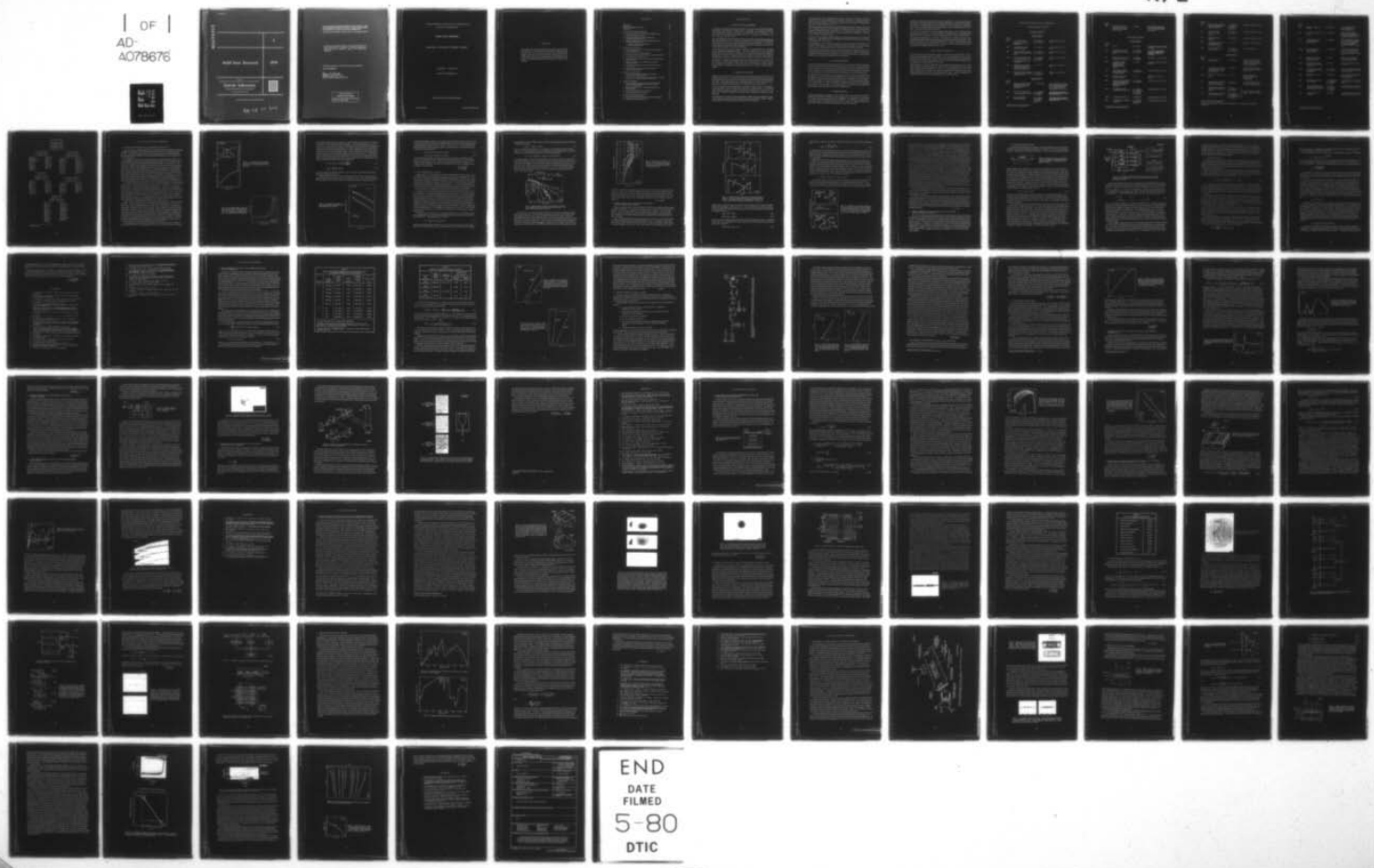
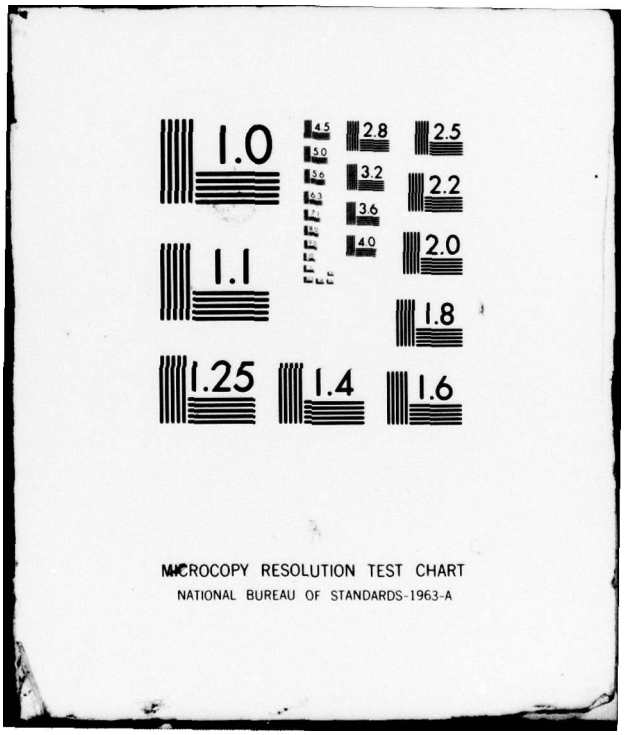
AD-A078 676 MASACHUSETTS INST OF TECH LEXINGTON LINCOLN LAB F/G 20/12
SOLID STATE RESEARCH.(U)
MAY 79 A L MCWHORTER
UNCLASSIFIED TR-1979-2 ESD-TR-79-150 F19628-78-C-0002 N/L



END
DATE FILMED
5-80
DTIC


1.0
1.1
1.25
1.4
1.6
1.8
2.0
2.2
2.5
2.8
3.2
3.6
4.0
4.5
5.0
5.6
6.3
MICROCOPY RESOLUTION TEST CHART
NATIONAL BUREAU OF STANDARDS-1963-A

ESD-TR-79-150

ADA078676

2

Solid State Research

1979

Prepared
under Electronic Systems Division Contract F19628-78-C-0002 by

Lincoln Laboratory

MASSACHUSETTS INSTITUTE OF TECHNOLOGY

LEXINGTON, MASSACHUSETTS



Approved for public release; distribution unlimited.

79 12 20 008

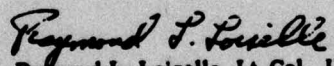
The work reported in this document was performed at Lincoln Laboratory, a center for research operated by Massachusetts Institute of Technology, with the support of the Department of the Air Force under Contract F19628-78-C-0002.

This report may be reproduced to satisfy needs of U.S. Government agencies.

The views and conclusions contained in this document are those of the contractor and should not be interpreted as necessarily representing the official policies, either expressed or implied, of the United States Government.

This technical report has been reviewed and is approved for publication.

FOR THE COMMANDER



Raymond L. Loiselle, Lt. Col., USAF
Chief, ESD Lincoln Laboratory Project Office

Non-Lincoln Recipients

PLEASE DO NOT RETURN

Permission is given to destroy this document when it is no longer needed.

MASSACHUSETTS INSTITUTE OF TECHNOLOGY

LINCOLN LABORATORY

SOLID STATE RESEARCH

QUARTERLY TECHNICAL SUMMARY REPORT

1 FEBRUARY – 30 APRIL 1979

ISSUED 25 SEPTEMBER 1979

Approved for public release; distribution unlimited.

LEXINGTON MASSACHUSETTS

ABSTRACT

This report covers in detail the solid state research work of the Solid State Division at Lincoln Laboratory for the period 1 February through 30 April 1979. The topics covered are Solid State Device Research, Quantum Electronics, Materials Research, Microelectronics, and Analog Device Technology. Funding is primarily provided by the Air Force, with additional support provided by the Army, ARPA, NSF, and DOE.

CONTENTS

	Abstract	iii
	Introduction	vii
	Reports on Solid State Research	x
	Organization	xiv
I.	SOLID STATE DEVICE RESEARCH	1
	A. Ionization Coefficients of Electrons and Holes in InP	1
	B. Electroabsorption in GaInAsP	4
	C. Subtraction of Signal Overlaps in Rutherford Backscattering Spectrometry	6
	D. Design Considerations for a High-Speed Electrooptic Analog-to-Digital Converter	9
	1. Converter Operational Principles	10
	2. Design Considerations	12
II.	QUANTUM ELECTRONICS	17
	A. Remote Sensing of CO and NO with Frequency-Doubled CO_2 Laser Radiation	17
	B. Thermal Behavior of NdP_5O_{14} Lasers	21
	C. Spectroscopic Measurements of $Tb_xY_{1-x}P_5O_{14}$ Compounds	24
	D. CW, High-Power Ni:MgO Laser	25
	E. Measurement of the Electronic Third-Order Susceptibility in Liquid $CO-O_2$	26
	F. Efficient Infrared AC Kerr Switches Using Simple Cryogenic Liquids	29
	G. Laser Photodeposition of Metal Films with Micrometer Size Features	29
	H. Imaging and RCS Measurements of Submillimeter Modeled Tactical Targets	31
III.	MATERIALS RESEARCH	37
	A. Calculated and Measured Efficiencies of Shallow-Homojunction GaAs Solar Cells	37
	B. Calculation of Crystallization Front Velocity for Amorphous Semiconductor Films Scanned with a CW Laser	41
IV.	MICROELECTRONICS	47
	A. Crystallographic Orientation of Silicon on Amorphous Substrate Using Artificial Surface-Relief Grating and Laser Crystallization	47
	B. Charge-Coupled Devices: SAW/CCD Programmable Matched Filter	51
	C. CCD Programmable Transversal Filter	55
	D. Charge-Coupled Devices: Imagers	61
V.	ANALOG DEVICE TECHNOLOGY	67
	A. Suppression of Spurious Signals in Memory Correlators	67
	B. MNOS Nonvolatile Analog Memory	70

INTRODUCTION

I. SOLID STATE DEVICE RESEARCH

The ionization coefficients of electrons and holes in InP have been determined from photomultiplication measurements on abrupt-junction, low-leakage, np^+ avalanche photodiodes. The ionization rate of holes β was found to be greater than that for electrons α. The ratio varies with the peak electric field E_m from $\beta/\alpha = 3.8$ at $E_m = 4.85 \times 10^5$ V-cm^{-1} to $\beta/\alpha = 2.7$ at $E_m = 6.37 \times 10^5$ V-cm^{-1}

The electroabsorption or Franz-Keldysh effect has been measured in $Ga_{0.24}In_{0.76}As_{0.52}P_{0.48}$ with an energy gap of 1.03 eV. Absorption coefficients were determined by measuring the transmission vs reverse bias through a double-heterostructure photodiode. The results are in good agreement with theory and are applicable to modulators and detectors in the 1.25- to 1.30-μm band of interest in optical-fiber transmission.

A subtraction technique has been developed to deduce the individual signals from overlapped ones in Rutherford backscattering spectra. The method eliminates one of the overlapping signals and yields the derivative of the other one, from which the two individual signals are reconstructed. When the technique was tested, good results were obtained using computer-simulated backscattering on a thin-film model which consisted of five layers of Au-Ag alloys.

An analysis of a high-speed electrooptic guided wave analog-to-digital (A/D) converter has been carried out. Design relationships are given for the electrooptic chip, the laser sampler, and the analog signal amplifier. Based on the analysis and available waveguide materials and technology, it is concluded that the development of a 6-bit 1-GS/sec converter should be feasible.

II. QUANTUM ELECTRONICS

Frequency coincidences have been determined between doubled CO_2-laser radiation and absorption lines of CO and NO, and the anticipated energy requirements have been calculated for remote sensing of these molecules by topographic reflection using a differential absorption system. The results indicate that concentrations typical for vehicle effluent should be measurable at reasonable ranges using the mini-TEA laser as the primary source.

In order to characterize the high-performance limitations of NdP_5O_{14} lasers, the dependence of the output power on duty cycle has been measured for a quasi-CW laser. No anomalous mode or spectral changes were observed under different heating or drive conditions; the CW output power limitation is explained by a thermally induced population increase in the lower laser level.

The spectroscopy of terbium-yttrium pentaphosphate crystals has been investigated to determine the potential of these materials as lasers for the blue-green spectral region. Radiative and nonradiative rates have been measured using KrF* laser excitation.

A CW Ni:MgO laser has been operated for the first time. Nearly 6 W of output at 1.32 μm was obtained at 77 K by optical pumping with a 1.06-μm Nd:YAG laser. Temperature tuning in wavelength regions between 1.316 and 1.409 μm was observed, with quasi-CW operation possible up to a crystal temperature of 235 K.

Experimental studies of the nonlinear susceptibility responsible for the tripling of CO_2 radiation in cryogenic liquids have been continued. Interference between the electronic and the two-photon resonant vibrational contributions to the third-order susceptibility tensor for liquid CO-O_2 mixtures has been used to measure the electronic contribution. A value of 3.9×10^{-34} Asm/V^3 has been obtained.

Efficient AC Kerr switching of visible radiation by infrared radiation has been demonstrated in liquid O_2. These switches are useful throughout the infrared spectral region with ultimate switching speeds of 0.1 to 0.3 psec.

The applicability of UV laser-induced dissociation to the processing of microelectronic components is being explored. Metal films with micrometer size features have been produced using a frequency-doubled argon ion laser to photodissociate metal alkyl compounds.

A submillimeter modeling system has been developed and applied to imaging and radar cross-section measurements of scaled tactical targets. The dependence of radar cross sections on transmitter/receiver polarization, resolution element size, and target aspect are being studied at frequencies of interest for a millimeter-wave radar system.

III. MATERIALS RESEARCH

By using a simple analytical model for GaAs solar cells with the $n^+/p/p^+$ shallow-homojunction structure, good fits have been obtained between computer calculations and experimental data for the external quantum efficiency and conversion efficiency of cells with different values of n^+-layer thickness. The calculations not only yield values for material properties of the GaAs layers composing the cells, but will also permit the optimization of cell design parameters.

In experiments on the crystallization of amorphous semiconductor films by scanning with the slit image of a CW laser, several unusual phenomena have been observed which include the formation of periodic structural features on the film surface, pulsations of the film temperature during scanning, and runaway crystallization of the entire film following first contact with the laser image. By means of preliminary computer calculations of the crystallization front velocity, it has been shown that these phenomena can be attributed to the liberation of heat accompanying the amorphous-to-crystalline transformation.

IV. MICROELECTRONICS

Uniform crystallographic orientation of 500-nm-thick silicon films has been achieved on amorphous fused silica substrates by laser crystallization of amorphous silicon deposited over surface-relief gratings etched into the substrates. The gratings had a square-wave cross section with a 3.8-μm spatial period and a 100-nm depth. The ⟨100⟩ directions in the silicon were parallel to the grating and perpendicular to the substrate plane.

A SAW/CCD programmable matched filter has been demonstrated. This device is capable of correlating an analog SAW signal of up to 40-MHz bandwidth and a 3.5-μsec duration against 300 samples of an analog reference previously loaded into a CCD shift register. This unique hybrid structure makes possible real-time processing of wideband inputs combined with low-speed, CCD-programmable reference patterns.

A 16-tap CCD transversal filter with tap weights programmable as 4-bit digital words has been fabricated and tested. The device has been successfully used as a programmable matched filter for a chirp signal. The matched-filter output has a dynamic range of 45 dB.

The spectral quantum efficiency of the 100- × 400-element CCD imager being built for the GEODSS (Ground Electro-Optical Deep Space Surveillance) Program has been measured. The imager is designed to have a maximum responsivity to an air mass 2 solar spectrum, which has a maximum photon flux at about 700 nm. The quantum efficiency averages approximately 50 percent over a midband range from 600 to 900 nm.

V. ANALOG DEVICE TECHNOLOGY

The major sources of spurious signals in memory correlators have been identified, and techniques for their suppression have been developed. The use of a split transducer drive in combination with metal shields under the ends of the silicon strips significantly reduces undesirable bulk-wave and edge-detection signals. It has been shown that all the development goals for suppression of spurious signals can be achieved.

MNOS capacitors are being investigated for use as analog nonvolatile memory devices. Linear signal storage over a dynamic range of at least 47 dB has been demonstrated. The loss of stored charge proceeds logarithmically in time at a rate proportional to the initial stored charge; a plot of flat-band voltage vs the log of the storage time is a straight line with a slope of approximately 0.1 V/decade per volt of initial flat-band voltage. Further investigations are centered on optimizing the conduction properties of the oxide and nitride.

REPORTS ON SOLID STATE RESEARCH

15 February through 15 May 1979

PUBLISHED REPORTS

Journal Articles

JA No.			
4829	ν_3 Mode Absorption Behavior of CO_2 Laser Excited SF_6	T.F. Deutsch S.R.J. Brueck	J. Chem. Phys. 70, 2063 (1979)
4843	Infrared Laser Photochemistry of Silane	T.F. Deutsch	J. Chem. Phys. 70, 1187 (1979)
4888	Collision Induced Predissociation in Photoassociated Hg_2	D.J. Ehrlich R.M. Osgood, Jr.	Chem. Phys. Lett. 61, 150 (1979)
4890	p-n Junction Diodes in InP and $In_{1-x}Ga_xAs_yP_{1-y}$ Fabricated by Beryllium-Ion Implantation	C.A. Armiento J.P. Donnelly S.H. Groves	Appl. Phys. Lett. 34, 229 (1979)
4899	Preparation of Sn-Doped In_2O_3 (ITO) Films at Low Deposition Temperatures by Ion-Beam Sputtering	J.C.C. Fan	Appl. Phys. Lett. 34, 515 (1979)
4907	Emission Cross Section and Flashlamp-Excited NdP_5O_{14} Laser at 1.32 μm	M.M. Choy* W.K. Zwicker* S.R. Chinn	Appl. Phys. Lett. 34, 387 (1979)

Meeting Speeches

MS No.			
4654	Advances in GaAs Schottky Diode Submillimeter Heterodyne Receivers and Radiometers	P.E. Tannenwald	Proc. AGARD Conf. No. 245, Millimetre and Submillimetre Wave Propagation and Circuits, Munich, Germany, 4-8 September 1978, p. 17-1
4760	Gap-Coupled InSb/$LiNbO_3$ Convolver Operating at 77 K	F.J. Leonberger R.W. Ralston S.A. Reible	1978 Ultrasonics Symposium Proceedings (IEEE, New York, 1978), pp. 238-242
4767	An Acoustoelectric SAW/CCD Device	D.L. Smythe R.W. Ralston B.E. Burke E. Stern	1978 Ultrasonics Symposium Proceedings (IEEE, New York, 1978), pp. 16-19

*Author not at Lincoln Laboratory.

MS No.			
4798	GaInAsP/InP Lasers and Detectors for Fiber Optics Communications at 1.1-1.3 μm	J.J. Hsieh	Proc. IEEE Intl. Electron Devices Mtg., Washington, D.C., 4-6 December 1978, pp. 628-629

* * * * *

UNPUBLISHED REPORTS

Journal Articles

JA No.			
4685	Lasers	H.J. Zeiger	Accepted by The Encyclopedia of Physics
4853	High Resolution Double Resonance Spectroscopy of SF_6	P.F. Moulton A. Mooradian	Accepted in Laser Induced Processes in Molecules (Springer-Verlag – to be published)
4871	MBE Techniques for IV-VI Optoelectronic Devices	H. Holloway* J.N. Walpole	Accepted by J. Cryst. Growth
4881	Zn-Diffused, Stripe-Geometry, Double-Heterostructure GaInAsP/InP Diode Lasers	J.J. Hsieh	Accepted by IEEE J. Quantum Electron.
4891	*Alkali-Metal Resonance*-Line Lasers Based on Photodissociation	*D.J. Ehrlich* R.M. Osgood, Jr.	Accepted by Appl. Phys. Lett.
4901	Synthesis and Crystal Growth of $CdGeP_2$	P. Vohl	Accepted by J. Electron. Mater.
4902	Anomalous Noise Behavior in Wide Bandwidth Photodiodes in Heterodyne and Background-Limited Operation	D.L. Spears R.H. Kingston	Accepted by Appl. Phys. Lett.
4920	Ion-Implanted, Laser-Annealed GaAs Solar Cells	J.C.C. Fan R.L. Chapman J.P. Donnelly G.W. Turner C.O. Bozler	Accepted by Appl. Phys. Lett.
4929	Tunable Infrared Lasers	A. Mooradian	Accepted by Rep. Prog. Phys.
4931	A SAW/CCD Accumulating Correlator	D.L. Smythe R.W. Ralston E. Stern	Accepted by Appl. Phys. Lett.

*Author not at Lincoln Laboratory.

JA No.			
4933	Planar Guarded Avalanche Diodes in InP Fabricated by Ion Implantation	J.P. Donnelly C.A. Armiento V. Diadiuk S.H. Groves	Accepted by Appl. Phys. Lett.
4936	FM Mode-Locked $Nd_{0.5}La_{0.5}P_5O_{14}$ Laser	S.R. Chinn W.K. Zwicker*	Accepted by Appl. Phys. Lett.
4937	Electroabsorption in GaInAsP	R.H. Kingston	Accepted by Appl. Phys. Lett.
4945	Schottky Diode Receivers for Operation in the 100-1000 GHz Range	B.J. Clifton	Accepted by Radio Electron. Eng.
4949	UV Solid-State Ce:YLF Laser at 325 nm	D.J. Ehrlich P.F. Moulton R.M. Osgood, Jr.	Accepted by Opt. Lett.

Meeting Speeches†

MS No.			
4542C, D	Recent Advances in Laser Devices	A. Mooradian	Seminars: University of Toronto, Ontario, Canada, 3 April 1979; University of Rochester, Rochester, New York, 27 April 1979
4846	A Comparison of Coplanar Waveguide and Microstrip for GaAs Monolithic Integrated Circuits	A. Gopinath	Intl. Microwave Symposium, Orlando, Florida, 30 April – 2 May 1979
4883B	Solar Cells: Plugging into the Sun	J.C.C. Fan	Physics Colloquium, Boston College, Boston, Massachusetts, 14 March 1979
4894	High-Efficiency GaAs Solar Cells on Single-Crystal GaAs and Ge Substrates	J.C.C. Fan C.O. Bozler	1979 Photovoltaic Solar Energy Conf., Berlin, West Germany, 23-26 April 1979
4898	Interband Magneto-Optical Studies in $In_{1-x}Ga_xAs_yP_{1-y}$ Alloys	K. Alavi* R.L. Aggarwal* S.H. Groves	American Physical Society Mtg., Chicago, 19-23 March 1979
5000	Magnetic Phase Dependence of Ni Reaction with CO	R.S. Mehta* G. Dresselhaus* M.S. Dresselhaus* H.J. Zeiger	

* Author not at Lincoln Laboratory.

† Titles of Meeting Speeches are listed for information only. No copies are available for distribution.

MS No.			
4928	Monolithic Integration in GaAs	R.A. Murphy	Intl. Solid State Circuits Conf., Philadelphia, 14-16 February 1979
4934	Acoustoelectric SAW/CCD Devices	D.L. Smythe	Greater Boston Chapter, IEEE Group on Sonics and Ultrasonics, Bedford, Massachusetts, 21 March 1979
4945	Ion Implantation in Si and III-V Compound Semiconductors	J.P. Donnelly	Joint IEEE Chapter on Microwave Theory and Techniques, Electron Devices, and Antennas and Propagation, St. Louis, Missouri, 17 April 1979
4945A, B	Ion Implantation in Si and III-V Compound Semiconductors	J.P. Donnelly	IEEE Chapters on Electron Devices: Schenectady, New York, 21 March 1979; and University of Illinois, 26 April 1979
4946	Fabrication and Applications of Artificial Microstructures	H.I. Smith	Seminar, Naval Research Laboratory, Washington, D.C., 22 February 1979
4946A	Fabrication and Applications of Submicrometer Structures	H.I. Smith	Seminar, Harvard University, 20 April 1979
4953	The Alignment of Masks and Substrates for X-ray Lithography	D.C. Shaver D.C. Flanders	X-ray Lithography Workshop, Stanford University, California, 21 February 1979
4954	Photodiodes at 1.06 to 1.6 μm	I. Melngailis	Optical Fiber Communications Mtg., Washington, D.C., 6-8 March 1979
5004	High-Speed Electrooptic A/D Converter	F.J. Leonberger C.E. Woodward D.L. Spears	SPIE Technical Symp. East '79, Washington, D.C., 17-18 April 1979
5009	Spectroscopic Studies of Small Molecule Interactions with Zinc Oxide Surfaces	R.R. Gay* E.I. Solomon* V.E. Henrich H.J. Zeiger	American Chemical Society, Honolulu, Hawaii, 4 April 1979
5022	Integrated Optics: A Tutorial	S.R. Chinn	Seminar, University of Lowell, Massachusetts, 25 April 1979

* Author not at Lincoln Laboratory.

ORGANIZATION

SOLID STATE DIVISION

A. L. McWhorter, *Head*
I. Melngailis, *Associate Head*
J. F. Goodwin, *Assistant*

P. E. Tannenwald, *Senior Staff*

QUANTUM ELECTRONICS

A. Mooradian, *Leader*
P. L. Kelley, *Associate Leader*

Barch, W. E.
Belanger, L. J.
Blumberg, W. A. M.
Brueck, S. R. J.
Burke, J. W.
Chinn, S. R.
DeFeo, W. E.
Deutsch, T. F.
Ehrlich, D. J.
Feldman, B.
Fetterman, H. R.
Fleming, M. W.*
Hancock, R. C.
Kildal, H.
Killinger, D.
Menyuk, N.
Moulton, P. F.
Osgood, R. M.
Parker, C. D.
Peck, D. D.
Pine, A. S.

APPLIED PHYSICS

A. G. Foyt, *Leader*
C. E. Hurwitz, *Associate Leader*
T. C. Harman, *Senior Staff*
R. H. Kingston, *Senior Staff*

Armiento, C. A.*
Calawa, A. R.
Carter, F. B.
DeMeo, N. L.
Diadiuk, V.
Donnelly, J. P.
Duffy, P. E.
Ferrante, G. A.
Glasser, L. A.*
Groves, S. H.
Leonberger, F. J.
Liau, Z-L.
Lind, T. A.
Maby, E. W.*
McBride, W. F.
Norris, P. E.*
Paladino, A. E.
Plonko, M. C.
Spears, D. L.
Tsang, D. Z.*
Walpole, J. N.

ELECTRONIC MATERIALS

A. J. Strauss, *Leader*
H. J. Zeiger, *Associate Leader*
J. G. Mavroides, *Senior Staff*

Anderson, C. H., Jr.
Bayard, M. L.
Button, M. J.
Chapman, R. L.
Davis, F. M.
Delaney, E. J.
Fahey, R. E.
Fan, J. C. C.
Finn, M. C.
Flutie, R. E.
Foley, G. H.
Gale, R. P.
Gay, R. R.*
Hong, H. Y-P.
Hsieh, J. J.
Iseler, G. W.
Kafalas, J. A.
Kolesar, D. E.
Krohn, L., Jr.
Mastromattei, E. L.
Owens, E. B.
Palm, B. J.
Pantano, J. V.
Salerno, J. P.*
Tracy, D. M.
Vohl, P.

ANALOG DEVICE TECHNOLOGY

E. Stern, *Leader*
R. C. Williamson, *Associate Leader*

Anderson, A. C.
Arsenault, D. R.
Baker, R. P.
Becker, R. A.
Brogan, W. T.
Cafarella, J. H.
DiPerna, M. S.
Dolat, V. S.
Holtham, J. H.
Hurlburt, D. H.
Kernan, W. C.
Oates, D. E.
Ralston, R. W.
Reible, S. A.
Slattery, R. L.
Withers, R. S.
Yao, I.

MICROELECTRONICS

W. T. Lindley, *Leader*
F. J. Bachner, *Associate Leader*
H. I. Smith, *Assistant Leader*

Alley, G. D.
Bozler, C. O.
Burke, B. E.
Chiang, A. M.
Chu, A.
Clifton, B. J.
Daniels, P. J.
DeGraff, P. D.
Durant, G. L.
Eastman, L. F.
Efremow, N.
Elta, M. E.
Felton, B. J.
Flanders, D. C.
Geis, M. W.
Gopinath, A.
Gray, R. V.
Hansell, G. L.*
Hawryluk, A. M.*
Lincoln, G. A., Jr.
Melngailis, J.
McGonagle, W. H.
Mountain, R. W.
Murphy, R. A.
Pichler, H. H.
Shaver, D. C.*
Silversmith, D. J.
Smythe, D. L.
Sotomayer-Diaz, O.*
Turner, G. W.
Wilde, R. E.

* Research assistant

I. SOLID STATE DEVICE RESEARCH

A. IONIZATION COEFFICIENTS OF ELECTRONS AND HOLES IN InP

Recent interest in avalanche photodiodes[1,2] and IMPATT devices[3] fabricated from InP has prompted an investigation of the ionization coefficients of electrons (α) and holes (β) in this material. The ionization rates are known to have a strong influence on both the noise[4] and gain-bandwidth product limitations[5] of avalanche photodiodes as well as on the noise and efficiency of IMPATTs.[6]

Unambiguous determination of the ionization rates from photomultiplication data on avalanche photodiodes requires two important experimental conditions.[7] One is that pure electron and pure hole injection into the high field region must be obtained in the same device. The second requirement is that the magnitude and variation of the junction electric field be known accurately. These two requirements are best met by use of an abrupt p-n junction photodiode, where incident radiation is completely absorbed in undepleted material on either side of the junction, allowing either electrons or holes to diffuse into the field region. This method has been employed successfully to determine ionization rates in other III-V materials.[8,9] Earlier measurements of the ionization rates in InP have been reported[10] for diffused junction devices where the photomultiplication data were interpreted under the invalid assumption that $\alpha = \beta$. Measurements also have been reported [11] on InP Schottky barrier diodes, a configuration for which the interpretation of the data is subject to several uncertainties,[12] with the result $\beta/\alpha \approx 5$.

The avalanche photodiodes used here were of the inverted mesa geometry fabricated by etching 138-μm-dia. mesas in a wafer consisting of a 5-μm-thick n-InP layer ($n = 1.7 \times 10^{16}$ cm^{-3}) grown by LPE on a (100)-oriented p^+-InP (Zn) substrate ($p \sim 2 \times 10^{18}$ cm^{-3}). Mesas were etched using a 1:1 mixture of 3% Br-methanol:H_3PO_4 at 45°C. Ohmic n- and p-type contacts were made by microalloying plated AuSn and evaporated AuMg, respectively. The center portion of the substrate was thinned to within 4 μm of the junction using a jet of a 1:1:6:1 mixture of HAc:$HClO_4$:HNO_3:HCl to facilitate photoinjection of electrons.[13] The final device structure is shown in the insert in Fig. I-1. The etched moat around the base of the mesa is an artifact of the etching procedure and has the positive attribute of insuring electrical isolation of the mesa while retaining some additional physical support in the rest of the wafer.

Dark currents of the diodes were of subnanoampere magnitudes up to voltages very close to breakdown. Figure I-1 illustrates the I-V characteristic of a typical diode. For some of the better devices, uniform photoresponse gains (within ±10 percent) of about 12 were measured with leakage currents as low as 0.35 nA. Typically, however, leakage currents at this value of gain tended to be about an order of magnitude larger. Reasonably uniform photoresponse gains of 150 with a concurrent leakage of 120 nA have been measured. Capacitance-voltage data indicated that these devices were abrupt junction diodes. Scanned photoresponse measurements from both sides of the wafer using the 6328-Å line of a HeNe laser were performed to ensure the absence of microplasmas and edge breakdown in the devices chosen for study. The diodes selected for photomultiplication measurements had uniform multiplication (±10 percent) over the area of the diode for the range of voltages used in the experiment.

Photomultiplication measurements were performed using a focused beam of strongly absorbed radiation (6328 Å), incident alternately on the n and p^+ sides of the diodes, resulting in

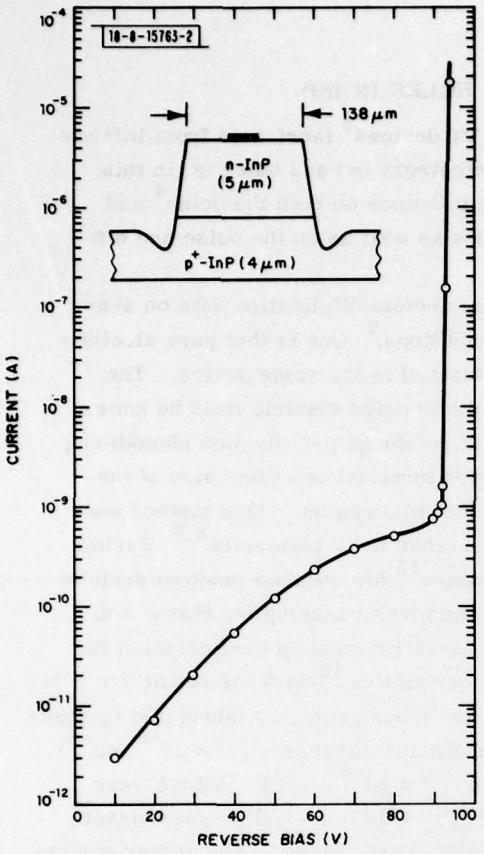


Fig. I-1. Current-voltage characteristics of a 138-μm-dia. np^+ InP avalanche photodiode. The inset shows the device structure.

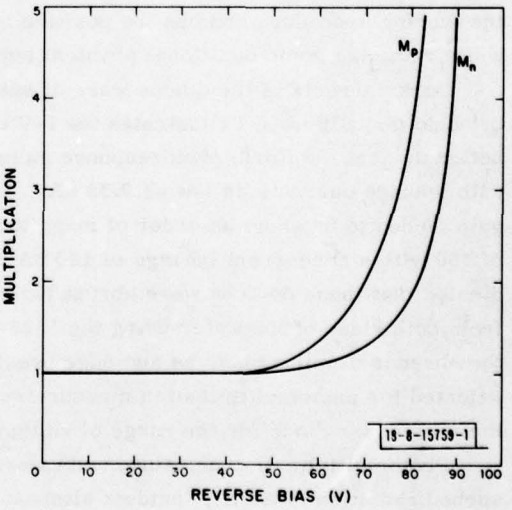


Fig. I-2. Electron-initiated (M_n) and hole-initiated (M_p) avalanche multiplication as a function of reverse bias in InP. The inset shows a schematic diagram of the experimental configuration.

pure hole and electron injection, respectively. The photoresponse as a function of reverse bias for each case was monitored with a lock-in amplifier. The injected photocurrent was of the order of 5 nA. Over a rather wide range of increasing reverse bias, below which multiplication was evident, the photocurrent rose slowly and very nearly linearly due to the increased collection efficiency of the widening depletion region. A linear extrapolation of this low field photoresponse was subtracted out at the higher fields to yield the values for the hole-initiated multiplication (M_p) and the electron-initiated multiplication (M_n) shown in Fig. I-2. The ionization rates were determined as a function of peak electric field (E_m) from the multiplication data by means of the following equations which apply for the case of a one-sided, abrupt-junction device with pure electron and pure hole injection, respectively.[14]

$$\alpha(E_m) = \beta(E_m) + E_m \frac{d}{dV}\left\{\ln\left[\frac{M_n}{M_p}\right]\right\} \tag{I-1}$$

$$\beta(E_m) = \frac{E_m}{M_n}\frac{d}{dV}\{\ln M_p\} \quad . \tag{I-2}$$

E_m was calculated using the applied voltage (V) and the carrier concentration obtained from capacitance-voltage measurements.

Application of Eqs. (I-1) and (I-2) to the multiplication data of Fig. I-2 yields the hole and electron ionization rates, plotted in Fig. I-3 as a function of $1/E_m$. These results show clearly that the ionization rate for holes is greater than that for electrons over the entire range of

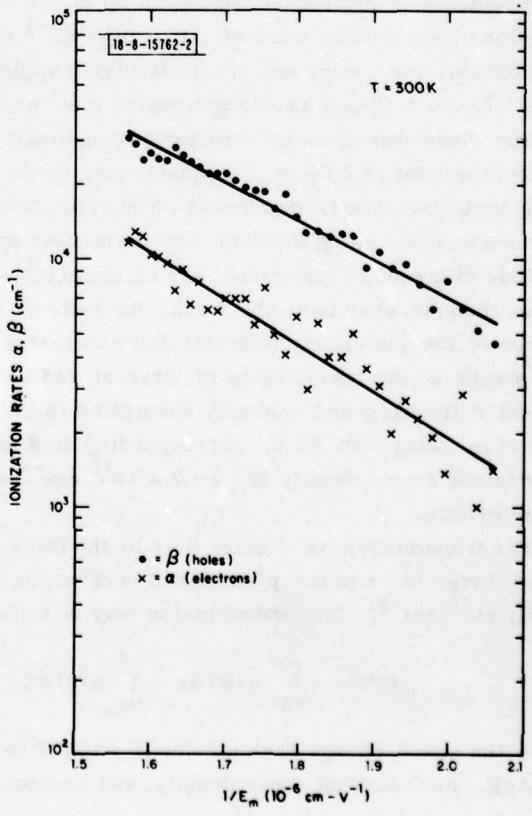


Fig. I-3. Ionization rates of electrons and holes in InP as a function of reciprocal peak electric field.

electric field strengths considered. For a peak electric field strength of 4.85×10^5 V-cm^{-1} the ratio of hole ionization rate to electron ionization rate (β/α) is 3.8. This ratio decreases with increasing electric field until $\beta/\alpha = 2.7$ at $E_m = 6.37 \times 10^5$ V-cm^{-1}. A least-squares fit of these data indicates that the ionization rates can be approximated over the range of electric fields used in this experiment as

$$\alpha(E) = 1.07 \times 10^7 \exp[-4.31 \times 10^6/E] \quad \text{(I-3)}$$

$$\beta(E) = 9.63 \times 10^6 \exp[-3.61 \times 10^6/E] \quad . \quad \text{(I-4)}$$

The measurements reported here provide some initial values for the ionization rates in (100)-InP, results which should be reliable because of the unambiguous nature of the experimental technique employed. Also, it has been demonstrated that uniform, high-gain, low-leakage avalanche photodiodes, suitable for use as detectors as well as for multiplication measurements, can be fabricated.

C. A. Armiento
S. H. Groves
C. E. Hurwitz

B. ELECTROABSORPTION IN GaInAsP

Measurements of electroabsorption (the Franz-Keldysh effect) have been made on the quaternary semiconductor alloy $Ga_{0.24}In_{0.76}As_{0.52}P_{0.48}$ which has an energy gap $E_G = 1.03$ eV. The data were obtained by measuring the transmission perpendicular to the plane of a reverse-biased double-heterojunction GaInAsP/InP photodiode. Since the thin quaternary layer enabled measurements of absorption coefficient up to values of 10^4 cm^{-1}, this represents a significant extension of the earlier work of Stillman et al.[15] on GaAs. The results are consistent with electroabsorption theory and are particularly applicable to detectors and modulators operating in the 1.25- to 1.30-μm wavelength region most suitable for optical-fiber transmission.

The diode was a mesa structure, previously described by Hurwitz and Hsieh,[16] with a p^+-InP substrate, a 2.5-μm p^+-n quaternary layer, and an n^+-InP top layer with small Au-Sn ohmic contacts. The transmission through the diode was measured as a function of wavelength and reverse bias, using a prism monochromator apertured to produce a focused spot equal to the diode diameter of 0.25 mm. The transmission of the p^+-InP substrate was measured by moving the spot away from the mesa; the ratio of these two measurements yielded the transmission of the quaternary material since the extra InP in the mesa structure is effectively transparent at the wavelengths of interest and the off-mesa measurement takes acount of the Fresnel reflections and residual absorption in the thicker substrate. Data were obtained up to reverse voltages of 40 V, corresponding to a maximum electric field of 3.6×10^5 V/cm for the constant donor density $N_D = 1.2 \times 10^{16}$ cm^{-3} determined from the capacitance-voltage characteristic.

The transmission is affected only by the field distribution in the n-type material since the space-charge layer in the p^+ material is of negligible thickness because of the high acceptor density 10^{18} cm^{-3}. The transmission may be written

$$\ln T = -\int_0^w \alpha(E)\, dx - \int_w^t \alpha(0)\, dx \quad \text{(I-5)}$$

where the space-charge region extends from 0 to w, and t is the thickness of the n-type GaInAsP. For constant donor density, and consequently a linear decrease of field with distance,

a small change in reverse voltage results in a change in space-charge width dw and the change in transmission becomes

$$d(\ln T) = -\alpha(E)\, dw + \alpha(0)\, dw \qquad \text{(I-6)}$$

where E is the peak field located at x = 0. Physically, the whole field distribution shifts to higher x; a thin layer dw at maximum field is added and an equal thickness layer at zero field is removed. The final expression in terms of the reverse bias becomes

$$\alpha(E) - \alpha(0) = (dT/dw)/T = (2qN_D V/\kappa\epsilon_o)^{1/2}\, (dT/dV)/T \quad . \qquad \text{(I-7)}$$

Using this expression, the measured transmission vs reverse bias, a dielectric constant[17] of 13.2, and the energy gap, 1.03 eV, the absorption coefficient vs field has been plotted in Fig. I-4. Also shown by the dashed line is the zero-bias absorption coefficient which was used to determine $\alpha(0)$. This zero-field value, determined from the net transmission through the whole quaternary layer, includes the effects of absorption in the p^+-layer. It therefore introduces some uncertainty in the absolute value of $\alpha(E)$ near the band edge, although the difference $[\alpha(E) - \alpha(0)]$ is still reliable.

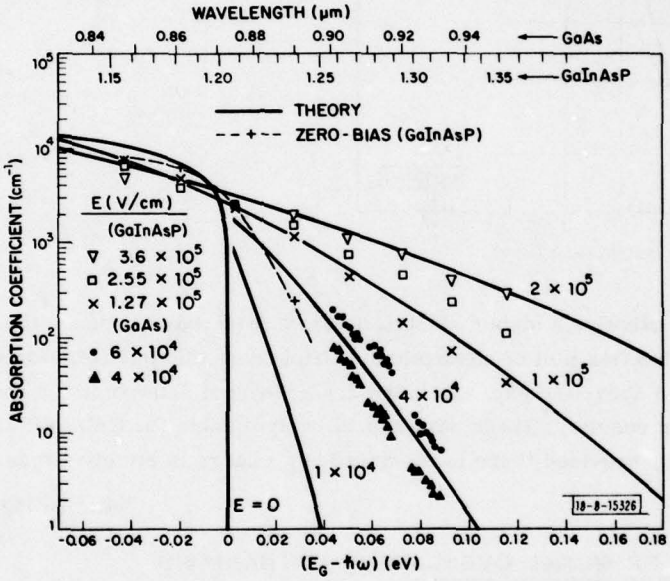


Fig. I-4. Experimental and theoretical absorption coefficient vs wavelength and electric field for GaInAsP and GaAs. The theory and GaAs data are from Ref. 15.

The data in Fig. I-4 include the results for GaAs (Ref. 15) as well as the theoretical predictions from the same work. The only materials parameters which enter into the theory of the electroabsorption effect[18] are the effective masses and the index of refraction. Since the masses[19] and index are the same within better than 10 percent for GaAs and GaInAsP, the theory should apply to the latter material also. The data in Fig. I-4 show good qualitative agreement with theory, including the predicted decrease at energies above the bandgap. There is also consistency with the earlier GaAs data in that the experimental values are significantly lower than

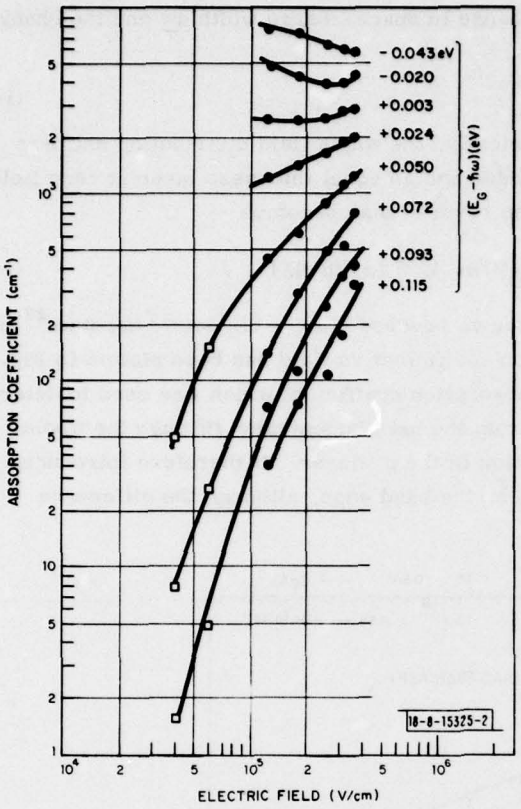


Fig. I-5. Absorption coefficient vs electric field for several values of $(E_G - \hbar\omega)$ for GaInAsP and GaAs. The data points at 4 and 6 × 10^4 V/cm are for GaAs, Ref. 15.

the theory, or alternatively, a higher electric field is required to produce the predicted absorption curve. Figure I-5 is a plot of absorption coefficient vs electric field for various energy differences below and above the gap. Included are additional data points on GaInAsP as well as points from the GaAs results. These data should be applicable for GaInAsP alloys over a wide range of energy gaps, provided there is no significant change in effective masses or index of refraction.

R. H. Kingston

C. SUBTRACTION OF SIGNAL OVERLAPS IN RUTHERFORD BACKSCATTERING SPECTROMETRY

Signal-overlapping has been a serious limitation in Rutherford backscattering (RBS) analysis of thin-film interactions. This problem was encountered in our recent RBS study of Au/InP contacts[20] in which the Au and In signals of the alloyed samples overlapped. To overcome this difficulty, we have developed a technique in which the individual signals can be obtained from the overlapped ones by a proper subtraction between two RBS spectra of slightly different incident ion energies.

Figure I-6 illustrates the main idea of this technique. In Fig. I-6(a), $f_1(E)$ and $g_1(E)$ represent the backscattered signals of two different elements F and G, respectively, in the target which has been analyzed with an incident ion energy E_1. Since $f_1(E)$ and $g_1(E)$ overlap, it is the sum of the two signals, $h_1(E) \equiv f_1(E) + g_1(E)$, that is obtained in the RBS experiment. When a

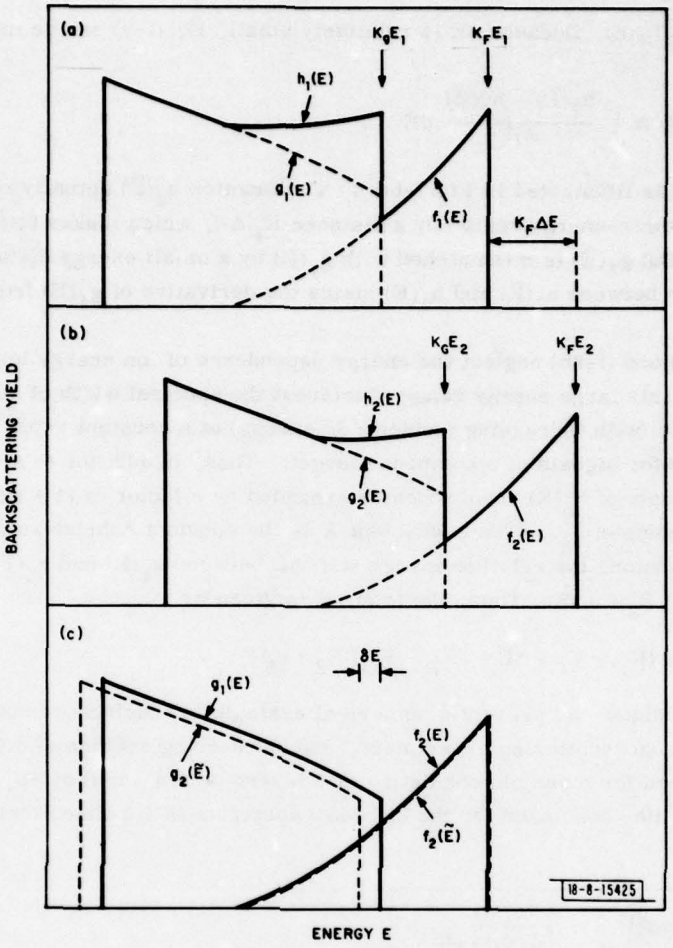


Fig. I-6. Illustration of the main idea in the present technique. Parts (a) and (b) represent RBS spectra of a sample taken at incident ion energies E_1 and E_2, respectively, with $E_2 > E_1$. Part (c) shows the matching of the two spectra in (a) and (b).

slightly higher incident ion energy E_2 is used for the same experiment, the signals will appear in higher-energy regions as shown in Fig. I-6(b). We first assume that the energy dependence of ion energy loss in the target material is so small that the individual signals are shifted without changes in shape, i.e.,

$$f_2(E) = f_1(E - K_F \Delta E) \tag{I-8a}$$

$$g_2(E) = g_1(E - K_G \Delta E) \tag{I-8b}$$

where K_F and K_G are the backscattering kinematic factors[21] of elements F and G, respectively, and $\Delta E \equiv E_2 - E_1$. By defining $\tilde{E} \equiv E + K_F \Delta E$, Eqs. (I-8a) and (I-8b) are then used to transform $h_2(E) \equiv f_2(E) + g_2(E)$ into

$$h_2(\tilde{E}) = f_1(E) + g_1(E + \delta E) \tag{I-9}$$

where $\delta E \equiv (K_F - K_G)\,\Delta E$. Because δE is relatively small, Eq. (I-9) can be further transformed into

$$g_1(E) \cong \int \frac{h_2(\tilde{E}) - h_1(E)}{\delta E}\, dE \quad . \tag{I-10}$$

The physical picture is illustrated in Fig. I-6(c). The function $h_2(\tilde{E})$ actually represents a translation of $h_2(E)$ to a lower-energy region by a distance $K_F \Delta E$, which makes $f_2(\tilde{E})$ coincide completely with $f_1(E)$. But $g_2(\tilde{E})$ is mismatched with $g_1(E)$ by a small energy distance δE. Therefore, the subtraction between $h_2(\tilde{E})$ and $h_1(E)$ yields the derivative of $g_1(E)$ from which $g_1(E)$ can be reconstructed.

Equations (I-8a) and (I-8b) neglect the energy dependence of ion energy loss in the target material. Over a fairly large energy range of interest the spectral width of an elemental thin-film target decreases (with increasing incident ion energy) at a constant rate.[21,22] We assume that this is also true for signals of a compound target. Thus, in addition to a shift by a distance $K_F \Delta E$, the energy scale of $h_2(E)$ should then be expanded by a factor of $(1 + s\Delta E)$ such that $f_2(\tilde{E})$ matches with $f_1(E)$ completely. (The coefficient s is the constant "shrink rate" of the signals.) Because of this expansion, the relative energy shift δE between $g_1(E)$ and $g_2(\tilde{E})$ will increase by an amount $(K_F - K_G)\, E_2 \cdot s\Delta E$. Thus, the total δE is given by

$$\delta E = (K_F - K_G)\,\Delta E + (K_F - K_G)\, E_2 \cdot s\Delta E \quad . \tag{I-11}$$

To test this technique, we present a numerical example in which a computer program[23] is used to simulate the backscattering experiment. Backscattering spectra of 2.0 and 2.1 MeV $^4He^+$ ions are obtained for a sample consisting of 5 layers (400 Å each) of Au_xAg_{1-x}, as shown in Fig. I-7(a). The $^4He^+$ dose used for the 2.1-MeV spectrum is 1.1 times that of the 2.0-MeV

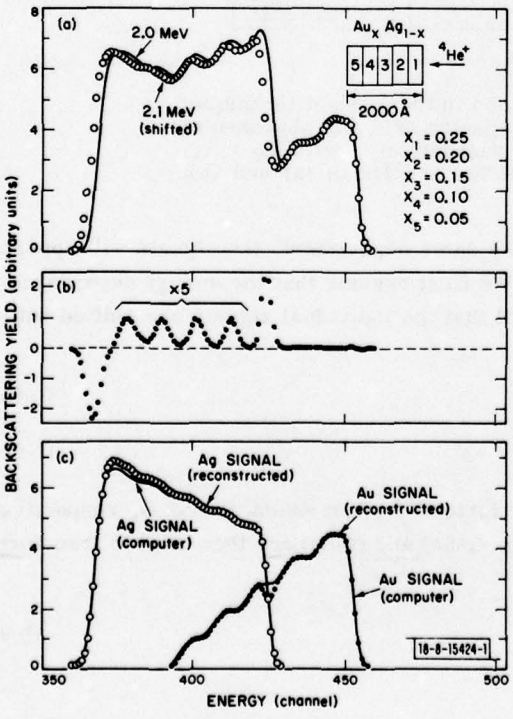


Fig. I-7. Example of the present technique. Part (a) shows computer-simulated RBS spectra of the Au_xAg_{1-x} sample. Part (b) shows the difference between the two matched spectra in (a). Part (c) shows the reconstructed as well as the original Ag and Au signals.

one (to compensate the energy dependence of the Rutherford cross section), such that the "clean" Au signals in the high-energy regions are of equal heights. The energy scale for the 2.1 MeV spectrum is 3.92 keV/channel as compared to 4.00 keV/channel for the 2.0-MeV one. This corresponds to an s-value of 2.0×10^{-4}/keV or $s\Delta E = 2.0 \times 10^{-2}$. The δE as obtained by using Eq. (I-11) is 8.28 keV. Figure I-7(b) shows the difference between the two matched spectra in Fig. I-7(a). Starting from the high-energy region, the integration of Eq. (I-11) is carried out by summing the readings in Fig. I-7(b), channel by channel. This integration yields the reconstructed Ag signal shown in Fig. I-7(c). The reconstructed Au signal is then obtained as the difference between the 2.0-MeV spectrum in Fig. I-7(a) and the reconstructed Ag signal in Fig. I-7(c).

The computer generates the individual Ag and Au signals as well as the overlapped ones in Fig. I-7(a). Comparisons in Fig. I-7(c) show that the present technique has closely reproduced the computer generated signals in large portions of the spectrum. Larger discrepancies are found in the reconstructed Au signal near the Ag edge. This is probably due to the rapid changes of the Ag signal near the Ag edge which cause larger errors in approximating $g_1(E + \delta E) - g_1(E)$ as $(dg_1/dE)\,\delta E$ in Eq. (I-10). There is also a gradual increase in discrepancy between the two Ag signals in the lower energy region in Fig. I-7(c). This can be caused by the slightly faster rising rate of the Ag signal of the 2.0-MeV spectrum than that of the 2.1-MeV one, due to the energy dependence of the Rutherford cross section. Although the difference is very small [causing ~0.5-percent difference in the two corresponding Ag signal heights near the low energy edges of the spectra in Fig. I-7(a)], the error can accumulate because of the integration procedure used in obtaining the reconstructed Ag signal. Calculations show that the error rises nearly parabolically, with a magnitude of a few percent near the low energy edge of the Ag signal, which is comparable to that observed in Fig. I-7(c).

One important approximation used in this technique is that the "shrink" of signals can be corrected by a single parameter s. Although this approximation appears to be a good one in the case of Fig. I-7, we do not know how good it is in other systems, especially those with extreme compositional nonuniformity.

In conclusion, we have demonstrated that individual signals can be obtained to high accuracies from the overlapped ones, by using a simple analytical technique which is mainly based on backscattering kinematics. The general validity of the approximation that the dependence of signal shapes on the incident ion energy can be compensated by a simple change of energy scale is yet to be evaluated. Should this question be answered affirmatively, the present technique can become very useful in RBS study of materials with moderate mass differences between the constituent elements.

Z. L. Liau

D. DESIGN CONSIDERATIONS FOR A HIGH-SPEED ELECTROOPTIC ANALOG-TO-DIGITAL CONVERTER

One of the most promising systems applications of integrated optical devices is the utilization of an array of waveguide electrooptic modulators to perform analog-to-digital (A/D) conversion.[24-26] Electrooptic A/D converters are of special interest because they should be capable of performing conversions at rates far exceeding what can presently be achieved with state-of-the-art technology. In addition, the electrooptic A/D converter permits optical sampling of the analog waveform and incorporates techniques that eliminate some of the inherent problems and complexities of integrated-circuit A/D converters. In this section, detailed design considerations are presented which suggest the feasibility of developing a 6-bit 1-GS/sec electrooptic A/D converter.

1. Converter Operational Principles

The fundamental integrated optical component of the electrooptic A/D converter is a planar waveguide version of a Mach-Zehnder interferometric modulator,[27-29] as shown schematically in Fig. I-8. It consists of an electrooptic crystal (e.g., $LiTaO_3$) containing a single-mode input

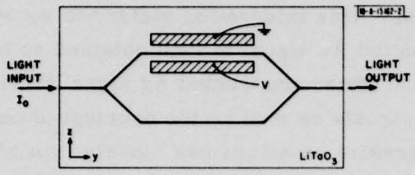


Fig. I-8. Schematic drawing of integrated optical Mach-Zehnder interferometer modulator fabricated from single-mode waveguides in $LiTaO_3$.

optical waveguide which branches at a Y to split the optical power into two equal components. Each component of light travels an equal distance before recombining at a second Y and exiting the crystal. In the absence of an applied voltage the light components recombine in phase, and a maximum output is obtained. If voltage is applied to one arm of the modulator via the coplanar electrodes shown in the figure the phase velocity of light propagating in that arm will be altered due to the linear electrooptic effect. This will produce a phase difference between light in the two modulator arms when they recombine, which will reduce the output signal. In the extreme case the two waves will be π radians out of phase. This will result in a null output since the two recombining light waves will try to form the second-order mode which the single-mode guide cannot support, and the light will radiate into the substrate. In general, it can be shown that for an input intensity I_o, the output intensity varies as

$$I = I_o [1 + \cos(\varphi + \Psi_s)]/2 \qquad (I-12)$$

where φ is the net phase difference between the two guides due to the applied voltage and Ψ_s accounts for any static phase difference between the arms. It should also be noted that the use of a three-electrode configuration, one between the two waveguides and two outside the guides, will reduce the required drive voltage by a factor of 2 for a given φ and minimize the modulator temperature dependence.

One can take advantage of the sinusoidal variation of the output intensity with voltage to form an A/D converter because the value of a bit in a binary representation of an analog signal varies periodically with the value of that signal. In particular, by combining a number of these modulators in parallel as shown in Fig. I-9(a), a converter can be fabricated which only requires one modulator per bit of resolution. The intensity output of the modulators vs the applied analog signal V_a is shown in Fig. I-9(b). The binary code is obtained by comparing the modulator outputs as detected by a photodiode at each output with a reference signal from the same light source used to excite the modulators. As shown in the figure, if the output intensity is above or below threshold I_t, a "0" or "1", respectively, is generated. The corresponding binary Gray code is also shown in the figures. In this converter, the sampling of the analog signal is done optically using a series of short laser pulses at the desired sampling rate. These pulses are applied in parallel to the modulators and also to the reference channel.

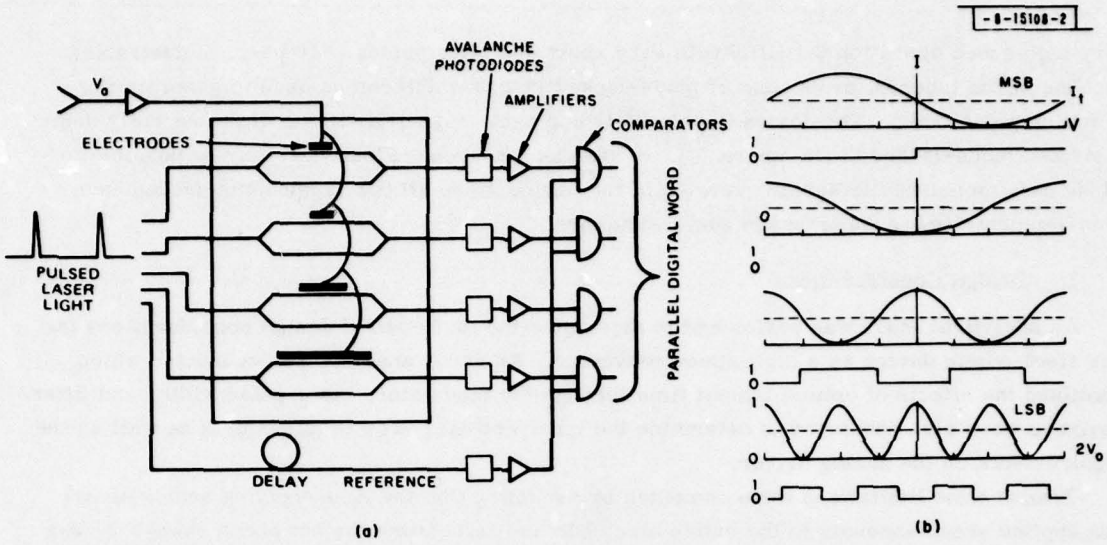


Fig. I-9. (a) Schematic diagram of a 4-bit electrooptic A/D converter. (b) Intensity vs voltage for a 4-bit A/D converter with Gray-code output (adapted from Ref. 25).

In the Gray-code approach shown here, the modulator electrode lengths differ by a factor of 2 between bit channels except for the two shortest modulators which have electrodes of equal length L_1. In general, the electrode length L_n for the n^{th} modulator of an N-bit converter is $L_n = 2^{n-2}L_1$, where n = 2, 3...N and n = 2 corresponds to the next-to-most significant bit and n = N corresponds to the least significant bit (LSB). The electrode length for the most significant bit (MSB) is L_1. The net phase change in this structure for the various channels is

$$\left.\begin{aligned} \varphi_1 &= kL_1V \quad , \qquad \Psi_1 = \pi/2 \\ \varphi_n &= 2^{n-2}kL_1V \quad , \qquad \Psi_n = 0 \qquad n = 2, 3...N \end{aligned}\right\} \tag{I-13}$$

where V is the applied voltage and k is a constant depending on the wavelength, the waveguide spacing and the crystal electrooptic parameters. For an N-bit device, a $\pi/2$ phase shift in the LSB channel corresponds to a change of one quantization step q in the applied voltage and results in a one-bit change of the output code. For an applied signal $V_a = V_o(1 + \sin\omega t)$ and 2^N quantization steps, $q = V_o/2^{N-1}$ and $kL_1 = \pi/V_o$. The static phase shift $\Psi_1 = \pi/2$ is obtained with a DC bias. The Gray code minimizes errors because, as shown, each quantization step only results in a change in one bit channel, unlike the conventional offset binary code in which multiple bits may change at each quantization step. In addition, the Gray-code output yields one more bit of precision than the offset binary code for a given set of electrode lengths and applied voltage.

The electrooptic technique has a number of advantages relative to other conversion methods. First, the device is relatively simple since only one modulator and detector are required per bit. An important characteristic is the decoupling of the analog signal from the optical sampling pulse. This should eliminate the distortion effects common to conventional devices that utilize diode-bridge sampling (or tracking) circuits. The electrooptic technique lends itself to

very high speed operation (>1 GHz) with very short sampling pulses (~10 psec, if desirable) because of the inherent properties of mode-locked lasers which can be used to generate the sampling pulse train. The device is relatively compact, especially if one of the recently demonstrated mode-locked diode lasers[30,31] is used as a source. Finally, it may be possible to fabricate a monolithic integrated version of the device since all the components needed have been demonstrated in GaAs-based semiconductors.

2. Design Considerations

An analytical study was performed to determine the fundamental design considerations for this electrooptic device as a high-speed converter. An error analysis was conducted which examined the effects of optical transit time through the modulator, laser pulse width, and jitter. Analyses were also conducted to determine the laser optical power requirements as well as the requirements on the analog driver.

Transit time limitations were computed by assuming that the time-varying analog signal was applied simultaneously to the entire electrode and calculating the net phase change $\bar{\varphi}$ of a wavefront of the laser pulse as it traveled the length of the electrode. For the n^{th} modulator, characterized by a transit time T_n, and an analog signal $V(t) = V_o(1 + \sin\omega t)$,

$$\bar{\varphi}_n \sim \pi 2^{n-2} \left[1 + \frac{\sin(\omega T_n/2)}{(\omega T_n/2)} \sin\omega(t + T_n/2)\right] \quad . \tag{I-14}$$

It can be seen from Eq. (I-14) that the net phase change exhibits a nonuniform attenuation and a delay dispersion between bits. Both these effects are caused by variation in electrode transit times between bit channels and lead to non-monotonicity effects. It should be noted that the simple averaging of the light pulse over the electrodes is a linear operation of integration. It can be completely described in terms of a linear filter and thus does not introduce errors in the conversion.

Non-monotonicity due to nonuniform attenuation occurs because the phase attenuation increases the required voltage to produce a given number of π phase shifts. It can be shown that the effect first occurs when the next-to-last "0"-"1" transition for the LSB (corresponding to near-maximum voltages) occurs at a larger voltage than the last "0"-"1" transition in the next-to-LSB [see Fig. I-9(b)]. This leads to the requirement that $T_N < 2^{2-N/2}/\pi f_s$, where f_s is the maximum signal frequency component to be digitized.

Delay dispersion is a potentially much more severe limitation. By a similar argument to that given above, non-monotonicity occurs for $T_N < 2^{1-N}/\pi f_s$. However, this effect is known and can be compensated for by introducing an appropriate delay between bit channels. A convenient way to do this is to align all the modulator electrodes along their centerline as illustrated in Fig. I-9(a).

Laser pulse width effects were calculated by assuming that the detector output was determined by the average intensity over the entire optical pulse width. Transit time effects were also incorporated in the analysis. Assuming $V_a = V_o(1 + \sin\omega t)$, a worst case of the high-frequency zero-crossing was examined. Both a square and a Gaussian pulse shape were analyzed.

For the ideal case of a square wave of width D, one obtains

$$\bar{I}_n \sim \frac{\sin(k_n\omega_s D)}{k_n\omega_s D} \cos[k_n(\omega_s T_n - 2)]$$

where $k_n \equiv kL_nV_o/2$. A nonlinear error occurs when the $\sin x/x$ terms change sign. If errors are to be limited to the LSB, then $D \leq (\pi f_s 2^{N-2})^{-1}$.

A similar analysis of the more realistic case of a Gaussian pulse of shape $\sim e^{-t^2/s^2}$ leads to

$$I_n \sim \cos[k_n(\omega_s T_n - 2)]\, e^{-k_n^2 \omega_s^2 s^2} \quad .$$

The limit on laser pulse width occurs when the amplitude is too small for detection. This can be approximated by requiring that the exponential term be above a detection limit η $\{$i.e., $\exp[-k_n^2\omega^2 s^2] \geq \eta\}$, and leads to a full width half maximum $s_{1/2}$ for the Gaussian pulse of

$$s_{1/2} \leq \frac{\sqrt{(\ln 2)\,(\ln 1/\eta)}}{\pi^2 f_s 2^{N-3}} \quad .$$

The limitation in the jitter of the onset of the sampling interval is set by consideration of the high-frequency zero-crossing of the analog signal. If the requirement taken is that the voltage uncertainty ΔV be less than quantization step size, then the allowable jitter time Δt is given by $\Delta t = (\pi f_s 2^N)^{-1}$.

The necessary laser optical power was estimated by defining an allowable probability of a 2-bit error. The worst case occurs if the LSB is very near a threshold crossing and the next-to-MSB (or the MSB) is also near a threshold crossing. Sufficient laser power should be used to ensure that to within the chosen error probability the more significant bit is detected correctly. This requires that $i_{sm}/i_n \geq x(2^{N-1}/\pi)$, where i_{sm} is the maximum signal photocurrent deviation from I_t, i_n is the rms noise current, and x is set by the desired error probability assuming Gaussian noise statistics. If it is assumed that the detectors are avalanche photodiodes of gain G and responsivity r and that the light coupling coefficient into the waveguides is k_i, one can write $i_{sm} = P_i k_i r G$, where P_i is the required incident power. This leads to the requirement that

$$P_i \geq i_n x 2^{N-1}/\pi k_i r G \quad .$$

The analog driver requirements were computed by assuming the modulator impedance could be modeled as a capacitance and that contact resistance was negligible. The rms signal power P_a was estimated as $V_o^2/2R$, where R is the source impedance and $2V_o$ is the voltage required to generate 2^{N-1} π phase shifts in the LSB modulator. [Although the analog signal is of the form $V_a \sim V_o(1 + \sin\omega t)$, the DC term V_o can be introduced by a level shift and therefore does not affect the driver power requirement.] R was computed assuming that the RC product of the modulators and source would correspond to a 3-dB frequency twice f_s. That is, the driver-modulator would be no worse a filter than other components in the signal processing system. Using expressions for the capacitance and electric field profile of coplanar electrodes,[32] it is found that

$$P_a = \pi k_1 k_2^2 \ln(4W_2/W_1)\, f_s \lambda^2 W_1^2 2^{N-1}/L_1 \quad .$$

Here k_1 and k_2 are defined by the coplanar capacitance and the electrooptic coefficients, respectively, λ is the optical wavelength and W_1 and W_2 are the spacings between the inner and outer edges of the coplanar electrodes along the waveguide. To minimize the necessary power,

one clearly should minimize λ and W_1 and maximize L_1. Another requirement on the analog driver amplifier is that its linearity not deviate by a quantization step (i.e., linear to one part in 2^N).

Based on this analysis and a consideration of waveguide materials and technology, it is concluded that the development of a 6-bit 1-GS/sec converter should be feasible. This converter which will be reported on in the future would require an array of $LiTaO_3$ electrooptic modulators, a doubled mode-locked Nd:YAG laser, and ~1 W rms of analog signal power.

F. J. Leonberger
C. E. Woodward
D. L. Spears

REFERENCES

1. C. A. Armiento, J. P. Donnelly, and S. H. Groves, Appl. Phys. Lett. 34, 229 (1979)
2. J. P. Donnelly, C. A. Armiento, V. Diadiuk, and S. H. Groves, Applied Physics Letters (to be published).
3. J. J. Berenz, F. B. Frank, and T. L. Hierl, Electron. Lett. 14, 683 (1978).
4. R. J. McIntyre, IEEE Trans. Electron Devices ED-13, 164 (1966).
5. R. B. Emmons, J. Appl. Phys. 38, 3705 (1967).
6. G. Gibbons, Avalanche-Diode Microwave Oscillators (Clarendon Press, Oxford, 1973), pp. 66-72.
7. G. E. Stillman and C. M. Wolfe, in Semiconductors and Semimetals, edited by R. K. Willardson and A. C. Beer (Academic Press, New York, 1977), Vol. 12, p. 330.
8. T. P. Pearsall, R. E. Nahory, and M. A. Pollack, Appl. Phys. Lett. 27, 330 (1975).
9. _____, Appl. Phys. Lett. 28, 403 (1976).
10. I. P. Molodyan, S. I. Rodautsan, E. V. Russu, and S. V. Slobodchikov, Sov. Phys. Semicond. 8, 879 (1975).
11. C. W. Kao and C. R. Crowell, presented at the Workshop on Hot Electron Phenomena in Semiconductors, Cornell University, 17-19 August 1978 (unpublished).
12. G. E. Stillman and C. M. Wolfe, loc. cit., Vol. 12, p. 347.
13. The electron diffusion length in p^+-InP and the hole diffusion length in n-InP were estimated from electron-beam-induced current measurements on similar diodes to be approximately 1.4 and 2.8 μm, respectively.
14. M. H. Woods, W. C. Johnson, and M. A. Lampert, Solid-State Electron. 16, 381 (1973).
15. G. E. Stillman, C. M. Wolfe, C. O. Bozler, and J. A. Rossi, Appl. Phys. Lett. 28, 544 (1976).
16. C. E. Hurwitz and J. J. Hsieh, Appl. Phys. Lett. 32, 487 (1978).
17. S. H. Groves, private communication.
18. G. E. Stillman and C. M. Wolfe, loc. cit., Vol. 12, p. 381.
19. K. Alavi, R. L. Aggarwal, and S. H. Groves, Journal of Magnetism and Magnetic Materials (to be published).
20. Z. L. Liau, E. B. Owens, and J. L. Ryan (unpublished).

21. W. K. Chu, J. W. Mayer, and M.-A. Nicolet, Backscattering Spectrometry (Academic Press, New York, 1978).

22. J. F. Ziegler and W. K. Chu, At. Nucl. Data Tables 13, 463 (1974).

23. J. F. Ziegler, R. F. Lever, and J. K. Hirvonen, in Ion Beam Surface Layer Analysis, O. Meyer, G. Linker, and F. Kappeler, Eds. (Plenum Press, New York, 1976), Vol. 1, p. 163.

24. H. F. Taylor, Proc. IEEE 63, 1524 (1974).

25. H. F. Taylor, M. J. Taylor, and P. W. Bauer, Technical Digest of the Topical Meeting on Integrated and Guided Wave Optics, Salt Lake City, January 1978, Paper Ta C-1.

26. H. F. Taylor, IEEE J. Quantum Electron. QE-15, 210 (1979).

27. W. E. Martin, Appl. Phys. Lett. 26, 562 (1975).

28. T. R. Ranganeth and S. Wang, IEEE J. Quantum Electron. QE-13, 290 (1977).

29. H. Sasaki, Electron. Lett. 13, 693 (1977).

30. P. T. Ho, L. A. Glasser, E. P. Ippen, and H. A. Haus, Appl. Phys. Lett. 33, 241 (1978).

31. L. A. Glasser, Electron. Lett. 14, 725 (1978).

32. I. P. Kaminow, L. W. Stulz, and E. H. Turner, Appl. Phys. Lett. 27, 555 (1975).

II. QUANTUM ELECTRONICS

A. REMOTE SENSING OF CO AND NO WITH FREQUENCY-DOUBLED CO_2 LASER RADIATION

A program to use frequency-doubled CO_2 laser radiation for remote sensing of CO and NO molecules will be undertaken in the new roof facility, with the high-repetition rate mini-TEA laser[1] providing the CO_2 radiation and $CdGeAs_2$ serving as the frequency-doubling crystal. Since the laser is line tunable, remote sensing is limited to those CO_2 laser lines whose doubled frequency coincides with an absorption line of the molecules. At sea level, we define coincidence as a frequency difference $\Delta\nu < 0.1\ cm^{-1}$. A determination has therefore been made of all such coincidences between 1 to 0 absorption bands of CO and NO and frequency-doubled $^{12}C^{16}O$ laser lines, and of the relative merits of each of these coincidences for remote sensing purposes. In addition, the laser pulse energy requirements for direct detection of topographically backscattered radiation at the preferred frequencies have been investigated.

A list of all coincidences falling within our definition is given in Table II-1. To determine which of these coincident lines are most suitable for use in a remote sensing system, consideration was given to the available pulse energy of the mini-TEA laser at each line, the absorption cross section of each of the CO and NO lines and the atmospheric transmittance at the corresponding frequencies. The NO absorption band falls within a spectral region of strong H_2O absorption and, as a result, the doubled P(24) line of the 10.6-μm band is the only frequency-doubled laser line which can be used for remote sensing of NO without excessive H_2O absorption. Either the P(24) or the R(18) lines of the 9.6-μm band can be used for monitoring CO. The frequency-doubled P(24) line is slightly preferable, and further considerations are limited to that line.

The energy requirement calculations assume topographic backscatter from a diffuse reflector located a distance R from the receiver, a direct detection system and the use of a differential absorption technique in which the reflected response at the molecular absorption (coincidence) frequency is compared with reflection at a neighboring nonabsorbing frequency. The P(26) CO_2 laser lines of the 10.6- and 9.6-μm bands are suitable as the neighboring nonabsorbing lines for NO and CO, respectively.

It can be shown that, to a good approximation, the difference in reflected signals δ from the on- and off-coincidence radiation due to the presence of an absorbing molecule is given by

$$\delta = \frac{K\rho A}{\pi R^2} P_o(\lambda_c)\, T(\lambda_c, R)\, \{1 - \exp[-2n\sigma_m(\lambda_c)\, L]\} \qquad \text{(II-1)}$$

where K is the receiver efficiency, ρ the reflectivity of the topographic reflector, $P_o(\lambda_c)$ the output power at the coincident wavelength λ_c, $\sigma_m(\lambda_c)$ is the absorption cross section at λ_c, and n is the pollutant density which extends over a distance L. $T(\lambda, R)$ is the two-way atmospheric transmittance over a range R at wavelength λ defined by

$$T(\lambda, R) = \exp[-2\beta_m(\lambda)\, R] \qquad \text{(II-2)}$$

where β_m is the volume extinction coefficient of the atmosphere at λ. The values of σ_m and β_m at the chosen radiation frequencies have been determined and are given in Table II-2 for the standard midlatitude winter and midlatitude summer atmospheres.[2]

PRECEDING PAGE BLANK-NOT FILMED

TABLE II-1

SPECTRAL COINCIDENCES BETWEEN NO AND CO ABSORPTION LINES AND FREQUENCY-DOUBLED CO_2 LASER RADIATION

Molecule	Absorption Line Identification	Absorption Line Frequency† (cm^{-1})	CO_2 Laser Line Identification	Doubled CO_2 Laser Frequency‡ (cm^{-1})	$\Delta\nu$ ($2\nu_{CO_2} - \nu_{mol}$) (cm^{-1})
NO	$R(73/2)_{3/2}$	1977.2721	$^{+}R(42)$	1977.29546	0.0234
	$R(71/2)_{3/2}$	1975.2971	$^{+}R(40)$	1975.24230	−0.0548
	$R(53/2)_{1/2}$	1954.3952	$^{+}R(22)$	1954.42922	0.0340
	$R(37/2)_{3/2}$	1935.4951	$^{+}R(8)$	1935.41584	−0.0793
	$R(19/2)_{1/2}$	1909.1281	$^{+}P(8)$	1909.09160	−0.0365
	$R(1/2)_{1/2}$	1881.0398	$^{+}P(24)$	1881.09766	0.0579
CO	R(6)	2169.19834	$^{\times}R(30)$	2169.27032	0.07198
	R(2)	2154.59598	$^{\times}R(18)$	2154.60498	0.00900
	Q(11)	2140.96109	$^{\times}R(8)$	2140.92456	−0.03653
	P(14)	2086.32231	$^{\times}P(24)$	2086.32650	0.00419

+ indicates (10°0) to (00°1) band; × indicates (10°0) to (02°0) band.

† NO frequencies from Laboratoire de Spectroscopie Moleculaire, Univ. de Paris VI, 1973 (unpublished). CO frequencies evaluated from Dunham coefficients given by H. Kildal, R.S. Eng, and A.H.M. Ross, J. Mol. Spectrosc. 53, 479 (1974).

‡ CO_2 laser frequencies from Handbook of Lasers, R.J. Pressley, Ed. (Chemical Rubber Company, Cleveland, Ohio, 1971).

TABLE II-2
FREQUENCY-DOUBLED LINES FOR REMOTE SENSING

CO_2 Laser Line Identification	Doubled Radiated Frequency (cm^{-1})	Absorption Cross Section σ_m (cm^2)	Volume Extinction Coefficient β_m (km^{-1})	
			Midlatitude Winter	Midlatitude Summer
P(24) (10°0) – (02°0)	2086.3265	9.08×10^{-19}	0.1654	0.292
P(26) (10°0) – (02°0)	2082.5582		0.0334	0.1077
P(24) (10°0) – (00°1)	1881.0977	4.85×10^{-20}	0.335	1.445
P(26) (10°0) – (00°1)	1877.3780		0.411	1.694

The minimum detectable value of δ is defined to occur for a signal-to-noise ratio S/N = 1; i.e., for $\delta = P_N = (NEP)\,(2\Delta f)^{1/2}$, where the noise is taken as dark-current limited in the infrared. The minimum energy per pulse is then

$$E_o^{min}(\lambda_c) = P_o^{min}(\lambda_c)\,\tau = \frac{2\pi R^2}{K\rho A}\,\frac{(NEP)\,\sqrt{\tau}}{T(\lambda_c)\,\{1 - \exp[-2n\sigma_m(\lambda_c)\,L]\}} \qquad \text{(II-3)}$$

where we have taken the time-bandwidth product $\tau\Delta f = 2$. When averaged over a train of N pulses, the minimum energy requirement is reduced by the factor $(N)^{-1/2}$. To evaluate Eq. (II-3), the values NEP = 3×10^{-12} W $Hz^{-1/2}$, $\rho = 0.5$ and K = 0.1 are assumed.[3] Our effective telescope area A ≃ 600 cm^2 and $\tau \simeq 10^{-7}$ sec. Then

$$E_o(\lambda_c) \geq \frac{2 \times 10^{-6}\,R^2}{T(\lambda_c)\,\sqrt{N}\,\{1 - \exp[-2n\sigma_m(\lambda_c)\,L]\}} \quad . \qquad \text{(II-4)}$$

The minimum energy required per pulse is evaluated as a function of range in Fig. II-1 for a CO concentration of 100 ppm over a distance L = 50 m for midlatitude winter and summer atmospheres. The minimum energy vs range curves for a similar concentration of NO are given in Fig. II-2.

Using a mini-TEA CO_2 laser with a "three-mirror" grating-tuned cavity,[4] second-harmonic outputs of over 2 mJ/pulse have been obtained from the P(24) lines of both the 9.6- and 10.6-μm bands. A repetition rate of 500 Hz has been achieved with the mini-TEA laser; thus averaging pulses over a one-second interval can lead to an effective pulse energy in excess of 40 mJ. Longer averaging times would further increase the effective range or S/N ratio.

The above results indicate that remote sensing of CO and NO from topographic targets over ranges of a few kilometers should be feasible with our system. The range is most limited for NO under conditions of high atmospheric water vapor content due to the large H_2O absorption in the NO absorption band region. Although the standard midlatitude atmospheres encompass the

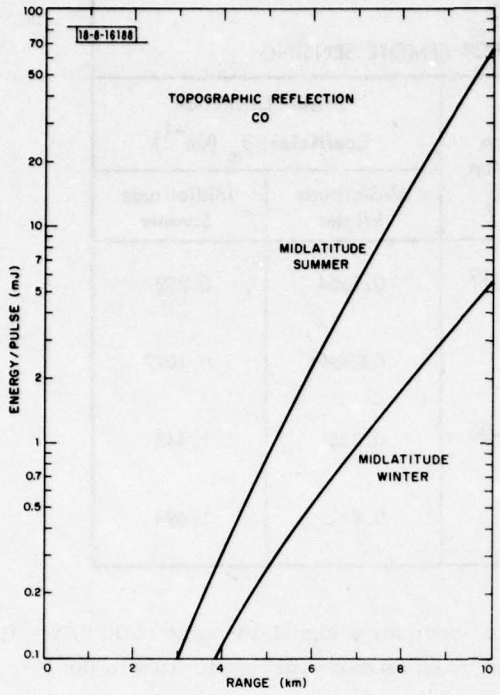


Fig. II-1. Minimum energy per pulse required for S/N = 1 as a function of range assuming a CO concentration of 100 ppm over a distance L = 50 m for standard midlatitude summer and winter atmospheres and topographic reflection.

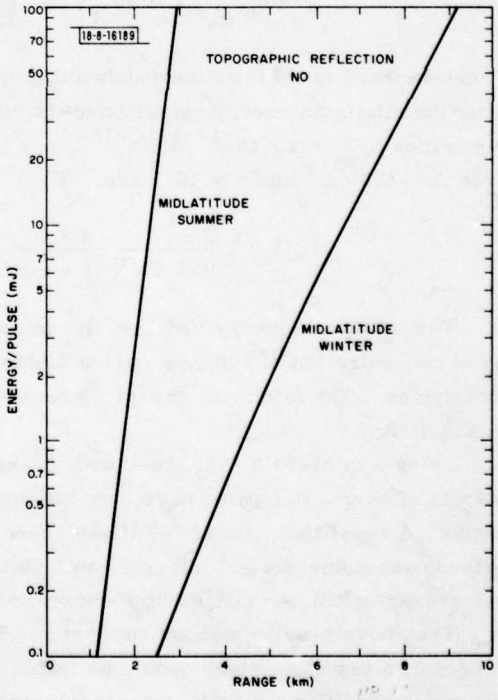


Fig. II-2. Minimum energy per pulse as a function of range assuming an NO concentration of 100 ppm over a distance L = 50 m for standard midlatitude summer and winter atmospheres and topographic reflection.

water vapor normally encountered, an accurate determination at the time of the experiment will be required. In addition, the level of ambient CO must be established for CO monitoring. The standard atmospheres assume a CO content of 0.075 ppm (Ref. 2). This is somewhat lower than the global average,[5] and is much lower than values which have been measured in urban environments.[6] The presence of additional amounts of ambient CO strongly increases the opacity of the atmosphere at the coincident frequency. For example, an increase in ambient CO content to 0.3 ppm will result in a tenfold decrease in atmospheric transmittance over a 2-km range, with a corresponding increase in the minimum energy required. Finally, the broad gain-bandwidth of our frequency-doubled atmospheric laser will alter the effective value of σ_m from the values shown in Table II-2, which are based on the line intensities given by McClatchey et al.[2] and the frequency difference $\Delta\nu$. To establish the proper value for our measurements, it will therefore be necessary to determine the effective values of σ_m for CO and NO using the frequency-doubled mini-TEA laser as the coherent radiation source.

N. Menyuk

B. THERMAL BEHAVIOR OF NdP_5O_{14} LASERS

During experimental investigations of high-Nd-concentration lasers, particularly NdP_5O_{14}(NPP), it has been observed that the output power often decreases at high excitation levels or duty cycles.[7,8] In order to develop useful CW NPP lasers it is necessary to understand the mechanisms which cause this effect.

A list of possible mechanisms for thermally caused degradation of the laser performance includes:

(1) increased population of the $^4I_{11/2}$ lower laser level, reducing the population inversion and gain;

(2) redistribution of population in the $^4F_{3/2}$ levels, reducing the gain on the dominant R_1-Y_1 laser transition;

(3) increase in laser transition linewidths;

(4) decrease in fluorescence lifetime;

(5) thermal lensing, through direct temperature dependence of the index of refraction or optical path length, or indirect strain and elasto-optic effects;

(6) optical deformation from ferroelastic domains.

The main conclusion we have reached is that for our NPP laser, direct lower laser level population in the Nd^{3+} $^4I_{11/2}$ level (item 1) is the dominant cause of efficiency decrease.

A schematic drawing of the laser apparatus is shown in Fig. II-3. The NPP laser had mirrors with 5-cm radii of curvature. One mirror had high reflectivity at 1052 nm and the other had reflectivity of either 99.6 or 99.0 percent. The laser rod in the center of the cavity was 2 mm square and 5 mm long along the lasing ('c') axis. The end faces were polished parallel to 20 arc-sec but were not antireflection (AR) coated. The effective mirror separation for mode calculations is $L_{eff} = L_M - \ell_c(n - 1/n)$, where L_M is the actual mirror separation, ℓ_c is the laser rod length (5 mm), and n is its index of refraction (1.60). In our cavity L_{eff} = 9.5 cm, which is sufficiently far removed from the concentric case (L_{eff} = 2 × mirror radius = 10 cm) that the cavity should be quite stable to perturbations.

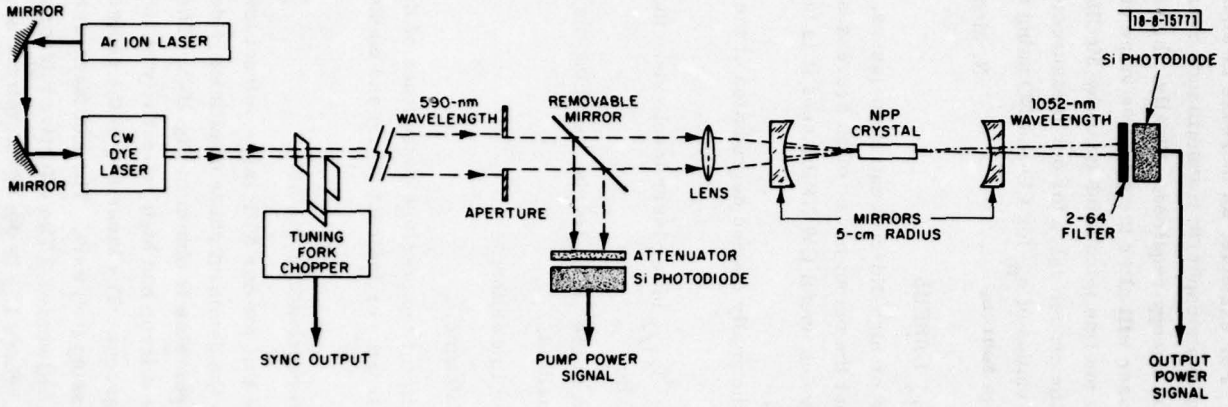


Fig. II-3. Schematic diagram of the collinearly excited NPP laser apparatus. Not indicated are auxiliary measuring devices including grating spectrometer, polarization analyzer, and infrared vidicon.

The NPP laser was pumped with collinear excitation from a CW rhodamine 6G dye laser tuned to 590 nm. This wavelength was chosen by tuning the dye laser until the pump beam was barely transmitted by the crystal, so as to obtain nearly complete absorption as uniformly as possible within the crystal. A 7.5-mm-dia. aperture was put in the beam before the pump focusing lens and Si photodiode used to measure the pump power. This diode was calibrated to measure the 590 nm power transmitted through the end mirror (high-reflectance at 1052 nm). The laser output power was measured with a calibrated Si photodiode preceded by a filter to eliminate the slight amount of transmitted pump radiation. A Glan prism could be inserted before the photodiode to measure the laser polarization. To examine the laser spectrum, the laser output beam was transmitted by a fiber optic bundle to a 1-m double-grating spectrometer, followed by a cooled InGaAs photomultiplier, boxcar amplifier, and chart recorder. The laser mode profile was obtained with an infrared-sensitive Si TV vidicon. Thus, in our series of experiments we measured the input power and duty cycle, and the output power, spectrum, polarization, and mode profile. In the data below, the measured powers refer to the quasi-CW powers during the excitation pulse, not the average powers.

Figure II-4 shows the experimental data for the output vs input power with the 99.6-percent-reflecting (0.4-percent-transmitting) mirror using duty cycles of η = 0.25, 0.50, and 1.0. With increasing duty cycle and heating, the threshold increases and the output and efficiency decrease. During the course of these measurements the laser mode profile was measured, and no change in shape or mode waist was observed. Data similar to Fig. II-4 were obtained with the 99.0-percent-reflecting mirror and are shown in Fig. II-5. The larger output transmission causes

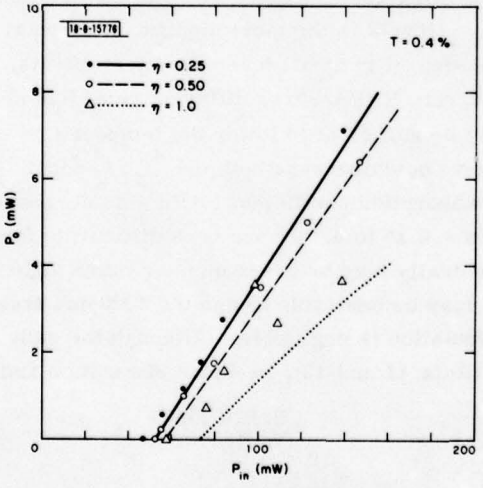


Fig. II-4. Output power as a function of input power for NPP laser with 0.4-percent-transmitting output mirror. The different data and curves refer to duty cycles of 0.25, 0.50, and 1.0.

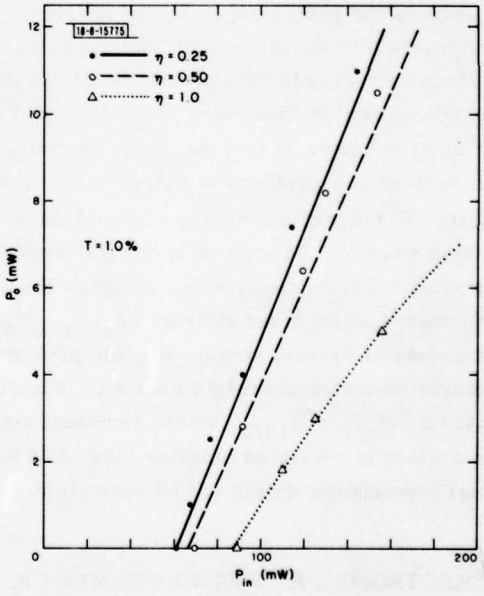


Fig. II-5. Output power as a function of input power for NPP laser with 1.0-percent-transmitting output mirror. The different data and curves refer to duty cycles of 0.25, 0.50, and 1.0.

somewhat higher thresholds, but also gives greater slope efficiencies. Heating effects are again evident. From these data, the internal loss is calculated to be 0.67 percent.

After performing these measurements, the laser rod was remounted for better cooling without changing the mirror separation. The 'a' side faces of the rod were held between two small thermoelectric cooler modules. A lowering of the surface cooling temperature of about 12°C restored the high-duty-cycle performance to CW operation.

On the basis of calculations and our experimental results, we have found that the terminal state thermal population is the most important effect of those listed above; to verify this conclusion further, we have calculated its contribution. The terminal state population has an exponential temperature dependence. Using measured values of the thermal conductivity in NPP, a simple model was used to calculate the temperature rise in the laser mode volume, leading to a nonlinear equation for the resonant-loss threshold term, proportional to the terminal state population. The results of this calculation are shown as the curves in Figs. II-4 and -5. A heat sink impedance parameter was adjusted in order to fit the data. In view of the approximations in the model, the experimental agreement is quite reasonable, and shows that this simple intrinsic heating effect can explain the observed power dependence of the laser output.

While these results pertain to one particular example, the general method and conclusions should have a considerably wider range of applications. For example, a useful geometry for practical NPP laser devices is the transverse pumping arrangement, using either CW sources such as light-emitting diodes (LEDs)[9] or pulsed sources such as flash lamps.[10] In such cases the pump absorption will be even more uniform than in the focused collinear pumping method, and our conclusions should be valid for the transverse pumping schemes as well. Generally, in such devices the geometric pumping efficiency will be lower than in the collinear case, and a larger fraction of the pump will heat portions of the laser rod outside the laser mode volume. This should affect only the calculation of the linear heating coefficients. The only restriction to our conclusions that increased population of the $^4I_{11/2}$ levels is the most significant thermal effect in NPP lasers is that the mode be stable with respect to small thermo-optical effects.

If heating is a problem in CW or high-repetition-rate NPP lasers, different remedies are possible. First, active cooling of the laser rod may be sufficient to lower the temperature in the lasing volume. Second, a lower Nd concentration would decrease both the $^4I_{11/2}$ population and the nonradiative decay rate, although the pump absorption coefficient would also decrease. Large, high-quality laser rods of $Nd_xLa_{1-x}P_5O_{14}$ ($x \simeq 0.25$ to 0.75) have been difficult to fabricate because of crystal strain, but this problem eventually may be overcome, or other high-Nd-concentration materials might be used. Finally, it may be desirable to use the 1320-nm transitions from $^4F_{3/2} \rightarrow {}^4I_{13/2}$, whose terminal state population is negligible. Although the gain cross section is ~5 times smaller than at 1050 nm (Refs. 11 and 12), resonant absorption and its thermal dependence should not be important.

S. R. Chinn
W. K. Zwicker†

C. SPECTROSCOPIC MEASUREMENTS OF $Tb_xY_{1-x}P_5O_{14}$ COMPOUNDS

A series of measurements has been initiated to determine the potential of terbium-yttrium pentaphosphate [(Tb, Y)PP] crystals as laser materials for the blue-green spectral region. Absorption and emission spectra have been taken and key radiative and nonradiative rates have

† Philips Laboratories, Briarcliff Manor, New York.

been measured with pulsed rare-gas:halide laser excitation. A strong absorption band in coincidence with the KrF pump laser has been found corresponding to the lowest 4f-5d transition. This may provide an excellent way in which to pump the candidate 4f transitions since 5d → 4f transfer is observed to be rapid.

In 100% TbPP the decay times of the prospective upper laser levels ($^5D_3$ and $^5D_4$) are 4.1 μsec and 3.1 msec, respectively, with the $^5D_3$ decay occurring predominantly into the $^5D_4$ state by nonradiative processes. The strongest 4f → 4f radiative transitions are $^5D_4 \rightarrow {}^7F_5$ and $^5D_3 \rightarrow {}^7F_5$. Growth techniques developed for NdPP crystals appear to be applicable to the growth of (Tb, Y)PP materials with, however, some alteration in growth parameters due to the difference between Tb, and Nd ionic radii. Based on the measured decay times and transition bandwidths, it is estimated that oscillators can be constructed from these materials with rare-gas:halide laser pumping if adequate crystals of high Tb doping can be obtained.

The (Tb, Y)PP materials are also good systems in which to study both 5d → 4f and 4f → 4f energy transfer. A particularly interesting example is the $^5D_3 \rightarrow {}^5D_4$ transfer, which presumably occurs as a result of long range interionic forces.

D. J. Ehrlich R. M. Osgood, Jr.
S. R. Chinn W. K. Zwicker†

D. CW, HIGH-POWER Ni:MgO LASER

The first CW operation of a Ni:MgO solid-state laser has been observed. Nearly 6 W of output at 1.32 μm was obtained by optical pumping of the $^3A_{2g} \rightarrow {}^3T_{2g}$ transition in a 1.85-cm-long crystal of Ni:MgO cooled in a liquid nitrogen Dewar. Up to 30 percent of the absorbed 1.06-μm pump radiation from a Nd:YAG laser was converted to Ni:MgO laser output. Quasi-CW operation was observed up to a temperature of 235 K. Preliminary temperature tuning results showed operation in several wavelength regions between 1.316 and 1.409 μm.

The laser crystal was grown by a carbon-arc fusion technique developed and carried out at Oak Ridge National Laboratory.[13] 5 wt% of NiO was added to the starting growth material; the resultant crystals contained about 0.5 wt% of Ni. The crystal used in the experiments was 1.85 cm long and had a cross section of 0.4 × 0.5 cm. The ends of the crystal were polished flat and AR coated for 1.4 μm.

Laser operation was observed with the crystal in the center of a 25-cm-long confocal cavity with 1.2-percent output coupling at 1.32 μm. The crystal was clamped to a heat sink attached to the cold finger of a liquid nitrogen Dewar. The heat sink temperature could be raised above 77 K by heating elements mounted in the heat sink and monitored by a Pt resistor. The two laser mirror surfaces were inside the vacuum chamber of the Dewar. The pump laser output was focused in the crystal by a 15-cm focal length lens. About 50 percent of the incident radiation was absorbed.

A curve of Ni:MgO laser output vs absorbed pump power input is shown in Fig. II-6. The heat sink temperature varied from around 82 K at the lowest pump power to 95 K at 22.6 W of absorbed power. At 95 K the temperature was fluctuating rapidly, presumably because of rapid boiling at the liquid-nitrogen cold-finger interface. Higher output powers should be obtainable with an improved cold-finger design. The pump laser was highly multimode (>10 times the diffraction limit) while the output of the Ni:MgO laser for the curve shown in Fig. II-6 was a mixture

† Philips Laboratories, Briarcliff Manor, New York.

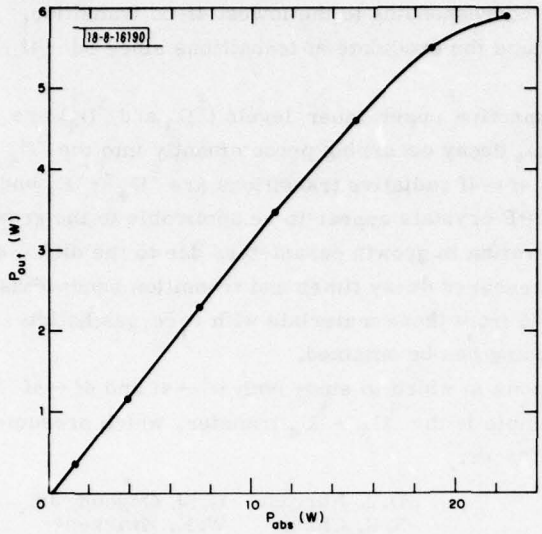


Fig. II-6. CW output power of Ni:MgO laser vs absorbed 1.06-μm pump power. Maximum conversion efficiency of pump into laser power ~30 percent. Roll-off in output power was due to limited cooling capacity of LN_2 Dewar.

of the TEM_{00} and TEM_{01} modes. Such behavior is possible because the cavity TEM_{00} mode size in the Ni:MgO crystal, 230 μm, is ~5 times larger than the expected size of a focused TEM_{00} mode from the pump laser. By reducing the number of modes operating in the pump laser it was possible to obtain single TEM_{00} mode output from the Ni:MgO laser, with 2.5 W of CW power.

Preliminary results of the effects of heat sink temperature on laser performance indicated that laser operation was possible up to 235 K at a 50-percent duty cycle with a 6-times-threshold increase over the threshold at 82 K. As the temperature increased from 82 K, the operating wavelength tuned from 1.316 to 1.328 μm at 131 K, shifted to 1.369 μm at 153 K and further shifted to 1.409 μm at 235 K.

More detailed measurements on the temperature behavior of the Ni:MgO laser will be performed. Since the lifetime of the laser transition remains constant[14] up to 300 K, it is possible that room temperature operation of the Ni:MgO laser can be obtained.

P. F. Moulton
A. Mooradian
Y. Chen†

E. MEASUREMENT OF THE ELECTRONIC THIRD-ORDER SUSCEPTIBILITY IN LIQUID $CO\text{-}O_2$

We have measured the electronic contribution $\chi_{el}^{(3)}$ to the nonresonant third-order susceptibility $\chi_{nr}^{(3)}$ of a liquid $CO\text{-}O_2$ mxture. This result is important for determining the optimum conditions for the two-photon resonant third-harmonic generation (THG) process[15,16] in liquid $CO\text{-}O_2$ and is also of fundamental interest.

In addition to $\chi_{el}^{(3)}$, there are also contributions to $\chi_{nr}^{(3)}$ due to electrostriction and molecular reorientation. These are larger than $\chi_{el}^{(3)}$ at low driving frequencies, but make negligible contributions to frequency mixing processes at optical frequencies because of their limited frequency response. A THG technique is therefore well suited for measuring $\chi_{el}^{(3)}$. Direct measurements

† Oak Ridge National Laboratory.

are difficult because of calibration problems; we have therefore chosen an interference technique. By tuning a CO_2 laser through the vibrational two-photon resonance in liquid CO-O_2, a variation in the THG signal is observed due to the interference between $\chi_{el}^{(3)}$ and the two-photon resonant susceptibility $\chi_{res}^{(3)}$. By measuring the frequency difference between maximum and minimum third-harmonic signal, $\chi_{el}^{(3)}$ can be determined relative to $\chi_{res}^{(3)}$.

The total $\chi^{(3)}$ for liquid CO-O_2 mixtures that contributes to THG is of the form[17-21]

$$\chi^{(3)}(\omega,\omega,\omega) = \frac{1}{2}\,\Delta\omega_n |\chi_{res}^{(3)}|_{pk} \left[\frac{1}{\omega_o - 2\omega + i\Delta\omega_n/2} + \frac{4\gamma^2/45}{\omega_o - 2\omega + i\Delta\omega_b/2}\right] + \chi_{el}^{(3)} \quad , \qquad \text{(II-5)}$$

in the limit of $\bar{\omega}\tau_\theta \gg 1$, where $\bar{\omega}$ is the width at 77 K of the O and S bands for gaseous CO vibrational two-photon absorption and τ_θ is the CO dielectric relaxation time in liquid CO-O_2. There are two contributions to the two-photon resonant susceptibility with very different linewidths $\Delta\omega_n$ and $\Delta\omega_b$. The narrow ($\Delta\omega_n$) and broad ($\Delta\omega_b$) resonance components are associated with, respectively, the isotropic or scalar part α and the anisotropic part β of the CO vibrational Raman polarizability tensor.[19,20] In Eq. (II-5) it is assumed that $4\gamma^2\,\Delta\omega_n/45\,\Delta\omega_b \ll 1$, where $\gamma = \beta/\alpha = 1.53$ for CO (Ref. 22). The linewidth and the vibrational frequency ω_o of the narrow resonance component, including the CO concentration dependence, have been measured by polarized spontaneous Raman scattering.[23] The broad linewidth, given by $\Delta\omega_b \approx 6/\tau_\theta \approx 60\ cm^{-1}$ can be estimated from infrared absorption data.[17,24] The center frequency of the broad resonance differs slightly from the position of the narrow component. The difference is negligible, however, compared to $\Delta\omega_b$.

Figure II-7 shows the frequency dependence of the observed third-harmonic signal for a CO-O_2 mixture at 77 K with a 0.077 relative CO peak absorbance. This relative peak absorbance is approximately proportional to the relative CO concentration.[17] The measurements were carried out using a tight-focusing geometry with a 0.65-cm confocal parameter in a 9.6-cm cell. The changes in the phasematching condition and the confocal parameter were negligible for the frequency range of 1035.46 to 1084.62 cm^{-1} over which the CO_2 laser was tuned stepwise. The third-harmonic signal in Fig. II-7 is therefore directly proportional to $|\chi^{(3)}(\omega,\omega,\omega)|^2$. The signal varies by more than six orders of magnitude. A destructive interference between the resonant and nonresonant terms in $\chi^{(3)}(\omega,\omega,\omega)$ is evident on the high-frequency side of the two-photon resonance at a frequency mismatch $\delta\omega = \omega_o - 2\omega$ of about $-6\ cm^{-1}$. Minimum signal is obtained

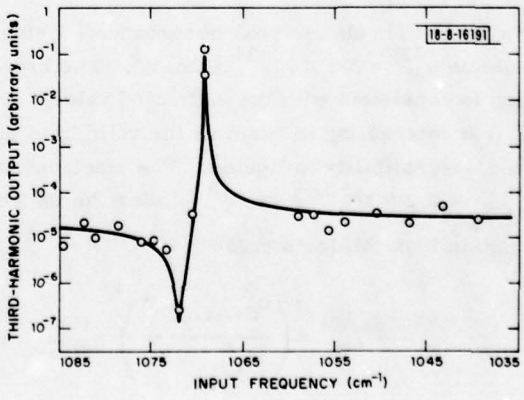


Fig. II-7. Interference between resonant and nonresonant contributions to $\chi^{(3)}(\omega,\omega,\omega)$ for a CO-O_2 mixture with 0.077 CO relative peak absorbance.

when the real part of $\chi^{(3)}(\omega, \omega, \omega)$ vanishes. This gives a relationship between the nonresonant and resonant parts of the third-order susceptibility tensor given by $\chi^{(3)}_{el} \approx -\Delta\omega_n/2\delta\omega\,|\chi^{(3)}_{res}|_{pk}$ when a small correction due to the broad resonance is neglected. The third-harmonic signal does not vanish at maximum destructive interference. The residual signal is determined mainly by the imaginary component of the broad resonance.

In order to determine accurately the signal level and frequency position for maximum destructive interference we have tuned through this region by changing the CO concentration while keeping the pump frequency constant at 1071.88 cm^{-1} [CO_2 R(10) line]. Figure II-8 shows the measured concentration dependence of the third-harmonic signal. A minimum is observed at a CO relative peak absorbance of 0.081. Without the interference, the third-harmonic signal would have exhibited a single peak characteristic of a tight-focusing geometry.

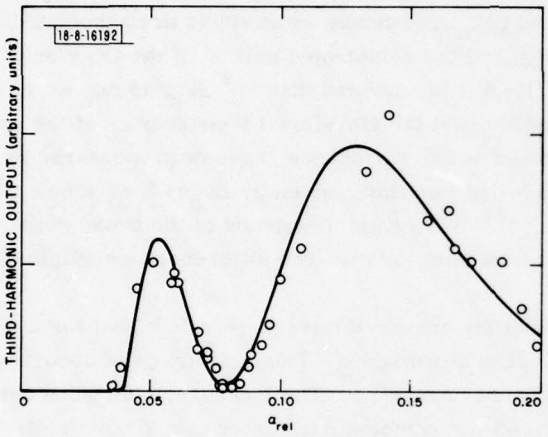


Fig. II-8. Third-harmonic signal near cancellation of resonant and nonresonant contributions to $\chi^{(3)}(\omega, \omega, \omega)$ in liquid CO-O_2 (laser emission at 1071.88 cm^{-1}, confocal parameter is 0.65 cm).

The solid curves in Fig. II-7 and -8 are the results of a computer calculation using $\chi^{(3)}_{el}$, $\Delta\omega_b$, and the signal amplitudes as the only adjustable parameters. In Fig. II-8 the dependence of $\chi^{(3)}_{el}$ and $\Delta\omega_b$ on the CO concentration was neglected, and the phasematching integral was calculated using the wave vector mismatch reported previously.[25] The value of $\chi^{(3)}_{el}$ is most sensitive to the curve fitting in Fig. II-8. We obtain

$$|\chi^{(3)}_{res}|_{pk}/\chi^{(3)}_{el} = 63 \pm 2$$

for a 0.077 CO relative peak absorbance. Using our previously reported value[15] for $|\chi^{(3)}_{res}|_{pk}$, we obtain $\chi^{(3)}_{el} = 3.9 \times 10^{-34}$ Asm/V^3. The broad resonance has a fitted linewidth of $\Delta\omega_b = 62$ cm^{-1} which is consistent with the estimated value.

It is interesting to examine the validity of applying Miller's rule[26] to the third-order electronic susceptibility in liquids. The electronic susceptibility for CS_2 has been reported[27] as $\chi^{(3)}_{el,CS_2} = 2.2 \times 10^{-32}$ Asm/V^3. Using the indices of refraction $n_{CS_2} = 1.62$ and $n_{CO\text{-}O_2} = 1.23$, we obtain from Miller's rule

$$\chi^{(3)}_{el} = \left(\frac{n^2_{CO\text{-}O_2} - 1}{n^2_{CS_2} - 1}\right)^4 \chi^{(3)}_{el,CS_2} = 2.2 \times 10^{-34}\ Asm/V^3$$

which is in reasonable agreement with the measured value. The indices of refraction are about the same for CO and O_2 liquids. Therefore, from this result, we expect little variation in measured $\chi^{(3)}$ with CO concentration.

H. Kildal
S. R. J. Brueck

F. EFFICIENT INFRARED AC KERR SWITCHES USING SIMPLE CRYOGENIC LIQUIDS

We have constructed efficient infrared AC Kerr switches of visible radiation using the cryogenic liquids O_2, N_2, and CO as the Kerr-active media. An intense CO_2 TEA laser pulse has been used to induce a birefringence greater than 1/2 wave for a visible probe beam in liquid O_2. Over 67 percent of the visible laser power was switched into the orthogonal linear polarization for a CO_2 input power of 1 MW. These infrared-visible Kerr switches offer significant promise for the generation of subpicosecond infrared pulses using an intense visible laser pulse to open the switch and, conversely, for upconverting the temporal dependence of short CO_2 pulses into the visible spectral region with subpicosecond resolution for diagnostic purposes.

These cryogenic liquids are transparent throughout the infrared with the exception of a few relatively narrow absorption bands corresponding to the vibrational fundamentals and overtones of the diatomic molecules. The dominant contribution to the Kerr coefficient arises from the partial orientation of the anisotropic molecules in the intense field; the speed of response of the medium is set by the orientational relaxation time τ_r which is in the 0.1- to 0.3-psec range for the cryogenic liquids.[24,28] This is substantially shorter than the relaxation time for the more conventional Kerr liquids CS_2 (τ_r = 1.8 psec) (Ref. 29) and nitrobenzene (τ_r = 32 psec) (Ref. 30) which have been used in the visible spectral region. Due to their infrared absorption, these more complex liquids are not generally useful throughout the infrared.

Efficient Kerr switches can be used to upconvert the temporal information on an infrared laser pulse to the visible spectral region. Conversely, these Kerr switches along with pulsed visible and near-infrared lasers may be used to gate infrared laser pulses. The required laser powers are in the 1- to 10-MW range. In order to realize the material limited switching speeds of 0.1 to 0.3 psec it will be necessary to compensate for the difference in the pulse group velocities between the infrared and optical spectral regions. This can be achieved by adding a molecule which exhibits the appropriate dispersion to the liquid, as has recently been demonstrated for phasematching of the third-harmonic generation process in liquid CO-O_2 mixtures.[15] The dispersion of all these liquids is sufficiently small that pulse spreading of the individual pulses is negligible for 0.1-psec duration pulses and 10-cm path lengths.

The details of the Kerr switches and the measurement of the AC Kerr coefficients of the cryogenic liquids will be reported elsewhere.

S. R. J. Brueck
H. Kildal

G. LASER PHOTODEPOSITION OF METAL FILMS WITH MICROMETER SIZE FEATURES

We have demonstrated the use of both pulsed and CW UV lasers to deposit metal structures with micrometer size features. Our experiments have explored one example of a general class of laser-initiated heterogeneous photochemical reactions which have application to removal of material (etching) as well as to the deposition of elements or compounds. The use of the laser permits ready spatial localization of the reaction region; hence, laser photodeposition may be applicable to the production of structures useful for microelectronics.

These techniques should be distinguished from laser processing based on strictly thermal effects such as laser annealing and chemical vapor deposition using laser heated surfaces. In our experiments molecular bonds are broken directly by UV laser photons, and free metal atoms are produced. These atoms then condense on a substrate.

We used the metal alkyl compounds trimethylaluminum (TMAl), $Al(CH_3)_3$, and dimethyl cadmium (DMCd), $Cd(CH_3)_2$, as parent gases from which Al or Cd were deposited. These gases have absorption bands with peaks near 200 nm and measurable absorptions for $\lambda < 260$ nm at pressures of the order of 1 Torr.

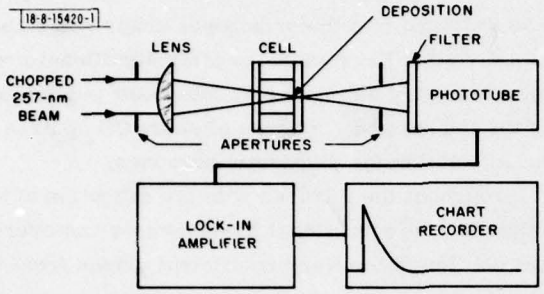


Fig. II-9. Schematic diagram of the experimental system used for deposition.

Figure II-9 shows the experimental setup used. The output of a CW argon ion laser operating at 514.5 nm is frequency doubled in an ADP crystal; the residual green light is removed by passing the beam from the crystal through a prism and the 257.2-nm radiation is focused on the quartz exit window of the 3.2-cm-long stainless steel cell by either a 7-cm focal length lens or a 0.5 N.A. reflecting microscope objective. The 257.2-nm light transmitted by the deposit is monitored by a photomultiplier and the resulting signal displayed on an X-Y recorder, allowing real-time monitoring of the growth of the deposit. Typical experimental conditions were $\sim 2 \times 10^{-4}$ W of 257.2-nm power, gas fills of 3 Torr DMCd or TMAl buffered with 750 Torr helium, and exposure times of 1 to 60 sec. The focus of the lens was located by translating the cell along the beam direction and noting the position at which the transmitted signal dropped most rapidly. Deposits were examined by dark-field and Nomarski microscopy, by scanning electron microscope (SEM), and by Auger electron spectroscopy.

Figure II-10 shows a Cd deposit obtained by irradiating a 3-Torr DMCd:700-Torr He mixture with 0.10 mW of 257.2-nm radiation for 60 sec with the substrate out of the focal plane of the 7-cm focal length lens; other deposits made with the substrate at the focal plane produced spots with lateral dimensions as small as 3 μm. This spot size corresponds to nearly diffraction limited performance by the single-element f/10 lens and does not indicate the potential resolution of the process. Figure II-10 shows that the Fresnel diffraction pattern in the plane of the window, imposed by slight aperturing of the Gaussian laser mode, is sharply reproduced in the metal deposit. Examination of the diffraction rings obtained in this set of depositions by SEM showed a series of well-modulated fringes with ring widths of 2 μm. The SEM examination revealed the presence of some secondary interference fringes with widths of 0.2 μm; while unintentional, these fringe patterns serve to illustrate that the ultimate resolution of the deposition process is in the submicrometer range. The SEM photos also showed that the typical height of such deposits was in the 1000- to 2000-Å range.

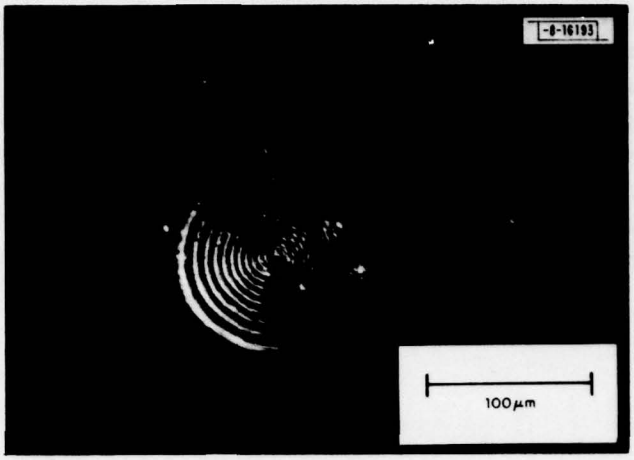


Fig. II-10. Cadmium deposit on SiO_2 substrate produced by 0.1-mW, 257.2-nm irradiation of 3-Torr DMCd:700-Torr He mixture for 60 sec.

In subsequent experiments 1.0-μm Cd lines were produced by translating the cell in a direction perpendicular to the beam axis by a motor-driven micrometer. In these experiments, the reflecting optics were used and the width of 1.0 ± 0.2 μm corresponds closely to the minimum spot size specified by the manufacturer of the lens, suggesting that smaller dimensions will be possible with diffraction limited optics. The thickness of the deposit is estimated to be ~100 Å from its optical transmission; greater thicknesses are possible with a slightly altered illumination geometry. Writing speeds were limited by the translator to ~25 μm/sec. A faster translator will allow the UV laser intensity to be increased to its maximum value (10^3 greater than at present) and hence greater writing rates will be possible.

D. J. Ehrlich
T. F. Deutsch
R. M. Osgood, Jr.

H. IMAGING AND RCS MEASUREMENTS OF SUBMILLIMETER MODELED TACTICAL TARGETS

A submillimeter system has been developed for and applied to imaging and radar cross section (RCS) measurements of scaled tactical targets. Current development of millimeter radar systems has created a requirement for RCS measurements of targets over a wide range of frequencies. A technique used for obtaining such data at a specified frequency of interest ν_o consists of measuring the power return from a scale model of the target at a modeling frequency ν_m given by

$$\nu_m = \nu_o \frac{D_o}{D_m}$$

where D_o is a linear dimension of the target and D_m is the corresponding linear dimension of the model.[31] The modeling technique allows a large amount of accurate data from complex targets, such as a tank, to be inexpensively and rapidly acquired. Details can be faithfully preserved and model size held to a manageable level at scale factors between roughly 20:1 and 100:1 (Ref. 32).

Assuming that the range of frequencies over which radar information is desired extends from approximately 10 to 240 GHz, it follows that the requisite frequency region for modeling includes the entire submillimeter (1 mm to 100 μm) and much of the far infrared (<100 μm). A particularly appealing feature of the modeling system described in this report is the use of optically pumped lasers which provide hundreds of available frequencies distributed throughout the submillimeter and far infrared.[33] As a result, a single experimental setup allows the modeling of virtually any microwave frequency of interest. Inexpensive but generally very accurate models are often available from commercial model manufacturers, with suitable scale factors for these measurements.

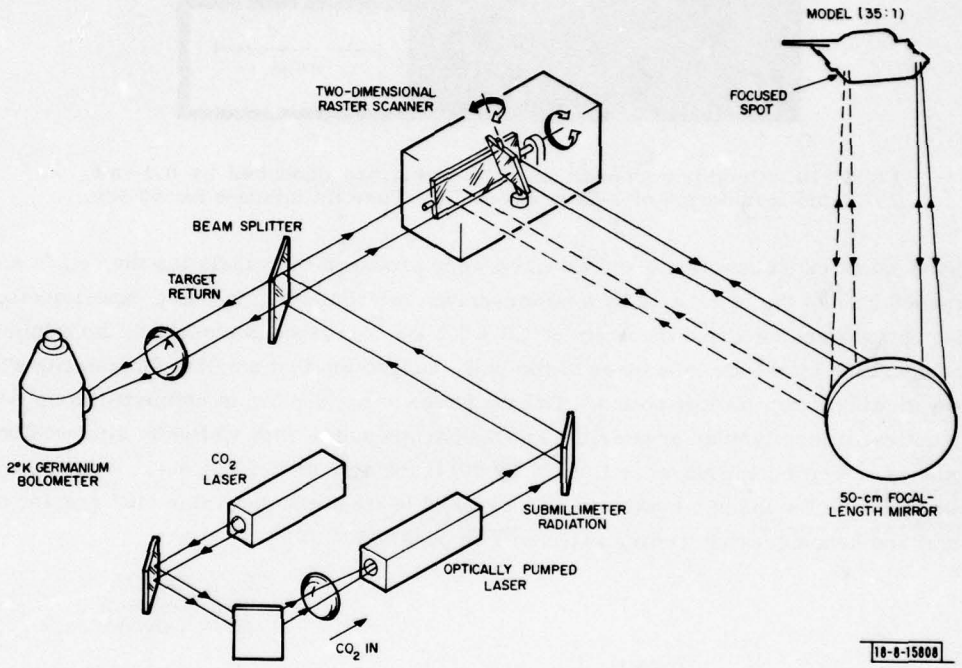


Fig. II-11. Schematic of the submillimeter model system showing the monostatic imaging configuration.

The initial experiments described herein involved imaging studies of a tank. Figure II-11 shows the experimental setup of the imaging system. Submillimeter radiation is directed by a beam splitter through a two-dimensional raster scanning system which scans the beam over a 25-cm-dia.f/2 spherical mirror. The near plane wave 2-cm-dia. Gaussian beam is focused to a waist and scanned over the target, which is positioned in the focal region of the mirror. Returns from the target are detected by a 2°K Ge bolometer positioned behind the beam splitter so as to obtain a monostatic view of the target. The resulting output is then displayed on a storage oscilloscope.

Three methanol laser lines at 1288, 2542, and 3125 GHz were selected to model 37, 70, and 90 GHz, respectively, thereby covering a substantial fraction of the millimeter region of interest. Figure II-12(a) shows oscilloscope traces of the image of the tank taken at a depression angle of 47° and an aspect angle of 0°. The outline of the tank model as viewed by the transmitter/receiver is shown in Fig. II-12(b). Considerable target structure is evident in the images, with

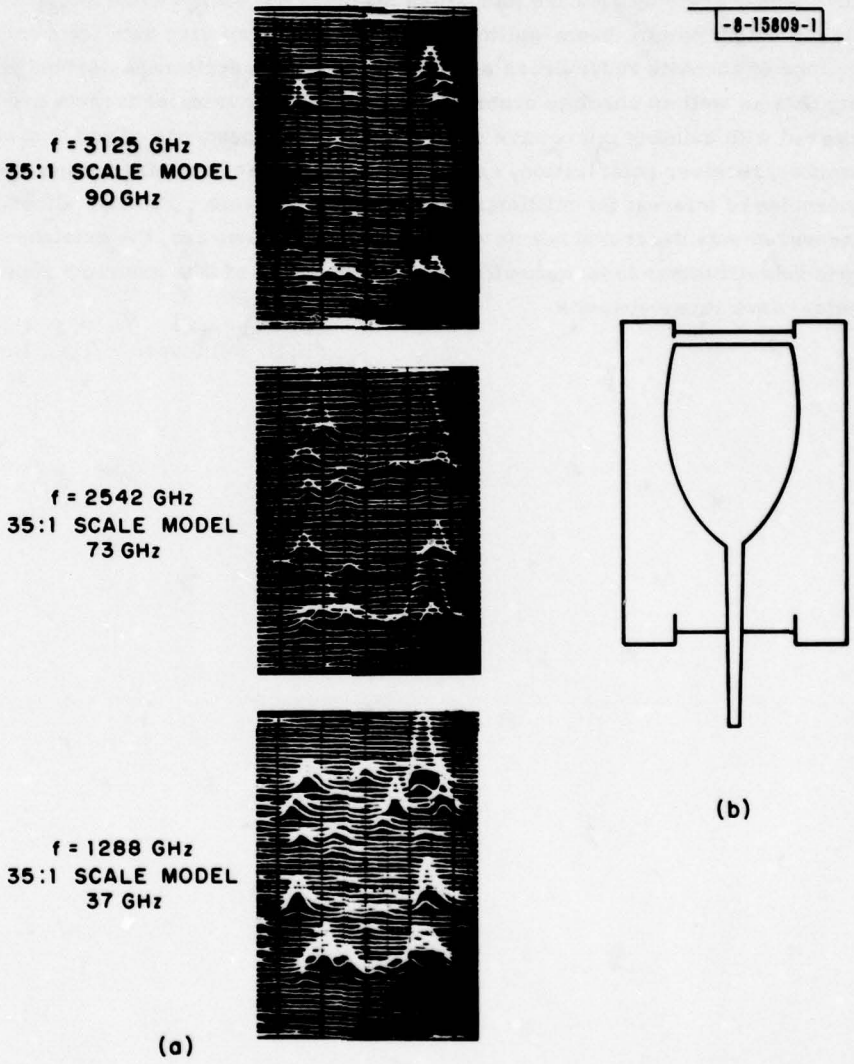


Fig. II-12. (a) Submillimeter images of the model target at the frequencies and orientation indicated. The oscilloscopes axes are driven by transducer voltages representing raster mirror positions. The returning signal is simply added to the vertical input. (b) Outline of the model target at the indicated orientation.

the detail sharpening with increasing frequency, in part as a result of the increase in resolution. The oscilloscope traces demonstrate that the system signal-to-noise ratio is already adequate for obtaining quantitative measurements of the cross sections of individual scatterers on the target. The data shown are only relative intensities and have not been normalized to correct for the variation in output power, beam-splitter efficiency, and spot size with frequency.

Determinations of absolute radar cross sections of individual scatterers derived from calibrated imaging data as well as absolute cross sections of fully illuminated targets are being made and compared with existing microwave data. The known dependence of radar cross sections on transmitter/receiver polarization, resolution element size, and target aspect are being studied at frequencies of interest for millimeter-wave radar systems. Finally, although the preliminary measurements described herein were done with CW sources, the existence of pulsed, optically pumped submillimeter lasers should allow the extension of this modeling approach to pulsed millimeter-wave radar systems.

J. Waldman† P. E. Duffy
H. R. Fetterman T. G. Bryant‡

† Department of Physics, University of Lowell, Massachusetts.
‡ Group 45.

REFERENCES

1. Solid State Research Report, Lincoln Laboratory, M.I.T. (1979:1), p. 19.
2. R. A. McClatchey, R. W. Fenn, J. E. A. Selby, F. E. Volz, and J. S. Garing, "Optical Properties of the Atmosphere (Third Edition)," Environmental Research Paper, No. 411, AFCRL-72-0497 (1972).
3. R. L. Byer and M. Garbuny, Appl. Opt. 12, 1496 (1973).
4. Solid State Research Report, Lincoln Laboratory, M.I.T. (1978:2), p. 11, DDC AD-A061241/6.
5. W. Seiler and C. Junge, J. Geophys. Res. 75, 2217 (1970).
6. R. T. H. Collis and P. B. Russell, "LIDAR Measurement of Particles and Gases by Elastic Backscattering and Differential Absorption," in Laser Monitoring of the Atmosphere, E. D. Hinkley, Ed. (Springer-Verlag, 1976).
7. H. P. Weber and B. C. Tofield, IEEE J. Quantum Electron. QE-11, 368 (1975).
8. G. Winzer, P. G. Möckel, R. Oberbacher, and L. Vité, Appl. Phys. 11, 121 (1976).
9. J.-P. Budin, M. Neubauer, and M. Rondot, Appl. Phys. Lett. 34, 309 (1978).
10. S. R. Chinn and W. K. Zwicker, Appl. Phys. Lett. 31, 178 (1977).
11. G. Huber and H. G. Danielmeyer, Appl. Phys. 18, 77 (1979).
12. M. M. Choy, W. K. Zwicker, and S. R. Chinn, Applied Physics Letters (to be published).
13. M. M. Abraham, C. T. Butler, and Y. Chen, J. Chem. Phys. 55, 3752 (1971).
14. Solid State Research Report, Lincoln Laboratory, M.I.T. (1978:1), p. 20, DDC AD-A056715.
15. S. R. J. Brueck and H. Kildal, Opt. Lett. 2, 33 (1978).
16. Solid State Research Report, Lincoln Laboratory, M.I.T. (1979:1), p. 21.
17. H. Kildal and S. R. J. Brueck, Phys. Rev. Lett. 38, 347 (1977).
18. S. R. J. Brueck, Chem. Phys. Lett. 50, 516 (1977).
19. A. I. Burshtein and S. I. Temkin, Sov. Phys.-JETP 44, 492 (1976).
20. S. I. Temkin and A. I. Burshtein, JETP Lett. 24, 86 (1976).
21. Y. L. Duff, J. Chem. Phys. 59, 1984 (1973).
22. C. M. Penney, L. M. Goldman, and M. Lapp, Nature 235, 110 (1972).
23. S. R. J. Brueck, Chem. Phys. Lett. 53, 273 (1978).
24. G. Levi, M. Chalaye, F. Marsault-Herail, and J. P. Marsault, Mol. Phys. 24, 1217 (1972).
25. S. R. J. Brueck and H. Kildal, Appl. Phys. Lett. 33, 928 (1978).
26. R. C. Miller, Appl. Phys. Lett. 5, 17 (1964).
27. R. W. Hellwarth, in Progress of Quantum Electronics, Vol. 5, J. H. Sanders and S. Stenholm, Eds. (Pergamon Press, New York, 1977), pp. 1-68.
28. K. Krynicki, E. J. Rahkamaa, and J. G. Powles, Mol. Phys. 29, 539 (1975).
29. S. L. Shapiro and H. P. Broida, Phys. Rev. 154, 129 (1967).
30. M. A. Dugay and J. W. Hansen, Appl. Phys. Lett. 15, 192 (1969).
31. Radar Handbook, M. A. Skolnik, Ed. (McGraw-Hill, 1970), p. 27-5.
32. L. A. Cram and S. C. Woolcook, "Review of Two Decades of Experience Between 30 GHz and 900 GHz in the Development of Model Radar Systems," AGARD Conference Proceedings No. 245, Millimetre and Submillimetre Wave Propagation and Circuits, Paper 6, Munich (1978).
33. D. Hodges et al. "Advanced Technology for the MM and Sub MM Wave Region," AGARD Conference Proceedings No. 245, Paper 21, Munich (1978).

III. MATERIALS RESEARCH

A. CALCULATED AND MEASURED EFFICIENCIES OF SHALLOW-HOMOJUNCTION GaAs SOLAR CELLS

We have recently reported[1,2] the fabrication of single-crystal GaAs shallow-homojunction solar cells without $Ga_{1-x}Al_xAs$ window layers that have conversion efficiencies of 21 percent at AM1 (air mass 1). These cells employ an $n^+/p/p^+$ structure, prepared by chemical vapor deposition (CVD), in which surface recombination losses are reduced because the n^+-layer is so thin that most of the carriers are generated in the p-layer below the junction. High-efficiency cells have been fabricated on (100) substrates of both GaAs (Ref. 1) and Ge (Ref. 2). For the same n^+-layer thickness, cells on both substrate materials have the same conversion efficiency, showing that the solar-cell properties of the CVD GaAs layers are the same in both cases. The substitution of Ge for GaAs substrates will permit a major decrease in Ga consumption as well as a significant reduction in cell cost.

We have now utilized a simple analytical model for the shallow-homojunction GaAs solar cells to obtain calculated results in very good agreement with our experimental data for the dependence of external quantum efficiency and conversion efficiency on n^+-layer thickness. The efficiency measurements were made on cells with Ge substrates, but the results would be the same for devices with GaAs substrates.

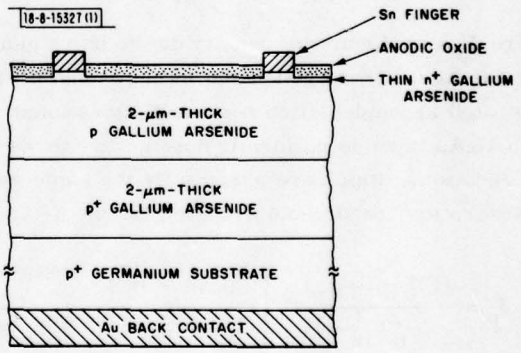


Fig. III-1. Schematic cross section of GaAs shallow-homojunction solar cell on Ge substrate.

The fabrication of the shallow-homojunction cells has been described elsewhere.[1,2] Figure III-1 is a schematic cross section of such a cell on a Ge substrate. The p^+ Ge substrate is highly doped with Ga (8×10^{18} cm^{-3}). The GaAs p^+ buffer layer and p active layer are doped with Zn to 5×10^{18} and 1×10^{17} cm^{-3}, respectively, while the GaAs n^+-layer is doped with S to 5×10^{18} cm^{-3}, the highest S doping level that has been achieved in our CVD system. Quantum and conversion efficiency measurements were made on four cells with areas of about 0.05 cm^2, fabricated side by side on the same wafer. For each cell, measurements were made at several different values of n^+-layer thickness, which were obtained by using a repeated anodization and stripping process[2] to accomplish a step-wise reduction in thickness. For each measurement the n^+-layer was anodized to form an AR coating approximately 850 Å thick.

The theoretical model used for our calculations assumes that one hole-electron pair is generated for each solar photon absorbed. The flow of photogenerated minority carriers across

PRECEDING PAGE BLANK-NOT FILMED

the p-n junction produces a photocurrent consisting of three components. Some of the holes generated in the n^+-layer may be lost by recombination at the GaAs surface as well as by bulk recombination; however, since the heterojunction between the heavily doped p^+ GaAs and Ge does not act as a barrier to hole transport, all the holes reaching the p-n junction should be collected at the contact to the Ge substrate, thus contributing the first component of the photocurrent. Similarly, of the electrons generated in the p and p^+ GaAs layers, those that reach the junction are collected at the contact to the n^+-layer and contribute the second component to the current. Some of the electrons generated in the p^+ GaAs layer can diffuse into the Ge substrate, producing no current, but electrons generated in the p GaAs layer are hindered from entering the p^+ region by the back-surface field (BSF) resulting from the difference in carrier concentration between the p- and p^+-layers. The final component of the photocurrent is due to the minority carriers generated within the junction depletion region; it is assumed that all these carriers are collected because of the large drift field within this region. Although some solar photons with energies less than the GaAs energy gap (1.43 eV) will be absorbed by the Ge substrate, which has a much lower energy gap (0.66 eV), electrons generated in the substrate should not contribute any measurable photocurrent, since in order to reach the p-n junction they would have to overcome a barrier of over 0.7 eV, the difference between the energy gaps of GaAs and Ge.

For the model described, the external quantum efficiency QE_{ext} as a function of wavelength λ is given by

$$QE_{ext}(\lambda) = \frac{J_p + J_n + J_{dr}}{qF(\lambda)} \tag{III-1}$$

where J_p = photocurrent density due to holes generated in the n^+-layer, J_n = photocurrent density due to electrons generated in the p- and p^+-layers, J_{dr} = photocurrent density due to carriers generated in the depletion region, $F(\lambda)$ = photon flux density at λ, and q = electronic charge. If each GaAs layer is uniformly doped, the three photocurrent densities are given by the following equations, which are essentially the same as those listed in Ref. 3 except that different sets of absorption coefficients are used for the n- and p-layers instead of a single set for both types.

$$J_p = \frac{qF(1-R)\,\alpha_n L_p}{(\alpha_n^2 L_p^2 - 1)} \left\{ \frac{(K_p L_p + \alpha_n L_p) - \exp[-\alpha_n x]\left(K_p L_p \cosh\frac{x}{L_p} + \sinh\frac{x}{L_p}\right)}{K_p L_p \sinh\frac{x}{L_p} + \cosh\frac{x}{L_p}} - \alpha_n L_p \exp[-\alpha_n x] \right\} \tag{III-2}$$

$$J_n = \frac{qF(1-R)\,\alpha_p L_n}{(\alpha_p^2 L_n^2 - 1)} \exp[-\alpha_p (x+w)] \left\{ \alpha_p L_n - \frac{K_n L_n \left(\cosh\frac{H'}{L_n} - \exp[-\alpha_p H']\right) + \sinh\frac{H'}{L_n} + \alpha_p L_n \exp[-\alpha_p H']}{K_n L_n \sinh\frac{H'}{L_n} + \cosh\frac{H'}{L_n}} \right\} \tag{III-3}$$

$$J_{dr} = qF(1-R)\exp[-\alpha_n x]\{1 - \exp[-\alpha_p w]\} \tag{III-4}$$

where R = reflectivity of the front surface; α_n, α_p = absorption coefficients of n- and p-layers, respectively; L_p, L_n = minority-carrier diffusion lengths for holes and electrons, respectively; $K_p = S_p/D_p$ and $K_n = S_n/D_n$, where S_p and S_n are the surface recombination velocities for minority holes and electrons, respectively, and D_p and D_n are the minority-carrier diffusion coefficients; x = junction depth (essentially the thickness of the n^+-layer); w = width of depletion region; H' = H − w, where H is the effective thickness of the p-layer. (Although F, R, α_n, and α_p are functions of λ, in the above equations and the following discussion the functional symbol (λ) has been omitted for clarity.)

The values of the nonadjustable parameters appearing in Eqs. (III-2) to (III-4) were obtained as follows. The values used for F were those published[4] for AM1. Values of R were measured on test wafers with an anodic oxide layer 850 Å thick. For α_n and α_p we adopted the values reported[5] for the absorption coefficients of GaAs with $n = 5 \times 10^{18}$ cm^{-3} and $p = 1 \times 10^{17}$ cm^{-3}, respectively. (For convenience, the same values of α_p were used for the p- and p^+-layers, since the actual coefficients for these two doping levels differ only for λ = 0.8-0.9 μm, where the p^+ values are slightly lower.) The value used for the electron diffusion length was L_n = 23 μm, as reported[6] for GaAs with $p = 1 \times 10^{17}$ cm^{-3}; the values calculated for QE_{ext} are quite insensitive to the exact value selected for L_n, as long as the latter is much greater than the thickness of the p-layer. It was assumed that $K_n = 0$, since S_n is expected to be very small because of the confinement of electrons by the BSF. The width of the depletion region was calculated[7] from the carrier concentrations in the n^+- and p-layers. The depletion region lies almost entirely within the p-layer. Therefore the calculated width of the portion within the p-region, 0.13 μm, was adopted as the value of w, and the contribution of holes generated in the n^+ depletion region to the photocurrent density is neglected in Eq. (III-4).

Since L_p, K_p, and H could not be evaluated independently, they were treated as adjustable parameters. A single value for each of these quantities was found by performing computer calculations to achieve the best simultaneous fit to the six sets of experimental data for QE_{ext} obtained in measurements at six different values of n^+-layer thickness. Each of these six values was found by subtracting, from the initial thickness of the grown n^+-layer, the thickness that had been removed by successive anodization and stripping steps.[2] Although the thickness removed was determined quite accurately from the anodization voltages used, the initial n^+-layer thickness was less certain. Therefore this initial thickness was also treated as an adjustable parameter. The initial value giving the best fit to all six sets of QE_{ext} data was 2150 Å, 100 Å greater than the value[2] estimated from the anodization results. The values of n^+-layer thickness used throughout the remainder of this section were obtained by using this best-fit initial thickness.

In Fig. III-2 the calculated curves for QE_{ext} as a function of λ are compared with the experimental points for four values of x. The overall agreement is seen to be excellent, although for x = 450 Å at the shorter wavelengths the calculated quantum efficiency values are somewhat higher than the measured ones. Good agreement was obtained for x = 300 and 1300 Å, the results for which have been omitted from Fig. III-2 for clarity, except that the calculated QE_{ext} values for x = 300 Å are significantly higher than the measured ones for λ < 0.6 μm.

The following adjustable parameter values were used in calculating the QE_{ext} curves in order to give the best fit to experiment: H = 4 μm, L_p = 0.05 μm, and $K_p = 1.7 \times 10^7$ cm^{-1}. An even higher value for H, the effective p-layer thickness, would give a better fit to the QE_{ext}

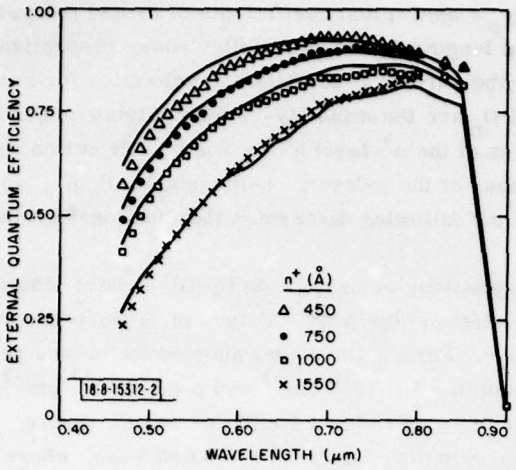


Fig. III-2. External quantum efficiency as a function of wavelength for GaAs shallow-homojunction solar cells with n^+-layer thickness of 450, 750, 1000, and 1550 Å. The solid curves were calculated, while the points were measured.

data for 0.8 to 0.85 μm, but such a value would be meaningless since 4 μm is the total thickness of the p- and p^+-layers. A value closer to the p-layer thickness (2 μm) would be expected because not all the electrons generated in the p^+-layer should reach the p-n junction. This discrepancy suggests that the actual absorption coefficients for the p-layer may be larger than the literature values, since the calculations would yield a smaller value of H if larger values were used for α_p.

The L_p value for the n^+-layer, which was doped with S to 5×10^{18} cm^{-3}, is considerably lower than the values of 0.1 and 0.3 μm reported for GaAs layers doped to the same level with Te (Ref. 8) or Sn (Ref. 9), respectively. The reduction in L_p could be explained if precipitates or defects were present in the n^+-layer as a result of doping the layer with S to a level near the solubility limit. This effect could also explain the fact that the electron Hall mobility measured for the n^+-layer is only about 1000 $cm^2V^{-1}sec^{-1}$, compared to the value of about 2000 $cm^2V^{-1}sec^{-1}$ reported[8] for layers with the same level of Te doping. If it is assumed that the drift mobility of electrons is equal to the Hall mobility, that the ratio of hole mobility to electron mobility in the n^+-layer is 1/20 [a reasonable value for GaAs (Ref. 7)], and that the Einstein relation[7] is applicable, then $D_p = (kT/q)\mu_p = 1.3$ cm^2sec^{-1}. Combining this D_p value with the value obtained for $K_p = S_p/D_p$ gives an estimated surface recombination velocity $S_p \approx 2 \times 10^7$ cm sec^{-1} for the anodized n^+-layer, consistent with the value of 10^7 cm sec^{-1} reported[10] for a bare n GaAs surface.

By using the same parameter values used in the QE_{ext} calculations, we have calculated the maximum conversion efficiency η_{max} at AM1 as a function of n^+-layer thickness for cells with the structure shown in Fig. III-1. The equations employed are given in Refs. 3 and 11. For the values of dark saturation current density J_o appearing in these equations, we used calculated values of the injected current density J_{inj}. For our cells, J_{inj} should closely approximate J_o, since the measured diode factors are close to unity. The values calculated for J_{inj} depend strongly on the value adopted for the intrinsic carrier concentration n_i. In our calculations we used $n_i = 1.8 \times 10^6$ cm^{-3} at 300 K (Refs. 12 and 13).

The dependence of AM1 conversion efficiency on n^+-layer thickness is shown in Fig. III-3, where the measured values of η_{exp} (represented by points) for four different $n^+/p/p^+$ cells are compared with the calculated values of η_{max} (represented by the solid line). With decreasing

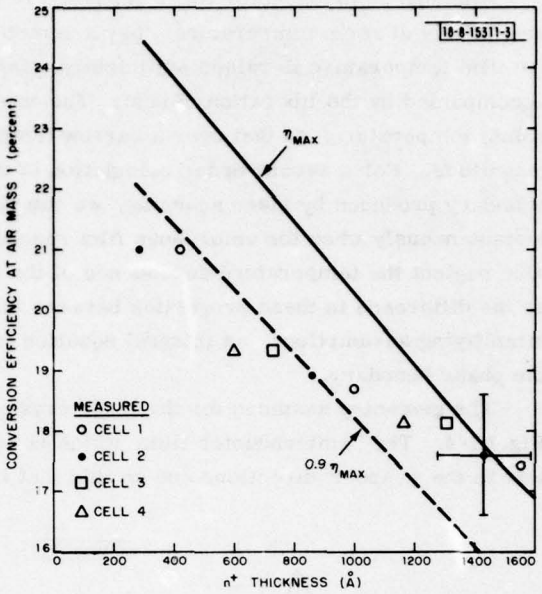


Fig. III-3. Conversion efficiency at AM1 as a function of n^+-layer thickness for GaAs shallow-homojunction solar cells. The measured values are represented by points, the calculated values of maximum conversion efficiency η_{max} and of $0.9\,\eta_{max}$ by solid and dashed lines, respectively.

thickness, η_{max} increases from 17 percent at 1600 Å to 24 percent at 300 Å. Even at the latter thickness, about 7 percent of the total photocurrent is due to the collection of holes generated in the n^+-layer. The η_{max} calculations do not take account of losses resulting from such effects as contact-finger shadowing and reduction in fill factor due to series resistance. Because of such losses, we expect the η_{exp} values for our cells to approximate $0.9\,\eta_{max}$ (represented by the dashed line in Fig. III-3). Within the limits of experimental error this is generally the case, although the η_{exp} values do not appear to decrease as rapidly as η_{max} with increasing n^+-layer thickness.

In summary, by means of calculations based on a simple model we have obtained good fits to the measured values for the external quantum efficiency and conversion efficiency of GaAs solar cells with the shallow-homojunction $n^+/p/p^+$ structure. These calculations have yielded values for several material properties of the GaAs layers composing these cells. Having demonstrated the applicability of the model, we can now use it in optimizing cell design. Preliminary calculations indicate that still higher conversion efficiencies would be obtained for n^+-layers with higher minority-carrier diffusion lengths and lower surface recombination velocities.

J. C. C. Fan
C. O. Bozler
B. J. Palm

B. CALCULATION OF CRYSTALLIZATION FRONT VELOCITY FOR AMORPHOUS SEMICONDUCTOR FILMS SCANNED WITH A CW LASER

In experiments on crystallization of amorphous semiconductor films by scanning with the slit image of a CW laser, we have observed a number of unusual phenomena, including the formation of periodic structural features on the film surface, pulsations of the film temperature during scanning, and runaway crystallization of the entire film following first contact with the laser image. By means of preliminary computer calculations of the crystallization front velocity, we have shown that all these phenomena can be attributed to the liberation of heat accompanying the transformation from the amorphous to the crystalline state.

Although semiconductor films deposited in the amorphous state will remain in this state indefinitely at room temperature, they are metastable with respect to the crystalline form. When the film temperature is raised sufficiently, transformation to the crystalline form takes place, accompanied by the liberation of heat. The transformation rate increases exponentially with absolute temperature, so that over a narrow temperature interval the rate changes by orders of magnitude. For a zeroth-order calculation of the motion of the amorphous-crystalline phase boundary produced by laser scanning, we can therefore assume that the transformation occurs instantaneously when the amorphous film reaches a sharply defined critical temperature T_c. We also neglect the temperature dependence of the optical and thermal properties of the film, as well as the difference in these properties between the amorphous and crystalline states. With these simplifying assumptions, an integral equation formalism[14] can be used to describe the motion of the phase boundary.

The geometry assumed for the laser crystallization calculation is shown schematically in Fig. III-4. The semiconductor film, which is deposited on a thick substrate, is of infinite extent in the $\hat{y}$ and $\hat{z}$ directions and so thin that its temperature is constant in the $\hat{x}$ direction.

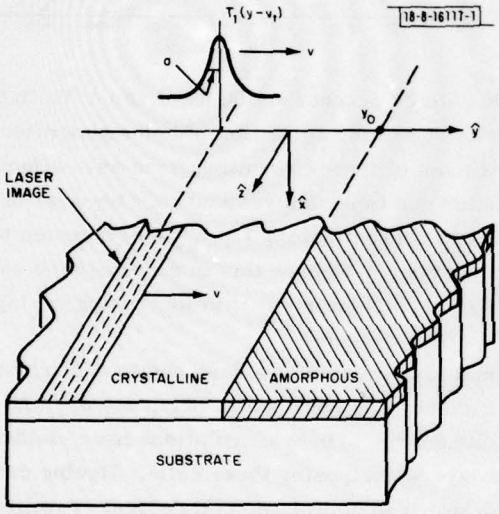


Fig. III-4. Schematic diagram of geometry assumed for theoretical description of a laser crystallization experiment.

The laser slit image is of infinite length in the $\hat{z}$ direction and moves at a velocity v from left to right in the $\hat{y}$ direction. At $t = 0$, the phase boundary is located at y_o, with the crystalline phase to the left ($y < y_o$) and the untransformed amorphous phase to the right ($y > y_o$). Prior to $t = 0$, the laser image is moving through the region $y < y_o$, carrying with it a steady-state temperature profile $T_1(y - vt)$. At $t = 0$, the temperature at the phase boundary reaches T_c and the boundary begins to move toward the right, with heat being liberated at a rate per unit volume of $L\rho\dot{Y}(t)$, where L is the latent heat of crystallization of the semiconductor, ρ is its density, and Y(t) is the position of the boundary. As a further simplification, the heat diffusing into the substrate and the heat lost by radiation from the film surface are neglected. Then the temperature T(y, t) at any point along the film at time t is given by the integral relation

$$T(y,t) = T_1(y - vt) + \frac{L}{C}\left[\frac{1}{2(\pi\kappa)^{1/2}}\right]\int_o^t \frac{\dot{Y}(t')}{(t-t')^{1/2}}\exp\left\{\frac{-[y - Y(t')]^2}{4\kappa(t-t')}\right\}dt' \qquad \text{(III-5)}$$

where C is the specific heat of the film, $\kappa = K/C\rho$ defines its thermal diffusivity, and K is its thermal conductivity. An integral equation for Y(t) can be obtained by using the condition that the temperature at the phase boundary is T_c, or

$$T[Y(t),\ t] = T_c \quad . \tag{III-6}$$

For purposes of calculation, it is convenient to rewrite Eq. (III-5) in the frame of reference moving with the laser image. For this purpose we introduce the position variable $u(t) = y(t) - vt$, where u(t) is measured from the center of the laser image as origin. The temperature T_1 is modeled in the form

$$T_1(u) = T_b + T_L\, e^{-(u/a)^2} \quad , \tag{III-7}$$

where T_b is a uniform, time-independent background temperature, and the temperature contribution due to the laser is described by a Gaussian of width a.

Finally, introducing normalized quantities we can write the integral equation for the motion of the phase boundary as

$$1 = \alpha\, \exp\{-[S(\tau)]^2\} + \eta \int_0^{\tau} \frac{\dot{S}(\tau') + V}{(\tau - \tau')^{1/2}}\, \exp\left\{\frac{-[S(\tau) - S(\tau') + V(\tau - \tau')]^2}{\tau - \tau'}\right\} d\tau' \tag{III-8}$$

where $\alpha = T_L/(T_c - T_b)$, $\eta = L/C\pi^{1/2}(T_c - T_b)$, $\tau \equiv 4\kappa t/a^2$, $V \equiv av/4\kappa$, $S \equiv U/a$, $\dot{S}(\tau') \equiv dS(\tau')/d\tau' = (1/a)\,[dU(t')/dt']\,(dt'/d\tau')$, and U is the position of the phase boundary measured from the center of the laser image.

Equation (III-8) has been solved numerically by a preliminary method to obtain S as a function of τ for representative values of α, η, and V, with the boundary conditions that $\dot{S}(\tau) = 0$ at $\tau = 0$ and that S(0) is given by $1 = \alpha\, \exp\{-[S(0)]^2\}$. Figure III-5 shows plots of S vs τ for $\alpha = 1.5$, $V = 1.52$, and three values of η. For each value of η, S initially increases rapidly (i.e., the amorphous-crystalline phase boundary moves quickly ahead of the advancing laser image) because the heat liberated by the phase transformation raises the temperature ahead of the boundary, accelerating the forward motion of the boundary. As the boundary moves away from the laser image, the contribution of the laser to the temperature ahead of the boundary decreases rapidly. For $\eta = 0.19$, the heat liberated by the transformation is then insufficient to keep the boundary velocity greater than the laser velocity, and S therefore decreases. With the resulting approach of the laser image toward the boundary, the laser contribution to the boundary temperature increases, eventually becoming sufficient to once more accelerate the motion of the boundary and causing S to increase again. This cycle is repeated indefinitely, resulting in the oscillations in S seen for $\eta = 0.19$ in Fig. III-5.

As η increases, the heat liberated by the phase transformation increases relative to the heat required to raise the film temperature from the background temperature T_b to the critical temperature T_c. Therefore, the initial acceleration of the phase boundary is greater, and the boundary moves farther beyond the laser image before it decelerates. This trend is illustrated by the initial portion of the calculated curve for $\eta = 0.35$ in Fig. III-5. The remainder of this curve has been dotted because the solution obtained beyond $\tau = 0.085$ is nonphysical. Thus, the decrease in the calculated value of S for $0.085 < \tau < 0.15$ corresponds to a backward motion of the phase boundary, which would imply reconversion of the crystalline phase to the amorphous

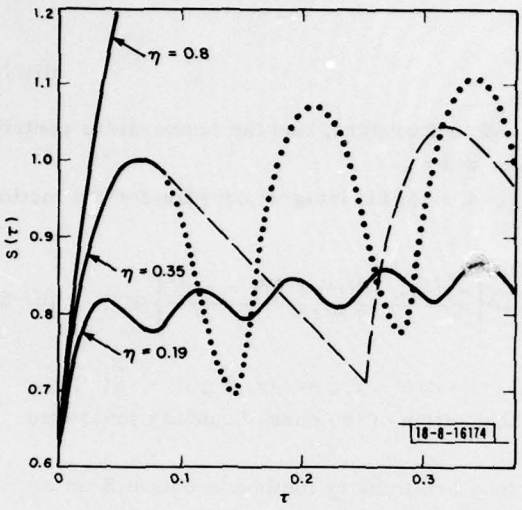


Fig. III-5. Calculated curves of $S(\tau)$ vs τ for parameter values $\alpha = 1.5$, $V = 1.52$, with $\eta = 0.19$, 0.35, and 0.8.

state and a consequent reabsorption of the latent heat. In reality the boundary comes to rest at $\tau \sim 0.085$ and then remains fixed until the laser image approaches closely enough to again initiate forward motion. This behavior is indicated schematically by the dashed curve in Fig. III-5, the linear portion of which covers the time interval when the boundary is fixed and therefore has the slope $|\dot{S}| = V$. (It should be noted that during this time interval the boundary temperature initially drops below T_c and then increases to T_c, at which time the boundary begins to move forward. For the motion represented by the solid lines in Fig. III-5, the temperature at the boundary is always T_c.) The physically correct solution for the boundary motion can be obtained by solving Eq. (III-8) with the additional constraint that whenever $[\dot{S}(\tau') + V] \leqslant 0$, this quantity should be set equal to zero.

When η becomes large enough, the heat liberated during crystallization is sufficient to sustain the transformation, causing the boundary to "run away" from the laser image. This situation, which is illustrated by the curve for $\eta = 0.8$ in Fig. III-5, corresponds to the observation that the entire film is crystallized following first contact with the laser image.

The zeroth-order model described does not predict observable structural changes in the laser-treated films, since optical and thermal properties are assumed identical for the amorphous and crystalline phases. Nevertheless, the qualitative features of laser crystallization experiments can be understood on the basis of the model calculation if the more realistic properties of the films are taken into account in the next approximation. Among the most important considerations is the fact that the rate of conversion of amorphous to crystalline material is a

smooth function of temperature, rather than occurring abruptly at T_c. The actual morphology of different regions of a laser-treated film can be expected to depend on their rates of transformation and therefore on their thermal history. Furthermore, crystalline material absorbs less laser energy than amorphous material, so that even though all the material is exposed directly to the laser radiation after the phase boundary has passed by, this direct exposure may not further modify the morphology of the film. This suggests that the periodic structural features observed on laser-crystallized films can be attributed to periodic fluctuations in the velocity of the phase boundary like those shown by the curves for η = 0.19 and 0.35 in Fig. III-5. If so, comparison of these curves indicates that the features should be more widely spaced and more prominent for higher values of η (i.e., higher T_b). Preliminary observations on laser-crystallized films of Ge on fused silica appear to be consistent with this prediction. Furthermore, for sufficiently high values of η, the calculated phase boundary alternately moves rapidly and comes to rest, resulting in large fluctuations in the rate of heat liberation and therefore in temperature. This could explain the observation of periodic fluctuations in the color temperature of films during laser crystallization.

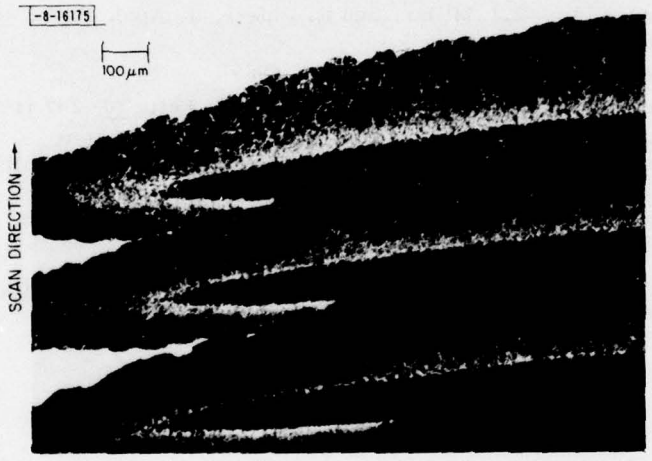


Fig. III-6. Microphotograph of periodic structure observed after laser crystallization of a film of Ge on a fused silica substrate.

Figure III-6 is a photomicrograph showing structural features with a spatial period of ~300 μm produced during laser crystallization of an amorphous Ge film on a fused silica substrate. Assuming that such features are due to oscillations in phase boundary velocity like those shown in the curves of Fig. III-6, their spatial period ΔY can be estimated from these curves by using the relationship $\Delta Y/a = V\Delta\tau$, where $\Delta\tau$ is the temporal period of the velocity oscillation. For η = 0.19 and 0.35, the values of $\Delta Y/a$ are 0.1 and 0.4, respectively. A rough estimate of the parameter a for Ge on fused silica is 10^{-1} cm, yielding ΔY values of 100 and 400 μm, respectively. In view of the preliminary nature of the calculations, this degree of agreement with the experimental observations is encouraging.

H. J. Zeiger J. C. C. Fan
B. J. Palm R. L. Chapman

REFERENCES

1. J.C.C. Fan, C.O. Bozler, and R.L. Chapman, Appl. Phys. Lett. 32, 390 (1978).
2. C.O. Bozler, J.C.C. Fan, and R.W. McClelland, Proceedings of the 7th International Symposium on GaAs and Related Compounds, St. Louis, 1978 (Institute of Physics, London, 1979), p. 429.
3. H.J. Hovel, "Solar Cells," Vol. 11 of Semiconductors and Semimetals (Academic, New York, 1975).
4. M.P. Thekaekara, Conference of COMPLES, Dahran, Saudi Arabia, November 1975.
5. H.C. Casey, Jr., D.D. Sell, and K.W. Wecht, J. Appl. Phys. 46, 250 (1974); H.C. Casey, Jr. and F. Stern, J. Appl. Phys. 47, 631 (1976).
6. R.J. Nelson, Proceedings of the 7th International Symposium on GaAs and Related Compounds, St. Louis, 1978 (Institute of Physics, London, 1979).
7. S.M. Sze, Physics of Semiconductor Devices (Wiley, New York, 1969).
8. H.C. Casey, Jr., B.I. Miller, and E. Pinkas, J. Appl. Phys. 44, 1281 (1973).
9. C.J. Hwang, J. Appl. Phys. 40, 3731 (1969).
10. H.C. Casey, Jr. and E. Buehler, Appl. Phys. Lett. 30, 247 (1977).
11. M.P. Godlewski, C.R. Godlewski, C.R. Baraona, and H.W. Brandhorst, Jr., Conference Record of the 10th IEEE Photovoltaic Specialists, Palo Alto, California, November, 1973.
12. D.D. Sell and H.C. Casey, Jr., J. Appl. Phys. 45, 800 (1974).
13. D.C. Look, J. Appl. Phys. 48, 5141 (1977).
14. H.S. Carslaw and J.C. Jaeger, Conduction of Heat in Solids (Oxford University Press, 1959), p. 293.

IV. MICROELECTRONICS

A. CRYSTALLOGRAPHIC ORIENTATION OF SILICON ON AMORPHOUS SUBSTRATE USING ARTIFICIAL SURFACE-RELIEF GRATING AND LASER CRYSTALLIZATION

In earlier work, surface-relief gratings with square-wave cross section in amorphous SiO_2 were used to induce oriented growth of KCl crystallites grown from a water solution,[1] and to align overlayer films of nematic and smectic A liquid crystals.[2-4] In that work and other papers[5,6] the authors speculated that control of overlayer crystallographic orientation by means of artificial surface-relief structure should be applicable to a broad range of overlayer/substrate combinations and deposition methods. Here we report uniform crystallographic orientation of thin silicon films on amorphous fused silica substrates, achieved by laser crystallization of amorphous silicon deposited over a surface-relief grating in the substrate. We propose that such examples of orientation induced by artificial surface patterns be called "graphoepitaxy."†

A theoretical model[3] predicts that film formation methods that yield textured polycrystalline films (i.e., films in which the individual crystal grains have one particular plane parallel to the substrate surface and random orientation otherwise) on smooth amorphous substrates should yield uniformly oriented films if such film formation is carried out over an appropriate surface-relief structure in the amorphous substrate. For example, polycrystalline films with (100) texture [i.e., with grains having (100) planes parallel to the substrate surface but random orientation in the surface plane] should become uniformly oriented on a surface-relief grating with square-wave cross section if the spatial period of the grating is small compared with the normal grain size. Specifically, the model, which is based on equilibrium thermodynamics, states that such uniform orientation is a configuration of minimum free energy. Polycrystalline films of (111) texture, on the other hand, would require a relief structure having facets that intersect at 70.5° and/or 109.5°. *Relief structures with square-wave cross section are more easily* fabricated using current techniques,[3,7,8] and thus one is led to seek film formation methods that yield (100) or (110) textured silicon. It is known that laser crystallization of silicon films yields grains several micrometers in diameter.[9,10] We found that under certain conditions laser crystallization of amorphous silicon over fused silica yields a nearly perfect (100) texture.

Several experiments were performed to determine the texture of laser-crystallized amorphous and polycrystalline silicon, deposited by a variety of methods, on optically polished fused silica substrates. In some cases the polished fused silica was coated with SiO_2 deposited by a CVD process. With amorphous silicon films 500-nm thick, deposited at 610°C in a commercial CVD reactor‡ using the reaction $SiH_4 \xrightarrow{N_2} Si + 2H_2$, we were able to obtain 100 percent of a (100) texture after laser crystallization, as determined by x-ray diffractometry. The maximum deviation of (100) from the substrate plane was about 3°, as determined by reflection electron diffraction (RED). With silicon deposited by thermal evaporation and by the reaction $SiH_4 \rightarrow Si + 2H_2$ in a low-pressure CVD reactor‡ we observed 100 percent (111) and relatively weak (100) textures, respectively. The laser crystallization was done in air at room temperature using an argon-ion laser, operating multiline at a power level between 6 and 7 W, focused with a 60-mm focal length lens placed 45 mm from the silicon film. For a single linear scan,

† From the Greek: "grapho" – to write or incise; "epi" – upon; "taxis" – arrangement, order.
‡ General Signal/Tempress, Sunnyvale, California.

this beam produced a band of crystallization about 380 μm wide. Samples were scanned past the beam at 10 mm/sec or slower in a raster fashion, with successive horizontal scans stepped vertically by 12 μm. After multiple raster scans of a silicon film in the laser beam, polycrystalline grains grew to 10 to 100 μm diameter, indicating that uniform crystollographic orientation should be obtainable with square-wave gratings having spatial periods of several micrometers.

To obtain square-wave gratings in fused silica substrates we first coated the substrates with a film of chromium 20 nm thick. Using conformable photomask lithography,[11] a 3.8-μm spatial-period grating was then exposed and developed in AZ 1350B photoresist,† and the chromium etched in a chemical etchant. After removal of the photoresist, a square-wave grating was etched into the fused silica by reactive-ion etching in CHF_3 gas using the chromium grating as a mask.[3,7,8] Finally, the chromium was removed in a chemical etchant. This procedure yields square-wave gratings with flat tops, flat bottoms, and sidewalls that deviate a maximum of about 6° from the vertical. The radii of curvature at the corners where the sidewalls join the tops and groove bottoms are about 5 nm. The deviation of a sidewall from an ideal planar facet depends primarily on the edge ripple in the original photomask and any additional smoothing or roughening that occurs during the chemical etching of the chromium. Typically the deviation is about ±100 nm. In the experiments reported here groove depths were 19, 60, and 100 nm. Substrates were cleaned just prior to depositing silicon on them, the final cleaning step being irradiation for about 40 min. in air with a far-UV lamp.[12] The lamp generates ozone and is very effective in removing any residual organic contamination.

For the crystallographic orientation experiments, about 500 nm of amorphous silicon was deposited by the CVD process,‡ referred to above, over fused silica substrates 1.5 mm thick and 38 mm in diameter. The 3.8-μm spatial-period grating was 100 nm deep and covered a square area about 15 mm on a side. The silicon was laser crystallized, both inside and outside the grating area (using the scanning procedure described above), at laser powers of 6 and 7 W. After a single raster scan at 6 W, the amorphous silicon became polycrystalline, with (100) texture and grains 10 to 20 μm in diameter, but no orientation relative to the grating was measurable. After a second raster scan, grains had grown to about 100 μm dia., and there was a definite preferred orientation relative to the grating as determined by RED. After four raster scans, a nearly perfect orientative relation to the grating was obtained, where the ⟨100⟩ directions in the silicon are parallel to the grating and perpendicular to the substrate surface, as illustrated schematically in Fig. IV-1(b). To verify that the grating geometry (and not the direction of the laser scan) determines the silicon orientation, scans were made parallel, perpendicular, and at 45° to the grating. Orientation was found to be independent of laser scan direction. As depicted in Fig. IV-1(a), the deposit of amorphous silicon conforms to the contour of the underlying grating. With laser crystallization, however, there is substantial redistribution of material; the top surface of the silicon becomes roughened but it is generally planar with no evidence of even a shallow grating. Outside the grating area the film consists of single crystal grains, 10 to 100 μm in diameter, that have a (100) texture, with random orientation in the plane of the substrate. Figure IV-2 shows a comparison of the RED patterns obtained inside and outside the grating area. The small arcs in Fig. IV-2 indicate a slight deviation

† Shipley Company, Newton, Massachusetts.

‡ General Signal/Tempress, Sunnyvale, California.

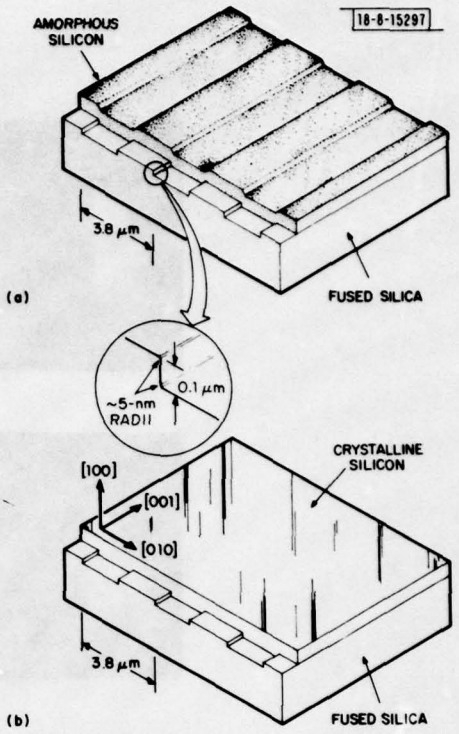


Fig. IV-1. Schematic illustration of (a) amorphous silicon film deposited by a CVD process over a surface-relief grating in fused silica and (b) uniformly oriented film of silicon obtained by laser crystallization of amorphous silicon over relief structure. Note that in (b) the top surface of the silicon does not follow the contour of the grating, as in (a). In practice, the surface of the silicon in (b) has a roughness of several 10 nm.

of (100) texture from one area in the film to another. Such deviation is present both inside and outside the grating area.

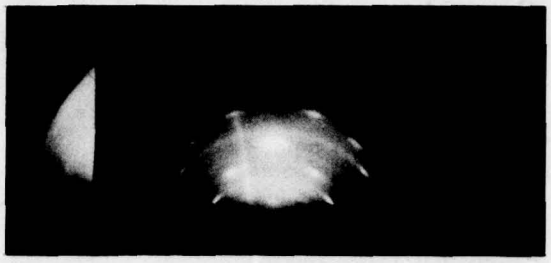
Figure IV-3 shows a transmission diffraction pattern taken in a transmission electron microscope of a silicon film laser crystallized over the grating. The silicon was separated from the fused silica substrate by immersion in a HF solution. The Kikuchi lines in the diffraction pattern indicate a highly ordered crystalline structure.[13]

If the laser power is increased to 7 W, grains having a variety of shapes up to 200 μm dia. form on the first raster scan, but no crystallographic orientation is observed in the grating area. This absence of orientation persists despite repeated scans. Removal of the silicon in hydrazine indicates some damage to the grating at the 7-W power level. Also, at 7 W the silicon appears to be melted by the laser irradiation.

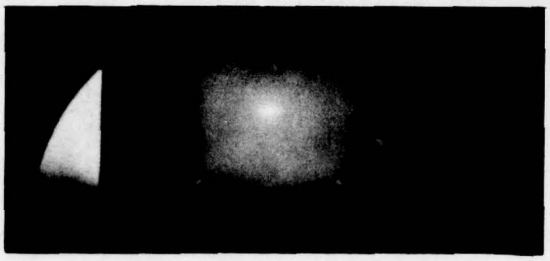
The cross-sectional profile of the grating plays an important role in controlling crystallographic orientation. If the depth of the grating is reduced to 60 nm, the crystallographic orientation degrades somewhat, and at a depth of 19 nm no evidence of orientation relative to the grating is observed by RED. If the bottom corners of the grating are rounded to a radius of curvature of about 80 nm, the orientation effect of the grating is substantially degraded. This is understandable qualitatively from the theoretical model,[3] and is in agreement with similar results obtained with KCl where orientation would not occur on gratings with rounded corners.[3]

We have demonstrated uniform crystallographic orientation of silicon films on amorphous fused silica substrates achieved by laser crystallization over a surface-relief grating with

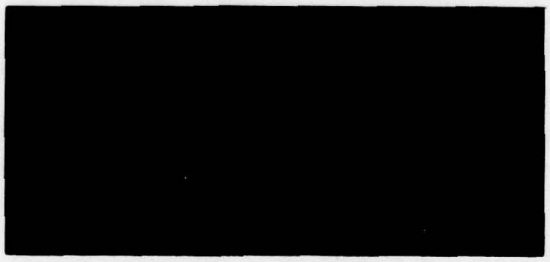
P240-243



(a)



(b)



(c)

Fig. IV-2. (a) RED pattern showing the (100) texture of laser-crystallized silicon film on smooth amorphous fused silica substrate. Lengths of the arcs in the pattern indicate the maximum deviation of the (100) planes from parallel with the substrate is about 3°. Pattern is independent of rotation about the substrate normal, indicating absence of any in-plane orientation. (b) RED pattern of silicon film laser crystallized over a 3.8-μm spatial period, 100 nm deep, square-wave grating in amorphous fused silica. Electron beam is parallel to the grating lines. Observed (100) pattern indicates uniformly oriented silicon having ⟨100⟩ directions parallel to the grating lines and perpendicular to the substrate surface. (c) RED pattern of same sample as in (b) but with electron beam at 45° to the grating lines. Diffraction pattern is (110). Appearance of arcs rather than spots in (b) and (c) indicates the film consists of single-crystal regions where the (100) plane deviates a maximum of about 3° with respect to the substrate surface.

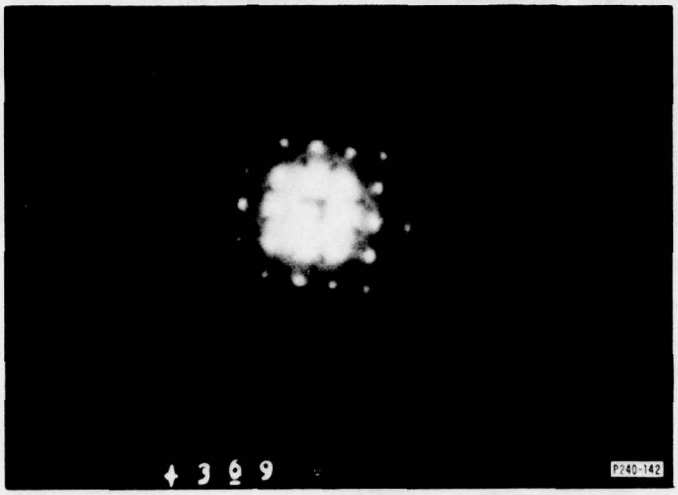


Fig. IV-3. Transmission electron diffraction pattern of 500-nm-thick silicon film laser crystallized over a 3.8-μm period square-wave grating in amorphous fused silica. Electron beam was perpendicular to silicon film yielding a (100) diffraction pattern. Kikuchi lines visible in the pattern indicate a high degree of crystalline perfection.

square-wave cross section. This opens the possibility of new methods of preparing films for microelectronic devices and solar cells.

M. W. Geis
D. C. Flanders
H. I. Smith

B. CHARGE-COUPLED DEVICES: SAW/CCD PROGRAMMABLE MATCHED FILTER

We report here a new device, the SAW/CCD programmable matched filter, which is capable of correlating an analog SAW signal of up to 40-MHz bandwidth and 3.5-μsec duration against 300 samples of an analog reference previously loaded into a CCD shift register. The programmable matched filter is the third analog signal processing function to be demonstrated by this new class of integrated SAW/CCD devices. By adding the programmable matched filter to the previously reported buffer memory[14] and accumulating correlator,[15] we have a family of unique devices which combines the wide bandwidth of the SAW with the long and flexible time-handling capability of the CCD, and thereby promises significant advantages over other technologies in many signal processing applications.

The construction details for this device are similar to those reported earlier for the SAW/CCD fast-in, slow-out buffer memory.[16] A schematic diagram of the programmable matched filter is shown in Fig. IV-4. It consists of a 300-stage CCD shift register with parallel outputs connected to an array of 300 sampling fingers on a p-type silicon substrate which is in close proximity (typically 350 nm) to a $LiNbO_3$ delay line. The RF piezoelectric fields associated with the surface wave are picked up by the sampling fingers, each of which has a DC bias previously set by the CCD-loaded reference pattern. Nonlinearities in the silicon effectively multiply the RF and DC potentials, and the local product terms are capacitively coupled to and summed by the output electrode, thereby producing the desired cross-correlation output.

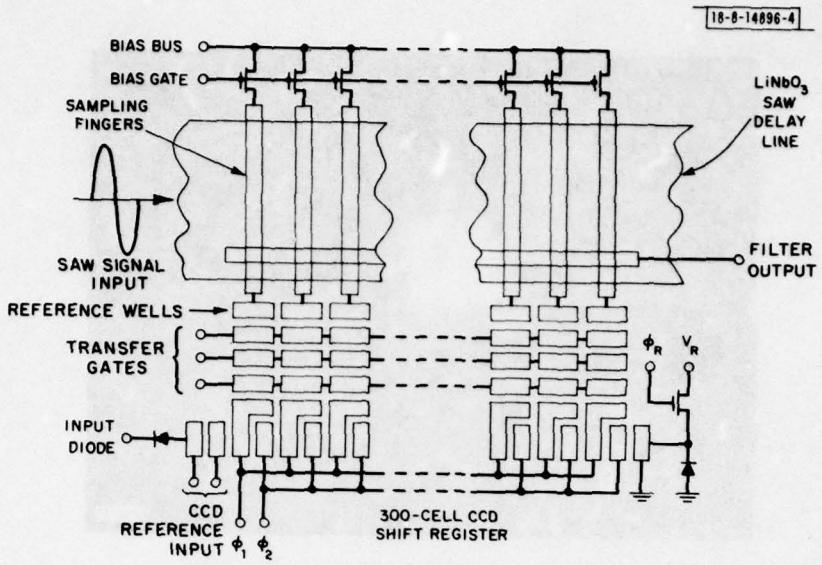


Fig. IV-4. Schematic diagram of a SAW/CCD programmable matched filter.

This output electrode is a 0.25-mm-wide Al strip deposited on the $LiNbO_3$ outside the acoustic beam so as not to distort the SAW phase fronts. Its height is approximately 50 nm less than the spacer-rail height; thus it is gap-coupled to the sampling fingers. Incorporation of the output electrode is the one fabrication detail required for the new device that was not needed for the buffer memory. Electrical differences between the modes of operation for the devices, however, are substantial.

The acoustoelectric interaction utilized for the buffer memory is a linear one, while that employed in the matched filter is nonlinear. Furthermore, as discussed below, the matched filter is a slow-in, fast-out device, in contrast to the fast-in, slow-out buffer reported earlier.

The sequence for matched-filter operation can be explained by reference to Fig. IV-4. Prior to the application of an input signal the sampling fingers are precharged to an appropriate potential by means of the linear array of enhancement-mode MOS transistors, shown at the top of Fig. IV-4. After the biasing transistors are turned off, allowing the sampling fingers to float, a reference voltage waveform is applied across the input gates while the input diode is pulsed at the CCD clock rate, allowing analog samples of reference charge to enter the CCD in the familiar "fill-and-spill" scheme.[17] Serial clocking of the shift register is halted once the 300 φ_1 wells of the CCD contain the desired spatial charge pattern. Charge from each φ_1 well is then transferred through a set of transfer gates to the well associated with the corresponding sampling finger, resulting in a spatial variation of the initially uniform potential on the array of sampling fingers.

In effect this process biases 300 independent varactors which perform the required multiplication between the reference charges and the RF fields that accompany a SAW signal as it propagates through the 3.5-μsec-long interaction region. The silicon nonlinearities, previously exploited in the SAW/CCD accumulating correlator,[15] are characteristic of both the drain regions of the bias transistors as well as the MOS regions underlying the sampling fingers. Optimization

of the nonlinear acoustoelectric interaction is afforded by adjustment of the uniform finger bias (as described earlier) to control the space-charge layer underlying the sampling array. The cross correlation between the SAW signal and CCD reference is obtained by summing the resultant local products on the output electrode. For the special case in which the SAW signal is an impulse, the output will represent a time-compressed serial scan of the reference pattern, in effect producing a slow-in, fast-out buffer memory.

This collinear parametric interaction may be described in frequency-wavevector (ω, k) space[18] simply as the product of the (ω, k) signal wave with the (0, $-$k) reference pattern to produce a correlation at (ω, 0). The matching of the wavevectors over a 40-MHz signal bandwidth is achieved with precisely the same sampling scheme as was implemented and reported for the buffer memory. In brief, the CCD cell size of 40.6 μm defines an effective sampling frequency f_s of 85.7 MHz for the acoustoelectric interaction, and therefore the signal bandwidth which can be match-filtered without sampling ambiguities is in the range 85.7 to 128.6 MHz (f_s to 3/2 f_s). In order to process the information contained on a SAW input at an RF carrier f_c within this band, the reference pattern on the 300 fingers must be at the matcing spatial frequency $(f_c - f_s)/(3480$ m/sec) which, for the 100-kHz clock rate used in the CCD shift register, requires an audio reference waveform in the 0- to 50-kHz range.

The prototype device has been programmed and successfully operated as a matched filter for a variety of signals including CW tone-bursts, linear-frequency-modulated waveforms, and biphase-modulated Barker codes. Performance of the prototype device to data has been most adequately tested by a 13-bit Barker sequence[19] (+++++--++-+-+) which would produce, in an ideal matched filter, a symmetric cross-correlation envelope consisting of a strong central peak and 12 sidelobes with a peak-sidelobe amplitude ratio of 1/13. The actual device performance is shown in Fig. IV-5, which is an oscillograph of the cross correlation of a 3.25-μsec-long 13-bit Barker code signal on a 107.2-MHz carrier frequency with a 13-bit Barker code reference initially loaded into the CCD on the matching 25-kHz carrier. For the signal input power at the 1-dB acoustic compression point of 27 dBm, the correlation peak is at a power level of -41 dBm, which is substantially above the -98-dBm thermal noise in a 40-MHz bandwidth. In future devices the peak output power could be increased by 10 dB and the dynamic range raised over the present 57-dB limit by increasing the CCD charge-handling capability so

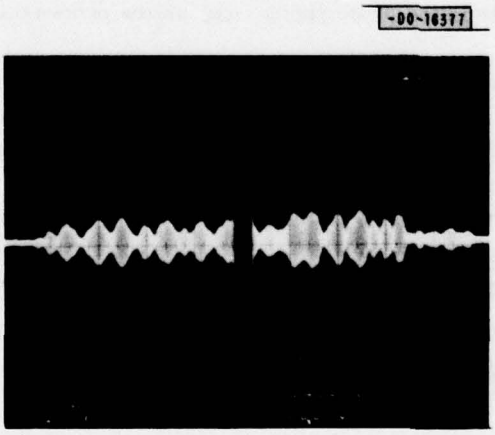


Fig. IV-5. Oscillograph of matched filter operation for a 13-bit Barker-encoded signal 3.25 μsec in length. Signal carrier frequency is 107 MHz while the CCD-controlled reference waveform was entered at a 100-kHz rate.

that it can more effectively charge the sampling fingers. (Currently the finger-to-φ_1 well capacitance ratio is about two.) Although the 3-dB full width of the peak matches the 250-nsec bit time as expected, the sidelobes are irregular with poorly defined nulls, and the peak-to-sidelobe ratio is only −14.5 dB as compared with the theoretical −22.3 dB.

Such signal-dependent spurious sidelobes are not uncommon in acoustoelectric devices, and are typically due to the detection by the silicon circuit of bulk acoustic waves generated at the input transducer.[20] Spurious sidelobes due to such bulk waves can be suppressed to a level at least 35 dB below the correlation peak by appropriate design of the delay line. Such suppression techniques have been successfully implemented in a Schottky-diode/$LiNbO_3$ memory correlator[21] structure and need not be discussed further here.

For the prototype SAW/CCD an additional spurious signal arises from a transducer-like detection of the SAW signal by the sampling finger array. This response is predictably of $\sin x/x$ character, where $x = 300\,\pi(f_c - f_s)/f_s$ is the normalized frequency excursion; for $f_c \leqslant 94$ MHz it contributes spurious sidelobes above those caused by bulk-wave generation. Clearly, an optimized matched-filter device would require suppression of this non-programmable transducer effect which, near the sampling frequency, competes with the CCD programmable filter output.

Finally there is, in addition, a spurious response not shown in the oscillograph, resulting from direct capacitive coupling between the signal transducer and the output electrode. In future devices this unwanted signal can be reduced to an insignificant level by introducing sufficient physical separation between the input transducer and the output electrode.

Ultimately the quality of matched-filter operation will be dependent upon both the suppresion of spurious sidelobes discussed above as well as the maintenance of phase and amplitude fidelity of the reference pattern retained by the sampling fingers. Holding time for the reference is limited by the thermal generation or leakage current in the n^+p drain-substrate junction of the bias transistors. Decay of the reference leads to a 3-dB loss in the correlation peak 1 sec after programming. This device, therefore, offers an excellent duty factor with only 6 msec currently required for refreshing or reprogramming the reference. Because CCD clocking rates of 5 MHz are not unreasonable, the writing time would in fact be reduced to about 120 μsec. As discussed elsewhere,[22] inhomogeneities in the silicon generate fixed-pattern noise and hence corrupt the reference potentials. A quantitative measure of the small degradation in signal processing gain due to such defects is not possible in the prototype device, as the processing gain is limited by bulk-wave effects.

The performance of this SAW/CCD programmable matched filter is given in Table IV-1. In summary, we have demonstrated an important analog signal processing function in an integrated SAW/CCD structure. The main feature of this device is that it can correlate wide bandwidth analog signals of up to 300 time-bandwidth products against electronically controlled reference waveforms. This unique hybrid structure makes possible real-time processing of wideband inputs combined with low-speed, CCD programmable reference patterns. The low-speed CCD reference input is compatible with high-density, low-cost integrated circuits for storing a set of reference waveforms.

R. W. Ralston
D. L. Smythe

TABLE IV-1 SAW/CCD PROGRAMMABLE MATCHED FILTER	
Signal Input Center Frequency	107 MHz
Signal Input Bandwidth	40 MHz
CCD Clock Rate	100 kHz
Reference Input Center Frequency	25 kHz
Reference Input Bandwidth	50 kHz
Signal Input Duration	3.5 μsec
Reference Holding Time	1.0 sec
Maximum Input Power	27 dBm
Maximum Output Power	−41 dBm
Dynamic Range over kTB	57 dB
Spurious (bulk wave) Sidelobes	−14 dB
Time-Bandwidth Product	300

C. CCD PROGRAMMABLE TRANSVERSAL FILTER

A 16-tap CCD transversal filter (Fig. IV-6) with tap weights programmable as 4-bit digital words has been fabricated and tested. The device has been successfully used as a programmable matched filter for a chirp signal. The matched-filter output has a dynamic range of 50 dB.

The tap weights (h_n) in this device are represented in 2's complement notation, i.e.,

$$h_n = \sum_{k=1}^{3} a_{k,n} 2^{-k} - a_{o,n} \qquad n = 0, 1, \ldots 15 \tag{IV-1}$$

where k is the bit position (k = 0 is the most significant bit and is handled separately as described below), n is the tap number, and $a_{k,n}$ is the weighting of the k^{th} bit of the n^{th} tap word and is equal to 0 or 1. The filter output can be written as

$$V_{out}(mT_c) \simeq \sum_{n=0}^{15} \sum_{k=1}^{3} a_{k,n} 2^{-k} V_{in}[(m-n)\,T_c] - \sum_{n=0}^{15} a_{on} V_{in}[(m-n)\,T_c] \tag{IV-2}$$

where $T_c = 1/f_c$, f_c is the CCD clock frequency, and m is a positive integer.

The filter structure is based on a device described previously [23,24] and is shown schematically in Fig. IV-7. Each reference bit-word is serially loaded into a shift register and stored in the latch circuits. The output of each triangular section represents the correlation of an analog input signal with a specific bit of the reference words. As can be seen in Fig. IV-7, the

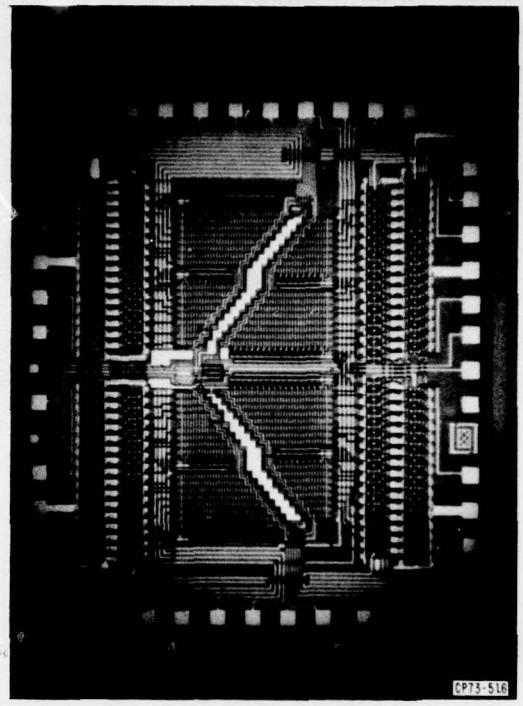


Fig. IV-6. Photograph of 4-bit, 16-tap CCD programmable transversal filter. Each triangular section is one bit.

correct filter output is achieved by binary weighted summation of signals from three sections. This summation can be performed in off-chip analog circuitry, but at the expense of additional components and power dissipation. A novel technique for performing on-chip weighted signal summation in the charge domain at the output of each section has been developed and is described here.

The operation of the weighted charge summation circuit is illustrated in Figs. IV-8 and -9. Each triangular section has a long charge collection node along the outputs of the delay lines. This collection node consists of two diode diffusions (D_1 and D_2 in Fig. IV-8) separated by a gate, called a partition gate, forming transistor Q_p. The operation of this circuit is shown in three stages beginning [Fig. IV-9(a)] at a time when charge packets in the last φ_2 storage wells are ready to be transferred to the collection diodes and the partition gate is off. When the φ_2 clock and transfer gate go low, the charge from the 16 delay lines is transferred to the two collection diodes. Since each collection diode services a different set of delay lines, the partition gate must go on to allow charge exchange and to equalize the potential on the two diodes [Fig. IV-9(b)]. The partition gate then turns off, the transfer gates (Q_{t1} and Q_{t2} in Fig. IV-8) go on, and the separated quantities of charge are transferred, one to the charge "dump" and the other to an output diode. The portion Q_s [Fig. IV-9(c)] transferred to the output diode is the desired signal, and is related to the total charge Q_T from the triangle section by

$$Q_s = \left(\frac{C_2}{C_1 + C_2}\right) Q_T$$

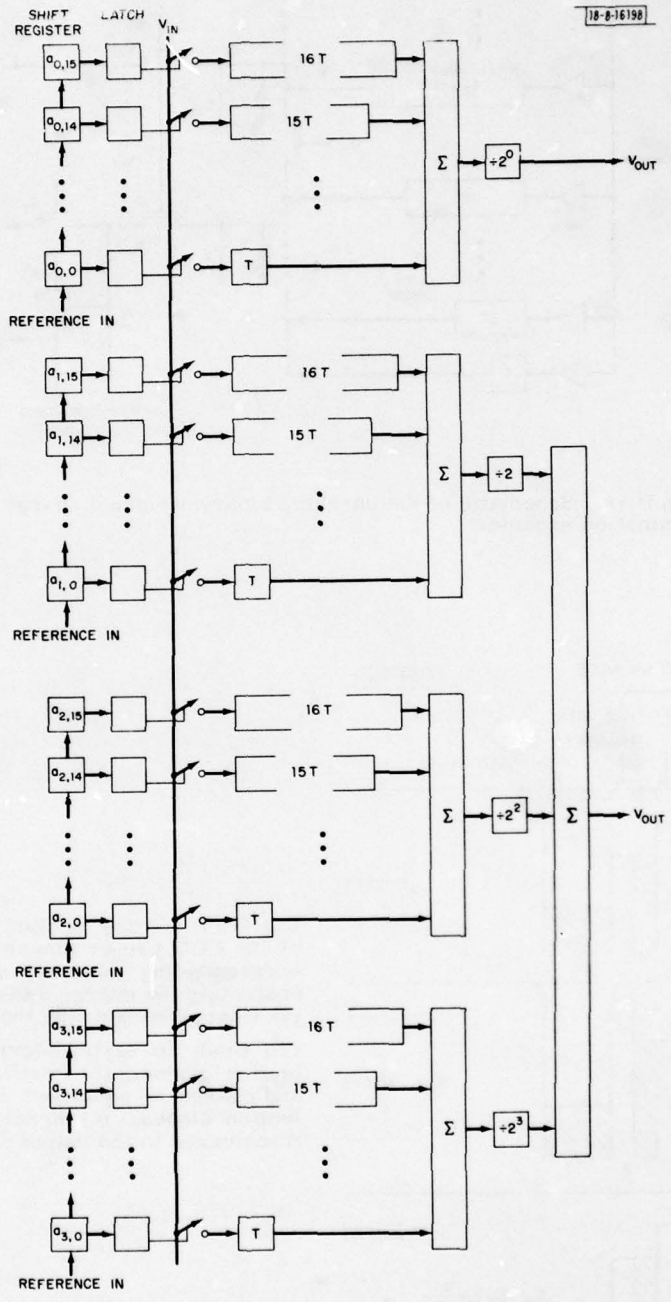


Fig. IV-7. Schematic describing operation of the programmable transversal filter shown in Fig. IV-6.

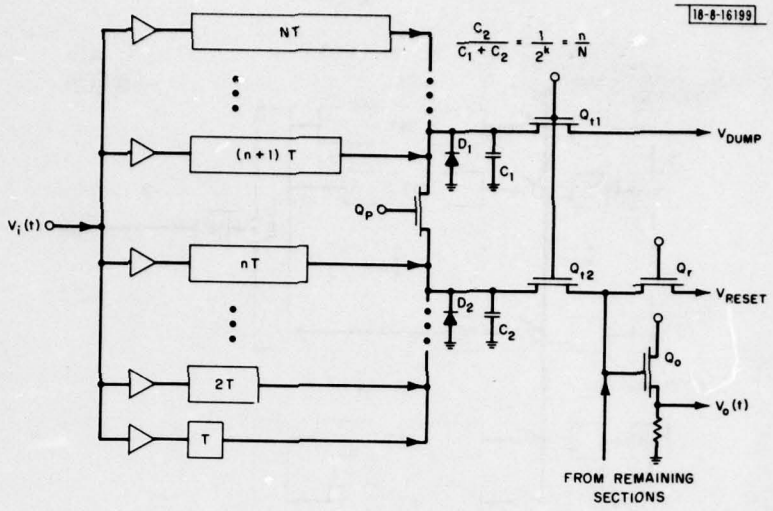


Fig. IV-8. Schematic of the on-chip, binary-weighted charge summation scheme.

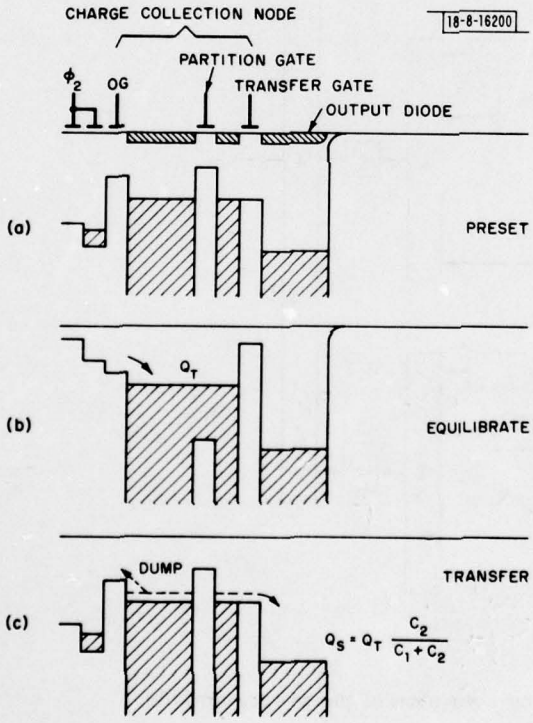


Fig. IV-9. Cross section of a section of the CCD programmable filter with a corresponding potential diagram demonstrating the charge division technique. (a) Charge packets in the last φ_2 wells are ready to be transferred to the collection diodes. (b) Partition gate is on and charge is equalized on the two collection diodes. (c) Signal charge Q_S is transferred to the output diode.

where C_1 and C_2 are the capacitances of each diode segment. The capacitance ratio $C_2/(C_1 + C_2)$ is made equal to 2^{-k} in accordance with Eq. (IV-2). The charge from two of the three remaining sections is similarly weighted and transferred to the same output diode where it is sensed by a conventional floating diffusion output circuit consisting of output and reset transistors, shown as Q_o and Q_r in Fig. IV-8. In the present structure the MSB output is brought out separately to be subtracted in an off-chip differential amplifier from the output of the remaining three sections. An examination of Fig. IV-6 shows the location of the partition along the staircase-shaped collection diodes at the outputs of all but the MSB triangle.

To demonstrate programmable matched filtering for a chirp signal, the tap weights of the device have been programmed as a cosine down-chirp, i.e.,

$$h_n = \cos 8\pi \left(\frac{15 - n}{16}\right)^2 \qquad n = 0, \ldots 15$$

The impulse response of the device is shown in Fig. IV-10(a). When a negative cosine up-chirp

$$V_{in}(m) = -\cos 8\pi \left(\frac{m}{16}\right)^2 \qquad m = 0, \ldots 15$$

is applied to the CCD signal gate, the convolution output of the filter has the correct peak-to-sidelobe ratio for this waveform, as shown in Fig. IV-10(b). Operating in this mode, a dynamic range of 50 dB has been measured.

A. M. Chiang
B. E. Burke

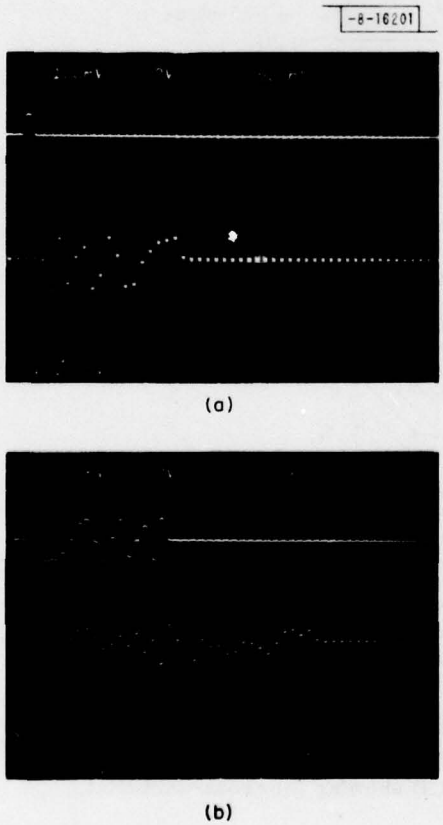


Fig. IV-10. Programmable matched filtering using the 4-bit, 16-tap device. (a) Impulse response of the device with tap weights programmed as a cosine down chirp. (b) Output of the device when a cosine up-chirp is applied to inputs of the CCD and the tap weights are programmed as in (a). Output is the convolution of the two signals and gives the correct peak-to-sidelobe ratio for this waveform.

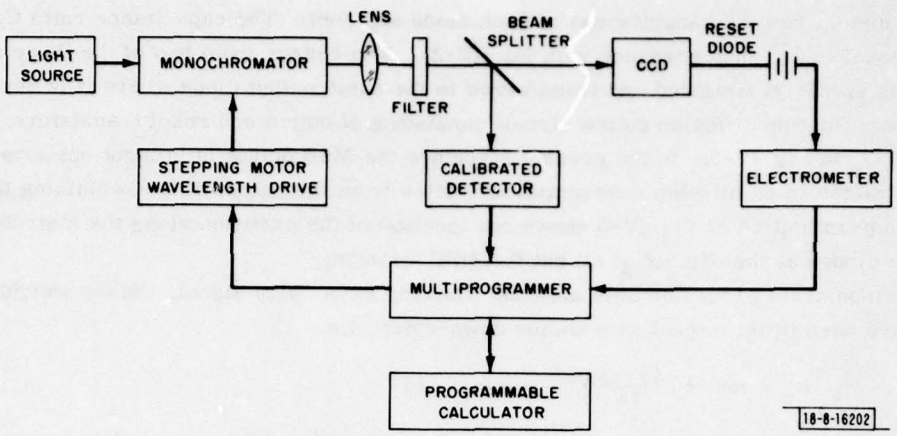


Fig. IV-11. Diagram of system for measurement of CCD quantum efficiency.

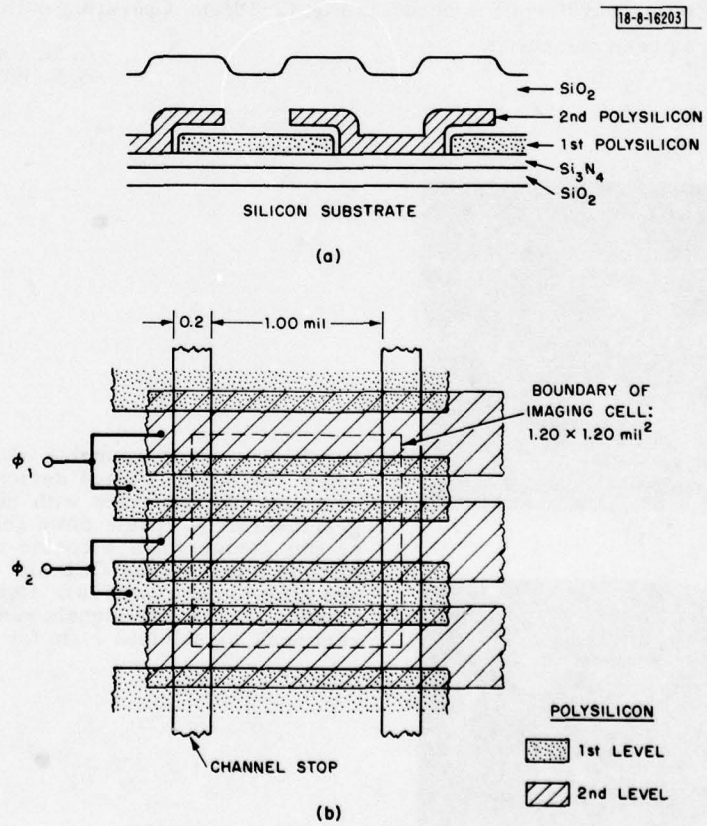


Fig. IV-12. Details of gate structure of the CCD showing (a) cross-sectional view and (b) top view of a unit imaging cell.

D. CHARGE-COUPLED DEVICES: IMAGERS

Measurements of the spectral quantum efficiency of the 100- × 400-element CCD imager have been made. The device is a polysilicon gate front illuminated silicon CCD made for the GEODSS (Ground Electro-Optical Deep Space Surveillance) program for use as a ground-based sensor for satellite surveillance. For this application the sensor is to have maximum responsivity to an air mass 2 (AM2) solar spectrum which has a maximum photon flux at about 700 nm. Measured data span the wavelength range from 400 to 1100 nm, and typically average around 50-percent quantum efficiency over a midband range from 600 to 900 nm.

The quantum efficiency was measured by illuminating the device with radiation from a monochromator and measuring the photocurrent collected by the CCD. An automated system controlled by a Hewlett-Packard 9825A calculator was used for the measurements and data reduction, and this system is illustrated by the diagram in Fig. IV-11. The calculator controls the measurements through an I/O instrument (Multiprogrammer) containing circuit cards to provide the interface between the calculator and the measurement instruments. A card provides the timing pulses to control the stepper motor which sets the monochromator wavelength. The monochromator employs a holographic grating which is usable from 300 to 1100 nm. The slits used in these measurements produce a 3-nm optical bandwidth. A portion of the optical beam is reflected by the beam splitter to a silicon photovoltaic detector. The detector is packaged with an op-amp which provides a voltage output proportional to the optical power and is calibrated by the manufacturer. The photoelectrons collected by the CCD are transported to an output sense circuit and come off the chip at a diode called the reset diode. The photocurrent flowing into this diode is measured by an electrometer from which a voltage proportional to this current is available. The detector and electrometer voltages are multiplexed through relays to a 12-bit A/D converter contained in the Multiprogrammer. The optical beam image is contained entirely within the active areas of both detector and CCD, and therefore no area corrections are needed in the data. The CCD responsivity is thus the photocurrent divided by the incident optical power. The CCDs used in these measurements generally had room temperature dark currents of less than 2 nA (corresponding to 6 nA/cm^2), while saturation level photocurrents were 80 nA or more at the clock rates used. Because of this high signal-to-background ratio, synchronous detection methods were not required.

The CCD structure in cross section is shown in Fig. IV-12(a), and a top view of a unit pixel in Fig. IV-12(b). The channel stops are a relatively inactive region optically but account for only 16 percent of the area. Thus the structure has a high percentage of active area. For the device discussed below, the first- and second-level polysilicon thicknesses were 3500 and 2600 Å, respectively, the gate SiO_2 and Si_3N_4 thicknesses were both 800 Å, and the top protective oxide was 1.5 μm thick. The first polysilicon was deposited in an RF-heated reactor, and its thickness is somewhat greater than desired due to problems of uniformity control in that system. A low-pressure hot-wall CVD (LPCVD) deposition system became available for the second-level polysilicon. This system has superior uniformity and thickness control, and permitted a much thinner second polysilicon layer to be used. This is an important consideration for the CCD imager because the polysilicon thickness has a major influence on the quantum efficiency, not only in the blue portion of the spectrum where the optical attenuation in silicon is high, but also at longer wavelengths where optical tailoring techniques can be used to minimize reflection losses.[25]

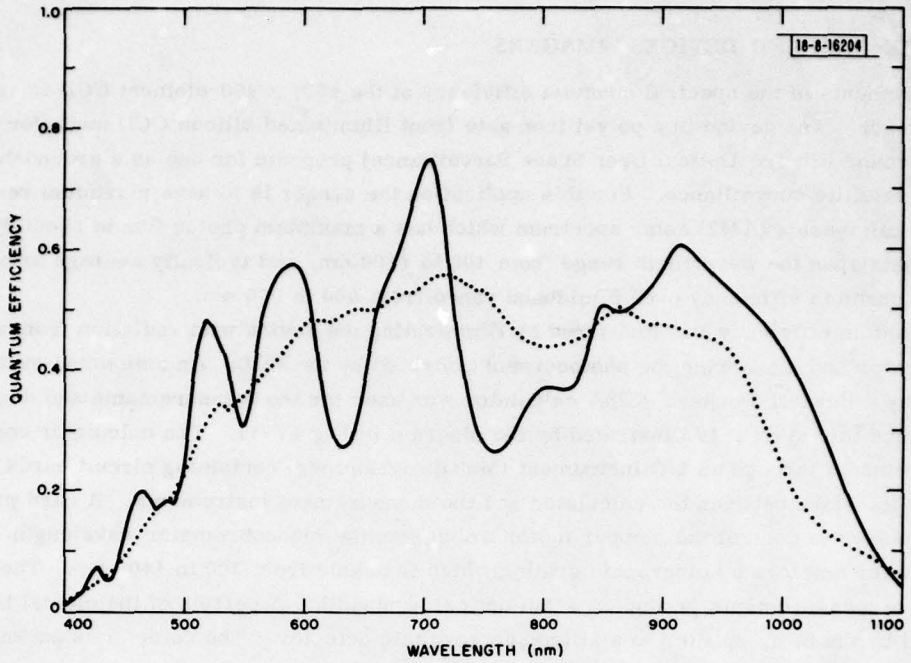


Fig. IV-13. Experimental (data) and theoretical (smooth curve) quantum efficiency for a CCD imager.

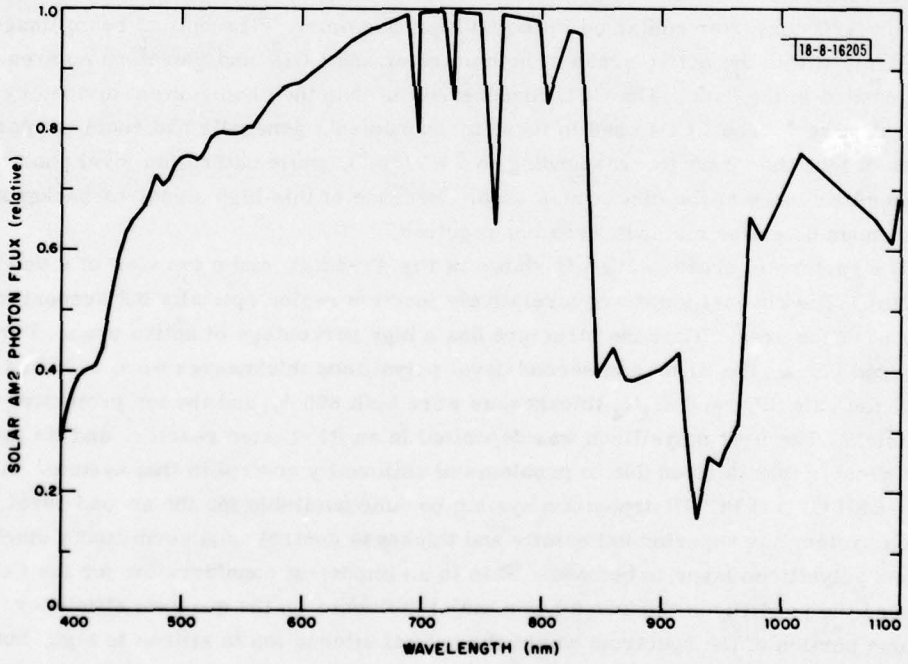


Fig. IV-14. Relative photon flux for the solar AM2 spectrum.

A representative set of data is shown in Fig. IV-13. The quantum efficiency averages approximately 50 percent in the range from 600 to 900 nm for this device. The monochromator radiation is nearly collimated and normal to CCD surface. In an optical system the radiation will be incident on the sensor over a range of angles, the maximum angle from normal being arctan [(1 + d/D)/2f]. where d is the longest dimension of the sensor, D is the diameter, and f the focal length of the optics. In the GEODSS systems with approximately F/3 optics this angle will be about 10°. Measured data show very little variation of quantum efficiency up to angles of 15°. The variation in total responsivity and average quantum efficiency as defined below is less than 3 percent over this range of angles.

A theoretical calculation of the quantum efficiency is also shown in Fig. IV-13 based on the parameters of the device. The calculation uses standard methods of calculating transmission through multiple films,[26] and the optical constants of single crystal silicon[27,28] are used for the polysilicon. The formulation of the carrier generation and collection is based on the work of Brown and Chamberlain.[29] The most striking feature in the comparison of experiment and theory is the relative smoothness of the data compared to the large amplitude peaks and valleys of the theory. Similar results have been noted elsewhere for polysilicon gate imagers.[25] The discrepancy has been attributed to the effects of optical scattering at the polysilicon grain boundaries.

For any imaging sensor it is necessary to know how the responsivity of the sensor matches the radiation output of the target or image being viewed. In the GEODSS system the targets of interest are satellites which are viewed in reflected sunlight. Satellites of particular interest are those in geosynchronous orbits, and it is assumed that the spectral irradiance of such targets at future GEODSS sites will be approximately that of an AM2 solar spectrum. Efforts to improve the CCD quantum efficiency will therefore be directed toward maximizing the responsivity to this irradiance distribution.

A plot of the relative AM2 solar photon flux for wavelengths from 400 to 1100 nm is shown in Fig. IV-14. The peak photon flux occurs at about 700 nm and has an overall shape similar to the CCD quantum efficiency. Two parameters we use to characterize the CCD response to a particular source are the total responsivity R_T and a weighted average quantum efficiency $\overline{\eta}$ They are defined by the following expressions:

$$R_T = \frac{\int_0^\infty R(\lambda)\, W(\lambda)\, d\lambda}{\int_0^\infty W(\lambda)\, d\lambda} = \frac{q}{hc} \frac{\int_0^\infty \lambda\, \eta(\lambda)\, W(\lambda)\, d\lambda}{\int_0^\infty W(\lambda)\, d\lambda}$$

and

$$\overline{\eta} = \frac{\int_{400}^{1000} \eta(\lambda)\, \varphi(\lambda)\, d\lambda}{\int_{400}^{1000} \varphi(\lambda)\, d\lambda}$$

where $R(\lambda) = (q\lambda/hc)\, \eta(\lambda)$ is the sensor spectral responsivity in A/W, $\eta(\lambda)$ is the spectral quantum efficiency, and h = Planck's constant. The spectral power flux $W(\lambda)$ and photon flux $\varphi(\lambda)$ of the source are related by $\varphi(\lambda) = (\lambda/hc)\, W(\lambda)$. The average quantum efficiency $\overline{\eta}$ is defined for the wavelength range of 400 to 1000 nm, which represents the useful limits of the CCD sensitivity. Of the total solar AM2 energy, approximately 70 percent is contained within this band. The CCD response beyond 1000 nm is not considered useful due to radiation from night sky background.

For the data of Fig. IV-13, the solar AM2 responsivity R_T is 153 mA/W and the average quantum efficiency $\bar{\eta}$ is 41 percent, while the theoretical values are 161 mA/W and 41 percent, respectively. This close agreement is somewhat surprising in view of the dissimilarities of the two curves.

Improvements in the quantum efficiency can be expected in future devices due to the improved control over polysilicon thickness in the LPCVD system. Experiments are under way to make devices having the gate structure in which an additional silicon nitride layer is placed on top of the polysilicon[25] and all layer thicknesses adjusted to maximize the solar AM2 responsivity.

B. E. Burke

REFERENCES

1. H. I. Smith and D. C. Flanders, Appl. Phys. Lett. 32, 349 (1978).
2. D. C. Flanders, D. C. Shaver, and H. I. Smith, Appl. Phys. Lett. 32, 597 (1978).
3. D. C. Flanders, "Orientation of Crystalline Overlayers on Amorphous Substrates by Artificially Produced Surface Relief Structures," Ph. D. Thesis, Department of Electrical Engineering and Computer Sciences, Massachusetts Institute of Technology, 1978; reprinted as Technical Report 533, Lincoln Laboratory, M.I.T. (5 December 1978), DDC AD-A071168.
4. D. C. Shaver, M. S. Thesis, Department of Electrical Engineering and Computer Sciences, Massachusetts Institute of Technology, September 1978.
5. H. I. Smith, D. C. Flanders, and D. C. Shaver, "New Applications of Submicrometer Structures in Materials Science and Biology," in Scanning Electron Microscopy (1978), Vol. 1, pp. 33-40, O. Johari, Ed. (Scanning Electron Microscopy, Inc., 1978).
6. D. C. Flanders and H. I. Smith, J. Vac. Sci. Technol. 15, 1001 (1978).
7. D. C. Flanders, H. I. Smith, H. W. Lehmann, R. Widmer, and D. C. Shaver, Appl. Phys. Lett. 32, 112 (1978).
8. H. W. Lehmann and R. Widmer, Appl. Phys. Lett. 32, 163 (1978); and erratum Appl. Phys. Lett. 33, 367 (1978).
9. A. Gat, L. Gerzberg, J. F. Gibbons, T. J. Magee, J. Peng, and I. D. Hong, Appl. Phys. Lett. 33, 775 (1978).
10. J. C. C. Fan and H. J. Zeiger, Appl. Phys. Lett. 27, 224 (1975).
11. J. Melngailis, H. I. Smith, and N. Efremow, IEEE Trans. Electron Devices ED-22, 496 (1975).
12. J. R. Vig, IEEE Trans. Parts, Hybrids and Packaging PHP-12, 365 (1976).
13. R. P. Heidenreich, Fundamentals of Transmission Electron Microscopy (Interscience Publishers, New York, 1964), Chap. 3.
14. Solid State Research Report, Lincoln Laboratory, M.I.T. (1978:3), pp. 31-32, DDC AD-A065116.
15. Ibid. (1979:1), pp. 51-53.
16. Ibid. (1978:2), pp. 34-36, DDC AD-A061241.

17. C. H. Sequin and M. F. Tompsett, Charge Transfer Devices (Academic Press, New York, 1975), pp. 48-52.

18. Solid State Research Report, Lincoln Laboratory, M.I.T. (1978:4), pp. 47-52, DDC AD-A068563.

19. E. C. Farnett, T. B. Howard, and G. H. Stevens, Radar Handbook, M. Skolnik, Ed. (McGraw-Hill, New York, 1970), p. 20-19.

20. R. F. Milsom, N. H. C. Reilly, and M. Redwood, IEEE Trans. Sonics Ultrason. SU-24, 147 (1977).

21. D. H. Hurlburt, R. W. Ralston, R. P. Baker, and E. Stern, 1978 Ultrasonics Symposium Proceedings (IEEE, New York, 1978), p. 33.

22. D. L. Smythe, R. W. Ralston, B. E. Burke, and E. Stern, Appl. Phys. Lett. 33, 1025 (1978).

23. B. E. Burke and W. T. Lindley, Electron. Lett. 13, 521 (1977).

24. Solid State Research Report, Lincoln Laboratory, M.I.T. (1978:2) pp. 37-39, DDC AD-A061241.

25. R. H. Dyck and R. Wight, Proceedings of SPIE (Solid-State Imaging Devices), Vol. 116 (1977), p. 19.

26. H. A. Macleod, Thin Film Optical Filters (American Elsevier, New York, 1969).

27. W. C. Dash and R. Newman, Phys. Rev. 99, 1151 (1955).

28. H. R. Phillip and E. A. Taft, Phys. Rev. 120, 37 (1960).

29. R. W. Brown and S. G. Chamberlain, Phys. Status Solidi 20, 675 (1973).

V. ANALOG DEVICE TECHNOLOGY

A. SUPPRESSION OF SPURIOUS SIGNALS IN MEMORY CORRELATORS

The development of an acoustoelectric memory-correlator subsystem has been reported.[1,2] The heart of this subsystem is a memory correlator which was described in some detail in an earlier report.[1] To achieve optimum performance of the subsystem, and any system of which the memory correlator is a part, the memory correlator must be as free of spurious signals as possible. Considerable improvement has been made in the suppression of the unwanted spurious signals, and techniques have been developed which promise still further suppression.

The first step in eliminating spurious signals within memory correlators was to identify the source of these signals and then to develop suppression techniques. Four separate sources have been identified. They are: electromagnetic feedthrough from the input transducer, bulk-wave generation by the input transducer, bulk-wave scattering occurring when the surface wave impinges on the support structure for the silicon strip, and edge detection by the edges of the silicon strip. The problems of electromagnetic feedthrough and bulk-wave generation by the transducer were discussed in a previous report.[1] New approaches have been taken to achieve suppression of the other spurious signals.

The most troublesome of the spurious signals has been edge detection caused by the stray capacitance at the edges of the silicon strip. The result is an output signal at the same frequency as the surface wave occurring when the wave first passes under the silicon and again when it leaves. A variety of methods, including slanting the ends of the silicon strip and using metal shields on the crystal surface under the ends of the silicon strip, have been tried with limited success. The method which has proven successful has been the use of a double-transducer structure in conjunction with metal shields, as shown schematically in Fig. V-1. The double transducer launches two parallel acoustic beams which, because of the 180° hybrid at the input, are out of phase by 180°. Identical matching networks are required on each section of the double transducer. Ideally, the signals detected by the ends of the silicon would be out of phase and cancel completely. In practice cancellation is incomplete, but the use of metal shields is sufficient to suppress any residual pickup. The use of the double-transducer configuration and the out-of-phase drive is as effective in suppressing electromagnetic feedthrough as the balanced device which was described earlier.[1]

With the double transducer it is unwieldy to use a multistrip coupler to eliminate bulk waves generated by the transducers. In practice it has been observed that the level of spurious bulk-wave signals generated by the double-transducer configuration is low, perhaps because any bulk waves generated by the antiphase drive in the two transducers tend to cancel. The addition of a transparent urethane absorber on the back of the surface-wave substrate has proven capable of eliminating most of the remaining spurious bulk waves generated by the transducers. Experiments are currently in progress to determine if the 127.86° rotated Y-cut of $LiNbO_3$ will improve this situation. This cut is known to have very low coupling to bulk waves.

The last remaining source of spurious signals is the scattering into bulk waves which occurs when the surface waves are incident on the rails that support the silicon strip; however, this spurious signal has been greatly reduced by the use of the double-transducer configuration. The surface wave launched by this configuration has a null at the center of the beam; thus scattering

PRECEDING PAGE BLANK-NOT FILMED

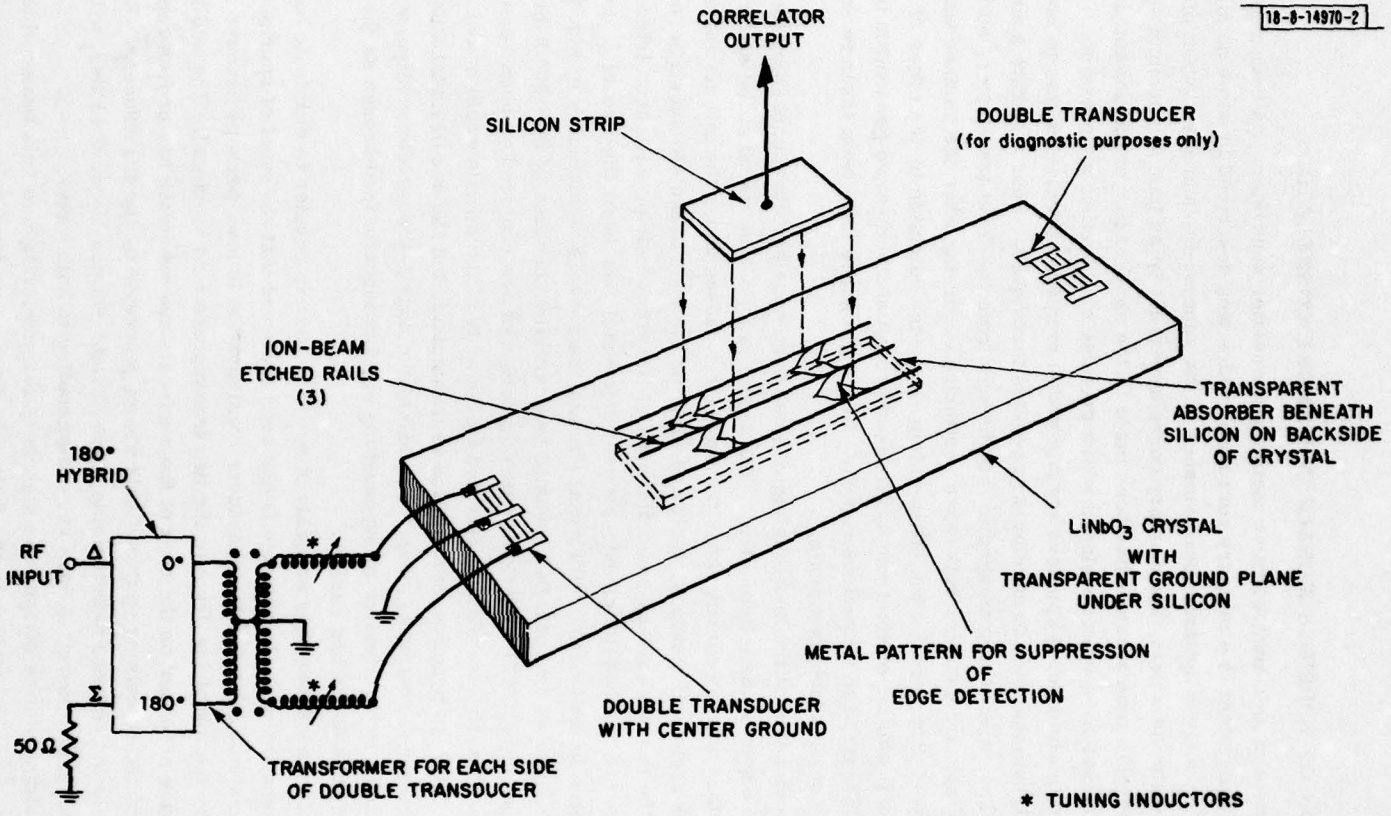


Fig. V-1. Schematic diagram of a memory correlator containing a double input transducer and metal patterns for suppression of edge detection.



Fig. V-2. Major parts of a memory correlator containing double input transducers. Top: Silicon strip mounted on Kapton. Middle: $LiNbO_3$ substrates and matching circuits mounted in package base. Bottom: LED array for erasure.

off the central supporting rail is eliminated. However, some surface-wave energy is incident on the outer rails, most likely as the result of diffraction from the transducers, and hence some small amount of energy is still converted to bulk waves.

A preassembly view of a memory correlator with the double-transducer configuration is shown in Fig. V-2. The $LiNbO_3$ crystal is mounted in the package with matching network at either end. The double transducer is visible at the left-hand end of the crystal, while the metal shields that are located under the ends of the silicon are the very small patterns in the central region of the crystal. The dark band that covers the central section of the crystal is the transparent ground plane which is on the backside of the $LiNbO_3$. Above the crystal is located the silicon strip containing the Schottky diode array. The object located below the crystal in Fig. V-2 is the bottom cover plate, which contains the LED array that is used for erasure of the stored pattern in the diode array.

Figure V-3(a) shows the response of the memory correlator when used to process a 5-μsec-long 50-MHz-bandwidth linear-FM waveform. The approximately $(\sin x)/x$ sidelobes due to the compression of an unweighted chirp are readily apparent. In Fig. V-3(b) the remaining residual spurious signals, virtually all caused by bulk-wave scattering, can be observed. (Note the increased gain of 20 dB.) At the present time the spurious signals introduce sidelobes which are

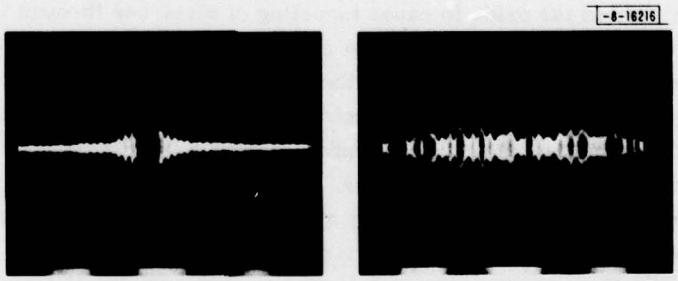


Fig. V-3. Response of memory correlator. (a) Compressed pulse obtained during matched filtering of a 5-μsec 50-MHz linear-FM waveform. (b) Gain increased by 20-dB to show residual spurious signals which occur at the output even when no reference is stored.

on the order of 35-dB below the peak memory correlator output. Experiments are currently under way in an attempt to eliminate the remnants of this spurious signal by using a low-bulk-wave cut of $LiNbO_3$ and by forming a guiding structure on the surface of the $LiNbO_3$ so that the surface-wave energy will not be incident on the supporting rails.

D. H. Hurlburt

B. MNOS NONVOLATILE ANALOG MEMORY

MNOS capacitor structures are being investigated for use as nonvolatile analog memories. Such a memory is compatible with present CCD and SAW/CCD technology and would greatly extend the signal storage time of these devices.

In the past few years a widespread technological effort has been directed at the development of MNOS structures for the storage of digital data. The device is, in its simplest form, a dual-dielectric capacitor cell as shown in Fig. V-4. It consists of a metal gate electrode (Cr in our

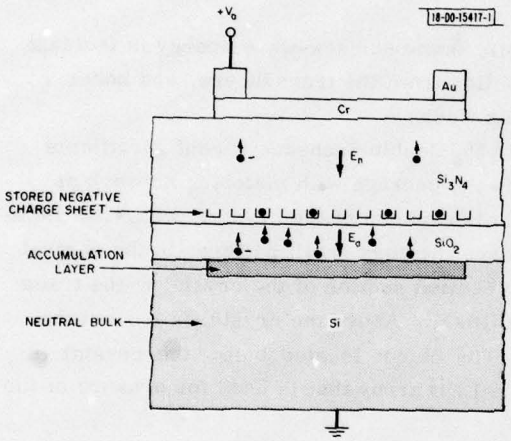


Fig. V-4. MNOS charging with majority carriers. Oxide field E_o is linearly dependent on the applied voltage and the quantity of stored charge.

case, but more commonly, Al), a chemically-vapor-deposited silicon-nitride layer about 500 Å thick, a thermally grown silicon-dioxide layer only 25 to 40 Å thick, and a silicon substrate (shown as n-type). Consider a positive voltage applied to the gate. The positive bias serves to accumulate majority carriers (electrons) at the $Si-SiO_2$ interface, and thus there is little potential drop across the silicon. For moderate gate voltages of the order of 30 V, there exists a sufficiently intense field in the oxide to cause tunneling of electrons through the oxide. The amorphous nitride layer is grown with very low conductivity, and hence this layer serves to block most of the electron flow. As a result, the electrons are captured at or near the oxide-nitride interface by a high density of traps which exist at the interface or in the nitride. The precise nature of the tunneling current and trapped charge is determined by the spatial and energy distribution of empty and occupied traps.

Several charge transport mechanisms play a role in the charging and discharging of these devices. A brief examination of these mechanisms is fruitful.

The band diagram for majority carrier injection is shown in Fig. V-5. Two tunneling mechanisms are most plausible: direct tunneling of valence-band electrons to traps [Fig. V-5(a)] and band-to-band (modified Fowler-Nordheim) tunneling from the silicon conduction band to the

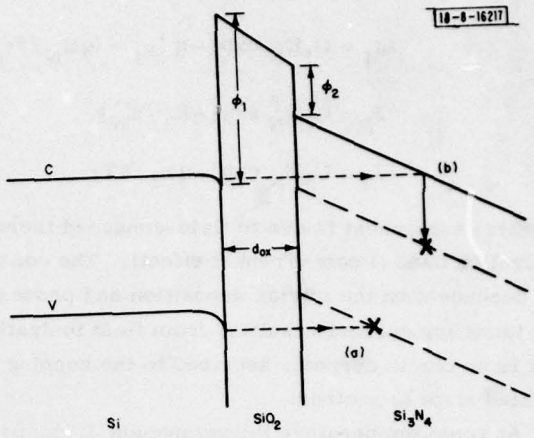


Fig. V-5. Band diagram of MNOS interfacial region during majority charging.

nitride conduction band followed by trapping [Fig. V-5(b)]. In both cases, the tunneling current is exponentially dependent on the field strength and oxide thickness. For instance, the band-to-band tunneling current may be written[3]

$$J_{BB} = C_{FN} E_{ox}^2 P_{ox} P_N \tag{V-1}$$

where C_{FN} is a constant, characteristic of Fowler-Nordheim tunneling from silicon into SiO_2, and E_{ox} is the oxide field strength. P_{ox} and P_N are the tunneling probabilities through the oxide and nitride, respectively, given by

$$P_{ox} = \exp\left\{-\frac{4}{3h}\sqrt{2qm_{ox}^*}\left[\varphi_1^{3/2} - (\varphi_1 - d_{ox}E_{ox})^{3/2}\right]/E_{ox}\right\} \tag{V-2}$$

and

$$P_N = \exp\left\{-\frac{4}{3h}\sqrt{2qm_N^*}\,(\varphi_1 - \varphi_2 - d_{ox}E_{ox})^{3/2}/E_N\right\} \tag{V-3}$$

where $\varphi_1 = 3.1$ eV and $\varphi_2 = 1.05$ eV are the barrier heights (defined in Fig. V-5), d_{ox} is the oxide thickness, and m_{ox}^* and m_N^* are the electron effective masses in the oxide and nitride. The nitride field E_N is, in this approximation, assumed to be related to the oxide field by $E_N = (\epsilon_{ox}/\epsilon_N)\,E_{ox}$; i.e., the space charge of the trapped carriers is ignored.

Direct tunneling occurs to nitride and/or interfacial traps which, in the absence of an applied voltage, are located energetically in the nitride bandgap directly opposite the silicon gap; otherwise the trapped charges would quickly back-tunnel to the silicon. Direct tunneling is thought to be more important in thin-oxide devices[4] ($\lesssim$25 Å), and less so in the thicker-oxide devices under consideration.

Carriers, once trapped, may escape by two routes: back-tunneling through the oxide to the silicon, or conduction (by several mechanisms) through the nitride to the gate electrode. The back-tunneling current[5] is exponentially dependent on the oxide thickness, trap location in the nitride, trap depth, and quantity of trapped charge (through its space-charge effect).

The nitride conduction current, on the other hand, is critically dependent on the nitride processing and ambient temperature. Three components of the nitride current can be identified:[6]

$$J_1 = C_1 E_N \exp\{-q\,[\varphi_t - (qE_N/\pi\epsilon_d)^{1/2}]/kT\} \quad \text{(V-4)}$$

$$J_2 = C_2 E_N^2 \exp[-E_2/E_N] \quad \text{(V-5)}$$

$$J_3 = C_3 E_N \exp[-q\varphi_3/kT] \quad \text{(V-6)}$$

The first component is due to field-enhanced thermal excitation of trapped electrons into the conduction band (Poole-Frenkel effect). The constant C_i and dynamic dielectric constant ϵ_d are dependent on the nitride deposition and processing parameters.[7,8] The second component is a tunneling current resulting from field ionization of trapped electrons. The third component is an ohmic current, ascribed to the hopping of thermally excited carriers from one isolated state to another.

At room temperature the component J_1 dominates for electric field strengths $E_N \gtrsim 3 \times 10^8$ V/m, and the ohmic component dominates for weaker fields,[6] although recent experimental evidence indicates that J_1 dominates even for $E_N \gtrsim 10^8$ V/m (Ref. 9). The component J_2 is important only at low temperatures. Thus, for devices operating at room temperature, the Poole-Frenkel component may be expected to limit the value of the charge stored during a majority-carrier writing period (when nitride fields are typically 6×10^8 V/m), a steady-state value of stored charge being reached when the nitride current equals the oxide current. This component may also contribute to the initial loss of stored charge; however, nitride fields in this case are due to the stored charge alone and are typically 3×10^8 V/m or less. The ohmic current may be expected to play a role in this discharge.

The key to an analog memory is to transfer a packet of minority carriers from the silicon to the nitride. In digital devices, minority carrier injection is achieved by providing an essentially unlimited supply of minority carriers to an inversion layer, by means of a field-effect-transistor structure or avalanche breakdown in the depletion layer. Tunneling through the oxide to the nitride traps then proceeds in much the same manner as for majority-carrier injection, although the barrier heights and trap levels (and thus time constants) may be different. For analog memory, a measured amount of minority carriers forms the inversion layer. Ultimately, these packets of carriers will be clocked under the memory gate in CCD fashion; in our experimental devices, the carriers are provided by injecting photons into the depletion layer.

Minority-carrier injection is illustrated in Fig. V-6. A negative gate voltage forms a depletion layer in the n-type silicon. In the absence of an inversion layer, almost all the applied

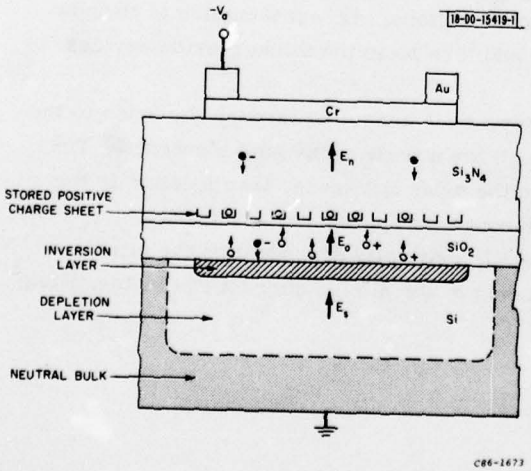


Fig. V-6. MNOS charging with minority carriers. Oxide field E_O is linearly dependent on inversion layer charge and only weakly dependent on applied voltage and stored charge.

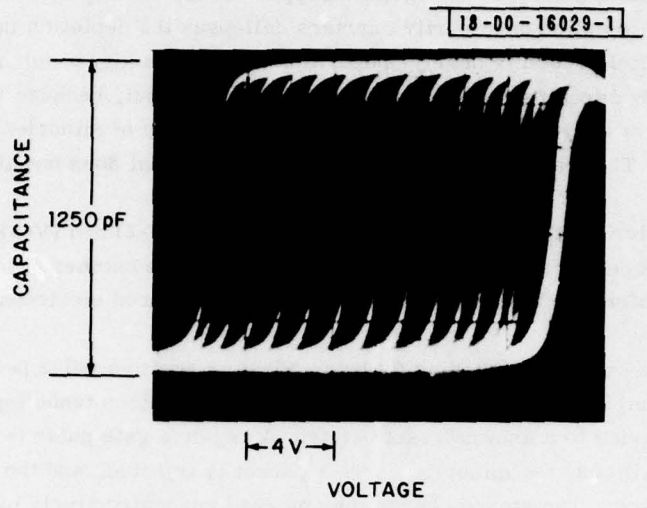
potential (and potential of any trapped charge) is dropped across the depletion layer; the oxide field is very low. The injection of minority carriers collapses the depletion layer somewhat and produces an oxide field which is nearly proportional to the quantity of minority carriers. Ideally, all the minority carriers would tunnel through the oxide but, because the tunneling depends on the self-field of the minority carriers, a certain quantity of minority charge must remain in the silicon. This necessitates the use of a "fat zero" but does not affect the linearity of the analog memory.

The potential barrier is of the same form as given by Eqs. (V-2) and (V-3), but the pre-exponential factor in Eq. (V-1) is modified to account for the finite number of available carriers. Additional charge transfer is effected by the back-tunneling of stored electrons, induced by the increased oxide field.

The analog storage cell is operated as follows: First, a positive pulse ($\simeq 30$ V and some milliseconds in duration) is applied to the gate. This causes electron tunneling to the nitride traps and brings the device to a known "reset" state. A negative gate pulse ($\simeq -20$ V) is then applied to deplete the silicon, the minority-carrier packet is injected, and the tunneling of minority charge takes place. The stored charge may be read nondestructively by a simple C-V measurement; the flat-band voltage shift is proportional to the stored charge. Ultimately, in an integrated CCD-MNOS device, the stored signal charge would be read nondestructively by filling the depleted potential well in the silicon below the MNOS gate.

Here we wish to describe the encouraging results obtained on isolated MNOS memory cells which were fabricated on 10-Ω-cm n-type Si without peripheral input/output circuitry. The geometry of these stand-alone capacitors is depicted in Figs. V-4 and -6. As was previously described, a positive gate voltage is first applied to reset the memory traps to a large electron occupation. Then a comparable negative gate voltage is applied which deep depletes the silicon. Held in the dark, the thermal generation of minority carriers occurs very slowly (full inversion takes 2 min.), and thus for short times, insufficient holes and insufficient oxide field are present for appreciable tunneling to occur. Into this empty deep-depleted well we are able to inject a controlled light flux by illuminating the semi-transparent Cr gate with an array of LEDs. The photon flux absorbed in the depletion layer generates electron-hole pairs; the depletion field sweeps the electrons into the neutral bulk, while the holes are swept to the Si-SiO_2 interface and there form an inversion layer. The formation of the inversion layer causes a collapse in the depletion field, hence a redistribution of the applied voltage occurs, and a significant tunneling field is obtained in the oxide. Holes from the controlled inversion layer are able to occupy the nitride traps. The results below show that the trapped charge is linearly proportional to the injected inversion charge over a wide range. This provides a suitable analog store mechanism.

The results of our experiment are shown in Fig. V-7(a), which is a family of capacitance-voltage characteristics for a typical MNOS cell. For each curve, the read waveform is ramped from +15 to −15 V in 100 μsec [right-to-left in Fig. V-7(a)], which sweeps the silicon surface from accumulation through flat-band and into deep depletion with a corresponding swing in capacitance from about 1250 pF to nearly zero. The read waveform, of course, is not sufficient to produce tunneling, hence it does not perturb the trapped memory charge. The right-most curve is the result of a reset operation at +32 V. All other curves are for successively increasing amounts of signal (inversion) charge, each injected optically within 500 msec at −27 V with intervening resets.



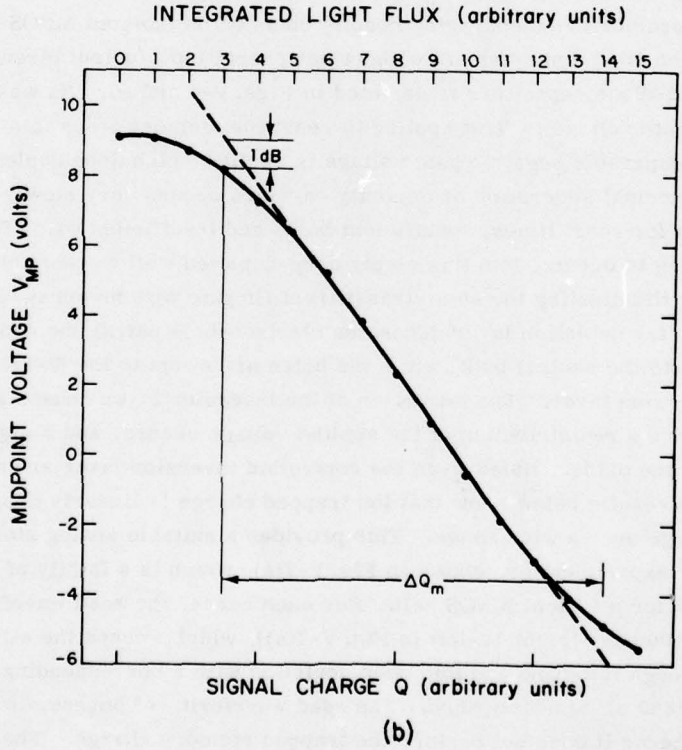
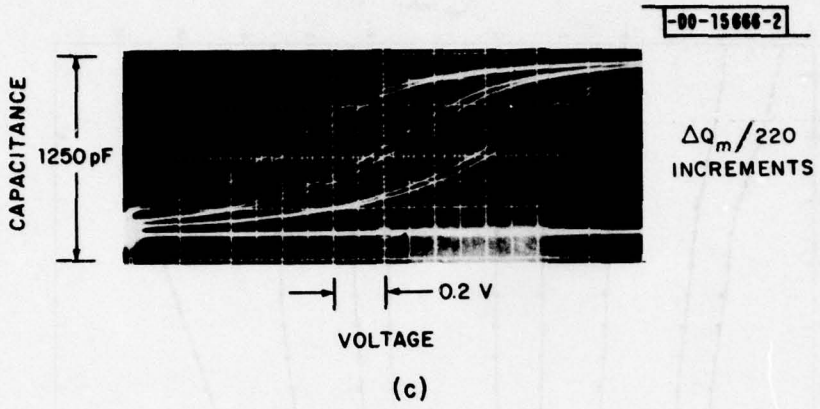


Fig. V-7. (a) Capacitance-voltage characteristic of typical MNOS cell indicating nondestructive readout of different analog signal charges. (b) Reduced data obtained from (a) indicating a large linear range.

Figure V-7(b) is a plot in which we indicate the midpoint voltage for each of the above C(V) curves as a function of integrated light flux or, equivalently, the analog signal charge. Note that over a voltage swing of nearly 13 V the stored charge is essentially a linear (to within 1 dB) replica of the input signal. Certainly, then, large quantities of charge can be stored in a linear analog fashion. This maximum linear analog charge-handling capacity we label as ΔQ_m.



(c)

Fig. V-7. (c) Capacitance-voltage characteristic around the central point in (b) indicating the sensitivity of readout to small increments in stored charge.

Figure V-7(c) is the expanded region about the central point. Here the smallest voltage shifts (~80 mV) result from increments in signal charge equal to $\Delta Q_m/220$. These shifts are clearly discernible, are well above the noise level in this read-out scheme, and indicate an analog dynamic range for this single MNOS cell in excess of 47 dB. The results confirmed our expectation that it should be possible to enter analog signals in the form of minority carriers into MNOS storage.

Of major concern is the loss of signal charge with time, a process which limits the useful storage time of these devices. Figure V-8 is a plot of experimental measurements of this decay in our devices. The decay of stored charge is clearly logarithmic in time, although for positive flat-band voltages (negative charge), the onset of this decay is somewhat delayed. (This is believed to be due to the low oxide field existing before the buildup of a thermally generated inversion layer.) The rate of decay (volts per decade) is evidently dependent on the initial flat-band voltage. A plot of the rate of decay vs initial flat-band voltage (Fig. V-9), in fact, reveals a linear dependence, as has been predicted theoretically.[5] Thus, although the decay is logarithmic in time, at any one moment a linear relation holds between the initial analog signal and the remaining stored charge. The magnitude of the decay rate is not as critical as its linear dependence on initial charge.

Numerical models of these MNOS capacitors are being made with the intention of gaining a better understanding of the important mechanisms in the charging and discharging of these devices. Further improvements in the charge retentivity of the memory cells are also dependent on the ability to grow reproducible thin oxides (~30 Å, with an error of 2 Å or less) and to deposit low-conductivity nitrides with reproducible trap levels and densities.

In summary, we have demonstrated nonvolatile storage of analog signal levels in isolated solid state devices with a dynamic range of greater than 40 dB. Initial results indicate that the decay rate (volts per decade of storage time) is linearly dependent on the initial signal level;

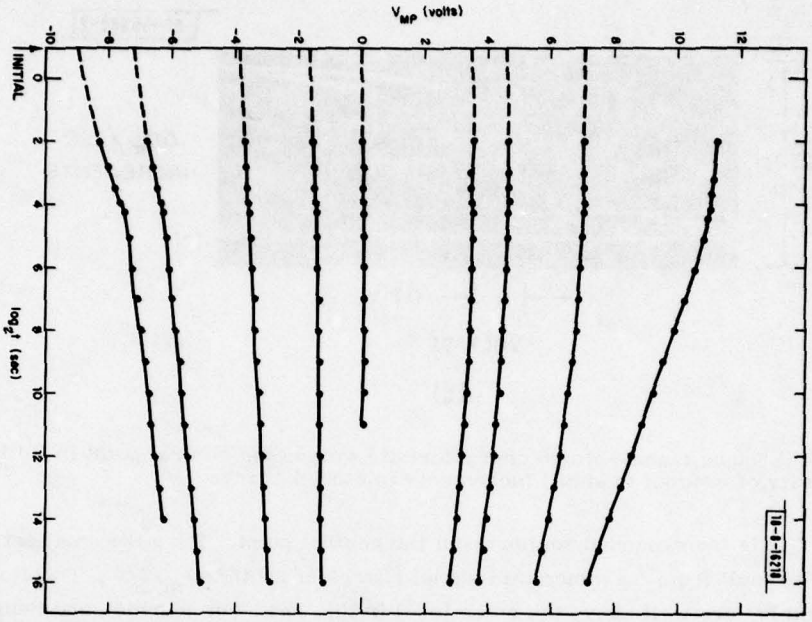


Fig. V-8. Decay of stored charge (as represented by the midpoint voltage V_{MP}) with time after writing.

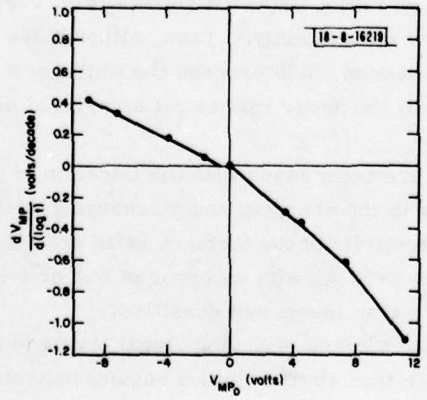


Fig. V-9. Rate of decay of stored charge (midpoint voltage), in units of volts per decade of storage time, as a function of initial midpoint voltage. Data from Fig. V-8.

thus, a waveform sampled at a series of storage sites may be attenuated in time but not distorted. Even so, a lower decay rate would be advantageous. Efforts are under way to obtain a better understanding of storage and conduction mechanisms in the dual dielectric films. Also, better control of the oxide growth and nitride deposition processes is essential to improved charge retention.

R. W. Ralston
R. S. Withers

REFERENCES

1. Solid State Research Report, Lincoln Laboratory, M.I.T. (1978:2), pp. 55-59, DDC AD-A061241.
2. D. H. Hurlburt, R. W. Ralston, R. P. Baker, and E. Stern, "An Acoustoelectric Schottky-Diode Memory Correlator Subsystem," 1978 Ultrasonics Symposium Proceedings (IEEE, New York, 1978), pp. 33-37.
3. K. I. Lundstrom and C. M. Svensson, "Properties of MNOS Structrues," IEEE Trans. Electron Devices ED-19, 826 (1972)
4. A. V. Ferris-Prabhu, "Theory of MNOS Device Behavior," IBM J. Res. Dev. (March 1973), p. 125.
5. L. Lundkvist, I. Lundstrom, and C. M. Svensson, "Discharge of MNOS Structures," Solid-State Electron. 16, 811 (1973).
6. S. M. Sze, "Current Transport and Maximum Dielectric Strength of Silicon Nitride Films," J. Appl. Phys. 38, 2951 (1967).
7. R. Lodi, M. Borovicka, and H. A. R. Wegener, "High Reliability Non-Volatile Integrated Memories," Sperry Research Center, Final Report, TR ECOM-0298-F (May 1973).
8. J. A. Topich and E. T. Yon, "The Effects of High Temperature Annealing on MNOS Devices," J. Electrochem. Soc. 123, 535 (1976).
9. V. M. Efimov, V. A. Kolosanov, and S. P. Sinitsa, "Electron and Hole Conduction in Silicon Nitride at Moderate Electric Fields," Phys. Status Solidi A 49, 217 (1978).

UNCLASSIFIED

SECURITY CLASSIFICATION OF THIS PAGE *(When Data Entered)*

REPORT DOCUMENTATION PAGE		READ INSTRUCTIONS BEFORE COMPLETING FORM
1. REPORT NUMBER ESD-TR-79-150	2. GOVT ACCESSION NO.	3. RECIPIENT'S CATALOG NUMBER
4. TITLE *(and Subtitle)* Solid State Research		5. TYPE OF REPORT & PERIOD COVERED Quarterly Technical Summary 1 February - 30 April 1979
		6. PERFORMING ORG. REPORT NUMBER 1979:2
7. AUTHOR(s) Alan L. McWhorter		8. CONTRACT OR GRANT NUMBER(s) F19628-78-C-0002
9. PERFORMING ORGANIZATION NAME AND ADDRESS Lincoln Laboratory, M.I.T. P.O. Box 73 Lexington, MA 02173		10. PROGRAM ELEMENT, PROJECT, TASK AREA & WORK UNIT NUMBERS Program Element No. 65705F Project No. 649L
11. CONTROLLING OFFICE NAME AND ADDRESS Air Force Systems Command, USAF Andrews AFB Washington, DC 20331		12. REPORT DATE 15 May 1979
		13. NUMBER OF PAGES 92
14. MONITORING AGENCY NAME & ADDRESS *(if different from Controlling Office)* Electronic Systems Division Hanscom AFB Bedford, MA 01731		15. SECURITY CLASS. *(of this report)* Unclassified
		15a. DECLASSIFICATION DOWNGRADING SCHEDULE

16. DISTRIBUTION STATEMENT *(of this Report)*

Approved for public release; distribution unlimited.

17. DISTRIBUTION STATEMENT *(of the abstract entered in Block 20, if different from Report)*

18. SUPPLEMENTARY NOTES

None

19. KEY WORDS *(Continue on reverse side if necessary and identify by block number)*

solid state devices	photodiode devices	infrared imaging
quantum electronics	lasers	surface-wave transducers
materials research	laser spectroscopy	charge-coupled devices
microelectronics	imaging arrays	acoustoelectric devices
analog device technology	signal processing	

20. ABSTRACT *(Continue on reverse side if necessary and identify by block number)*

This report covers in detail the solid state research work of the Solid State Division at Lincoln Laboratory for the period 1 February through 30 April 1979. The topics covered are Solid State Device Research, Quantum Electronics, Materials Research, Microelectronics, and Analog Device Technology. Funding is primarily provided by the Air Force, with additional support provided by the Army, ARPA, NSF, and DOE.

DD FORM 1 JAN 73 1473 EDITION OF 1 NOV 65 IS OBSOLETE

UNCLASSIFIED

SECURITY CLASSIFICATION OF THIS PAGE *(When Data Entered)*


D
FI
5